DEVELOPMENT OF TRANS-RECTAL ULTRASOUND (TRUS) COUPLED DIFFUSE OPTICAL TOMOGRAPHY (DOT) FOR PROSTATE CANCER IMAGING

by

VENKAIAH CHOWDARY KAVURI

Presented to the Faculty of the Graduate School of

The University of Texas at Arlington in Partial Fulfillment

of the Requirements

for the Degree of

DOCTOR OF PHILOSOPHY

THE UNIVERSITY OF TEXAS AT ARLINGTON

August 2014

Acknowledgements

First and foremost I want to thank my advisor Prof. Hanli Liu. I would like to thank her for encouraging my research and for allowing me to grow as a researcher. She has taught me, both consciously and un-consciously, how to be a perfect researcher. I appreciate all her contributions of time, ideas, and funding to make my Ph.D. experience productive and stimulating. I sincerely believe that her belief, advice, guidance and encouragement made my dissertation possible.

Besides my advisor, I would like to thank the rest of my thesis committee: Prof. George Alexandrakis, Dr. Jeffrey Cadeddu, Dr.Payal Kapur, and Prof. Ralph Maspn for their encouragement, insightful comments, and hard questions. My sincere thanks also goes to Prof. Bahong Yuan for teaching me the concepts of Photoacoustics and Prof. Victoria Chen for teaching me the concepts of Statistics leading me gain knowledge on diverse exciting projects.

I should also express my gratitude to Mr. Stephen Savoie for his help to 3d print our probe. I also acknowledge Dr. Monica Morgan for her help in patient selection and identification of tumors during ex-vivo measurements. My sincere thanks also go to Ms. Rebecca Denny for her help during animal handling and preclinical measurements. I should also acknowledge colleagues Mr. Xinlong Wang and Mr. Henry Tran for their help in ex-vivo measurements study.

Last but not the least; I would like to thank my family: my parents Ramachandra Rao Kavuri and Parvathi, for giving birth to me at the first place, encouraging me to do PhD and supporting me throughout my life.

August 11, 2014.

Abstract

DEVELOPMENT OF TRANS-RECTAL ULTRASOUND (TRUS)
COUPLED DIFFUSE OPTICAL TOMOGRAPHY (DOT)
FOR PROSTATE CANCER IMAGING

Venkaiah Chowdary Kavuri, PhD

The University of Texas at Arlington, 2014

Supervising Professor: Hanli Liu

Prostate cancer is one of the leading causes among cancer deaths in men in the United States. A minimally invasive real time searching tool for cancer need to be developed, which can enhance the odds of cancer detection; Current diagnostic techniques such as Trans-rectal ultrasound (TRUS) suffers from low sensitivity and specificity. The goal of the dissertation is to develop a Trans-Rectal Ultrasound (TRUS) coupled Diffuse Optical Tomography (DOT) probe that can detect and image prostate cancer. To accomplish the task, an optical clip-on probe has been designed that can incorporate the existing ultrasound probe and can pass through the rectum. Next, a multi-step reconstruction technique has been developed by combining the piecewise cluster reconstruction and hard prior reconstruction methods. Optical properties of ex-vivo prostate specimens also have been measured. Finally, Clip-on optical probe is tested by utilizing prostate cancer animal models.

The clip-on probe has been successfully tested using computer simulations and laboratory phantoms. In experiments, a hidden absorber without prior location information was reconstructed with a recovery rate of 100% in its location and 83% in its optical property. The result from ex-vivo specimen study indicates cancer tissues carry different

optical signatures from the benign tissues. Change in light scattering from benign to cancer tissues is more noticeable or prevailing than that in absorption. Animal study successfully validated the functioning of the clip-on probe by reconstructing the images during gas stimulus.

Table of Contents

Acknowledgements iii

Abstract iv

List of Illustrations x

List of Tables xvi

Chapter 1 Introduction 1

1.1 Prostate Cancer Screening 5

1.2 Prostate Imaging Techniques 7

1.3 Rationale of This Thesis 10

1.4 Organization of This Thesis 11

Chapter 2 Methods in Diffuse Optical Tomography 12

2.1 Introduction 12

2.2 Optical Absorption 12

2.3 Optical Scattering 13

2.4 Problems in Diffuse Optical Tomography 15

2.4.1 Forward Problem in Diffuse Optical Tomography 15

2.4.2 Inverse Problem in Diffuse Optical Tomography 23

2.4.3 Inclusion of Spatial-Priors in the Inverse Problem 26

2.4.4 Stopping Criterion 27

2.5 Conclusion 28

Chapter 3 Enhancing Resolution of DOT with Sparse Regularization and Depth Compensation 29

3.1 Introduction 29

3.2 Methods 29

3.2.1 Depth compensation method (DCA) 29
3.2.2 Combination of DCA with L2 Regularization 30
3.2.3 Combination of DCA with L1 Regularization 31
3.2.3 Implementation of Combined DCA with L1 Regularization 34
3.3 Experiments 35
3.3.1 Fiber-Based DOT Imager 36
3.3.2 Camera-Based DOT Imager 37
3.3.3 Measurement Metrics 39
3.4 Results 40
3.4.1 Results from Tissue Phantom experiments 40
3.5 Applications of DCA-L1 Method for Human Brain in-vivo Measurements 44
3.6 Application to Prostate Imaging 48
3.7 Discussion 50
3.8 Conclusion 52
Chapter 4 Hierarchical Clustering Method to Image Prostate Cancer Using Diffuse Optical Tomography 54
4.1 Introduction 54
4.2 Methods 56
4.3. Simulation and Experiment Results 62
4.3.1 Trans-rectal DOT Image Reconstruction by HCM with Limited Prior Information 62
4.3.2 Investigation of HCM on Depth Sensitivity 66
4.3.3 Trans-rectal DOT Image Reconstruction by HCM with Two Absorbers 67

4.3.4 Investigation of HCM on Effects of Different Background (Prostate Region) Contrast 68
4.3.5 Investigation of HCM on Effects of Different Noise Levels 70
4.4 Discussion 71
4.4.1 Investigation and Confirmation of HCM by Simulations 71
4.4.2 Potential Usefulness of HCM for PCa Detection and Diagnosis 73
4.4.3 Limitation of the Method and Future Work 74
Chapter 5 Development of Optical Clip-On Rectal Probe for Existing TRUS Transducer 77
5.1 Introduction 77
5.2 Design 1 78
5.2.1 Validation 80
5.3 Design 2 83
5.3.1 Validation of Clip-On Probe 85
5.4 Conclusion 89
Chapter 6 Measurement of Bulk Optical Properties of Ex-vivo Prostate Tissues 90
6.1 Introduction 90
6.2 Experimental Methods 93
6.3 Statistical Analysis: 95
6.4 Results 96
6.5 Discussion 104
6.6 Conclusion 110
Chapter 7 Imaging hemodynamics of prostate cancer during gas stimulus 111
7.1 Introduction 111

7.2 Experimental Methods 112
7.2.1 Animal preparation 112
7.2.2 Instrumentation 114
7.2.3 Image Reconstruction 114
7.3 Results 115
7.4 Discussion and Conclusion 119
Chapter 8 Concluding Remarks 120
8.1 Conclusion 120
8.2 Contributions of This Work 121
8.3 Limitations and Future Scope 121
Chapter 9 References 125
Biographical Information 136

List of Illustrations

Figure 1-1 Anatomy of prostate 2

Figure 1-2: Zonal anatomy of prostate 3

Figure 2-1: Figures illustrating forward and inverse problems in diffuse optical tomography 15

Figure 2-2: Processes in radiative transport equation 16

Figure 3-1: A schematic illustration of how different regularization terms lead to sparse and non-sparse solutions (A) L1 regularization corresponds to the diamond shaped ball centered on the origin. (B) L2 regularization corresponds to the spherical ball centered on the origin. 32

Figure 3-2: Experimental setup showing the locations of absorbers, bifurcated source-detector configuration and slices used for image reconstruction. 36

Figure 3-3: (a) Experimental setup; (b) light sources and CCD-camera configuration used 38

Figure 3-4 Reconstructed images of two objects placed symmetrically around the center of X-Y plane and at Z= -3 cm (See Fig. 1 for geometry details). (a) and (b) were obtained with DCA-L1 and plotted in X-Z and X-Y plane, respectively; (c) and (d) were obtained with DCA-L2 and also plotted in X-Z and X-Y plane, respectively; (e) and (f) were obtained with L1 only and also plotted in X-Z and X-Y plane, respectively. The dashed circles in each panel indicate the true size and location of the absorbers to be reconstructed. The reconstructed images are normalized between 0 and 1. 41

Figure 3-5: Reconstructed images of two objects placed symmetrically around the center of X-Y plane and at Z= -2 cm (see Fig. 2 for the measurement geometry setup). (a) and (b) were obtained with DCA-L1 regularization, in X-Z and X-Y plane, respectively; (c) and (d) were obtained with DCA-L2 regularization and also plotted in X-Z and X-Y plane,

respectively. The dashed circles in each panel indicate the true size and location of the absorbers to be reconstructed. The reconstructed images are normalized between 0 and 1. 42
Figure 3-6 (a) placement of optodes on the subject's head; (b) S-D (Source-detector) configuration showing optode separations. 46
Figure 3-7: 2D slices (2.5 cm below the scalp surface) of reconstructed human brain images induced by finger tapping tasks. It shows a localized area with (a) an increase in oxy-hemoglobin concentration and (b) a decrease in deoxy-hemoglobin concentration when DCA-L1 is applied. In contrast, a larger or more diffused region is observed with (c) an increase in oxy-hemoglobin and (d) a decrease in deoxy-hemoglobin concentration when DCA-L2 is utilized for image reconstruction. 47
Figure 3-8 (a) Simulation setup and probe geometry utilized to check the feasibility of L1-DCA in PCa imaging. (b) Dotted circles indicate the six locations of absorber used for testing. 49
Figure 4-1: Steps or a flow chart showing HCM 58
Figure 4-2 Geometrical illustration of clustering 59
Figure 4-3: (a) Probe geometry used in this study; each optode is bifurcated to serve as a source and detector. (b) Mesh (elements not highlighted) has been rotated and sliced vertically into two halves to show the simulation geometry. (c) A slice from the mesh cut along the longitudinal direction, showing simulated rectum wall (green), surrounding tissue (blue), prostate (sky blue).An anomaly has been created at 1-cm depth from the rectum wall. (d) Image reconstruction in progress, showing clusters within the prostate region. 63
Figure 4-4: reconstructed μa values in mm-1 using different reconstruction steps for (a) an anomaly located within a simulated prostate. The dotted circles indicate the real

locations of the anomaly. Reconstructed images (b) after Step 1 of HCM, (c) after Step 2 of HCM, (d) after Step 3 of HCM, (e) after Step 4 of HCM. (f) Reconstructed image for the same case using a known hard prior for the inclusion. 64
Figure 4-5: (a) shows the two anomalies separated by 2 cm and created at a depth of 2 cm; (b) shows the two anomalies separated by 4 cm and located at depths of 1 cm and 2 cm. Dotted circles show the actual locations of the anomalies..... 66
Figure 4-6: (a) shows the two anomalies separated by 2 cm and created at a depth of 2 cm; (b) shows the two anomalies separated by 4 cm and located at depths of 1 cm and 2 cm. Dotted circles show the actual locations of the anomalies..... 68
Figure 4-7 Comparison of absorption coefficients between the recovered anomaly and the prostate background after Step 2..... 69
Figure 4-8: (a) shows the reconstructed image with 1% noise added to the data and without any anomalies. (b), (c), and (d) show the reconstructed image with 1%, 2%, 3% noise level, respectively. 71
Figure 5-1 Instrumentation and probe setup utilized for laboratory phantom experiment. Eight sources and detectors were used for light delivery and detection. BS: beam splitter; PD: photodiode. 78
Figure 5-2 Flow chart depicting various stages of detection electronics utilized in proposed instrumentation. 79
Figure 5-3 Pictures of the developed instrument 80
Figure 5-4 (a) Experimental setup used in this study. The probe was placed on one side of the tank to avoid contact with the intralipid solution. An absorber was placed 1.5 cm from the probe side of the tank. (b) Photograph showing the experimental setup. (c) Photograph showing the photodiode array. 81

Figure 5-5 reconstructed μa values in mm-1 using (a) regular DOT iterative reconstruction and HCM after (b) step 2, (c) step 3, and (d) step 4. The dashed circles indicate the actual location of the 1-cm absorber with a depth of 1.5 cm below the measurement surface. 82
Figure 5-6 Drawing shows the insertion of TRUS probe into clip-on optical probe 84
Figure 5-7 pictures showing various generations of the optical Clip-on probes developed 84
Figure 5-8: Experimental setup showing the horizontal translation of the probe across the absorber (located at center of the plastic container). Pictures were taken after the experiment. 86
Figure 5-9 Raw data from a channel showing the changes in the data while translation of the clip-on probe 87
Figure 5-10 Panels (a) (b) and(c) shows the reconstructed images which depicts the translation of the absorber (scattering contrast). Dotted rectangles shows the target locations 88
Figure 5-11 Panels (a) (b) and(c) shows the reconstructed images which depicts the translation of the absorber (absorption contrast). Dotted rectangles shows the target locations 88
6-1: (a) Source detector geometry used; (b) showing the actual probe used for the measurement; (c) explaining the measurement procedure 93
Figure 6-2 Bar plot showing the optical scattering of four prostate tissues. Error bars represents standard deviation of the mean. * represents significant differences with Tukey's pairwire comparisons..... 98

Figure 6-3 Bar plot showing the optical absorption of four prostate tissues. Error bars represents standard deviation of the mean. * represents significant differences with Tukey's pairwire comparisons 99
Figure 6-4 Plots (a) and (b) showing studentized deleted t residuals and cutoff values for scattering and absorption. 100
Figure 6-5 Panels (a) and (b) showing the normal probability plots of both scattering and absorption respectively and person correlation coefficient respectively 101
Figure 6-6 Residuals Vs Measurements order 103
Figure 6-7 Residuals Vs Measurements order 103
Figure 6-8 Figure showing pathological slides obtained from biopsy samples. (a) Benign prostate glands (b) Benign prostate glands with stroma (c) PIN (d)Adenocarcinoma (e) Benign prostatic hyperplasia (f) Prostattitis 105
Figure 7-1 (a) Picture showing locations of two probes on rat thighs the two probes have been utilized to record the hemodynamic changes of the tumor and normal muscle. (b) Picture showing the width of the intralipid bag 113
Figure 7-2 Picture showing rats breathing protocol 113
Figure 7-3 Changes in oxy-hemoglobin in cancer and normal tissues 115
Figure 7-4 Changes in oxy-hemoglobin in cancer and normal tissues 116
Figure 7-5 Bar plot showing the magnitude of changes in Oxy-hemoglobin 117
Figure 7-6 Bar plot showing the magnitude of changes in reduced Oxy-hemoglobin during gas challenge between cancer and normal tissues 117
Figure 7-7 (a) (b) and (c) showing the image reconstructions from rats 1,2 and 3 using HCM 118
Figure 8-1: Simulated future probe design showing space for rectangular fibers, self calibrating phantom attached to the probe (red) and 3axis gyroscope(yellow) 122

Figure 8-2 Simulated probe design showing the arrangement of dummy detector for self calibrating probe..... 123

List of Tables

Table 1-1 Summarizing the anatomical location of prostate zones and the fraction of each zone in the total volume of gland and percentage of cancer prevalence in that zone 4

Table 3-1: comparison of DCA-L1 versus DCA-L2 algorithm 43

Table 3-2: Volume ratios and position error at six simulated locations 49

Table 4-1 Comparison of reconstructed μa values by HCM 65

Table 4-2 comparison of reconstructed μ_a value of the target at different depths using HCM 67

Table 5-1 comparison of reconstructed μa value between regular DOT reconstruction and HCM for experimental data. 83

Table 6-1 Table showing number of measurements made per tissue type 96

Table 6-2: Comparison of optical properties of prostate and various wavelengths in literature 109

Chapter 1

Introduction

The rationale for this thesis is to advance the technological capability of near infrared spectral tomography, for prostate cancer imaging. Prostate cancer (PCaa) is one of the leading causes among cancer deaths in men in the United States. American Cancer Society predicts that, about 233,000 new cases of PCaa will be diagnosed and about 29,480 men will die of PCaa in the year of 2014 [1]. The above numbers imply that about 1 in 7 men will be diagnosed with PCaa during his lifetime. PCaa occurs mainly in older men. About six cases in ten are diagnosed in men aged 65 or older, and it is uncommon before age 40. The median age at the time of diagnosis is around 66. The roles of race and family history are significant as well. African American men are 61% more potential to grow PCaa compared with Caucasian men and are nearly 2.5 times as likely to die from the disease. Therefore, it is essential to develop robust clinical methods to find cancer in early phases so that treatment can be planned. Advanced prostate imaging techniques play a very important role in the process of early cancer detection and diagnosis. The following section briefly discusses the anatomy of the prostate and current prominent PCaa diagnostic techniques, to allow the interpretation of imaging PCaa in the appropriate setting.

The prostate is a gland of the male reproductive system. It is located in front of the rectum and just below the bladder (the organ that stores urine) and produces a fluid that forms part of the semen. The prostate surrounds the urethra as it goes out the bladder and merges with the ductus deferens. The seminal vesicles, two little glands that secrete about 60% of the substances that make up semen are located above the prostate. The size of the prostate is about the size of a walnut or lemon, and has roughly conical shape. Anatomical landmarks of prostate consist of a base, an apex, an anterior,

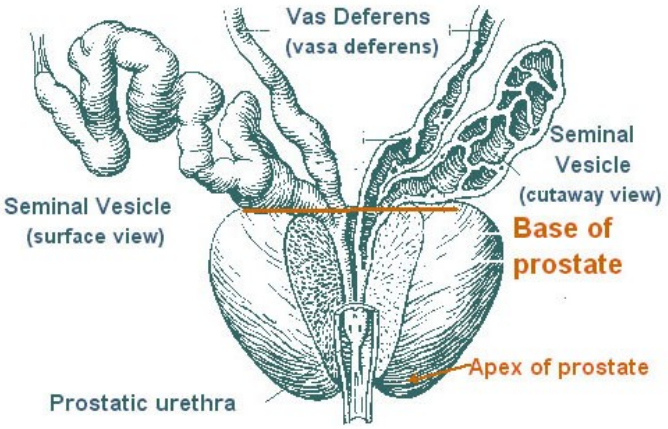

Figure 1-1 Anatomy of prostate

a posterior and two lateral surfaces (see Figure 1.1). The base is directed upward near the inferior surface of the bladder. The greater part of this surface is directly continuous with the bladder wall.

Prostate was also divided majorly into three zones Peripheral Zone (PZ), Central zone (CZ), and Transition Zone (TZ). Peripheral Zone (PZ) covers the dorsal, lateral, and apical parts of the prostate. Transition Zone (TZ) consists of two lobes, located anteriorly between the proximal urethra and the lateral parts of the PZ. Central Zone (CZ) is cone-shaped with its base located at the bladder neck and the tip at the verumontanum (a landmark located near the entrance of the seminal vesicles).

Previous studies show that most cancer lesions (about 68%) occur in the peripheral zone of the gland, fewer occur in the transition zone (24%) and very less in number (8%) arise in the central zone [2-5]. It is also shown that most benign prostate hyperplasia (BPH) lesions develop in the transition zone. The inflammations that appear in the transition zone are associated with BPH nodules and atrophy, and the latter is often present in and around the BPH nodules. Acute inflammation can be salient in both

the peripheral and transition zones, but is rather variable. The inflammation in the peripheral zone occurs in association with atrophy in most cases. Although cancer might involve the central zone, small cancer lesions are nearly never found here in isolation, strongly suggesting that prostatic intraepithelial neoplasia (PIN) lesions do not readily progress to cancer in this zone. Both modest and large cancers in the peripheral zone are often set up in association with high-grade PIN, whereas cancer in the transition zone tends to be of lower class and less often associated with high-grade PIN. The diverse patterns of prostate atrophy, some of which frequently merge directly with PIN and at times with small cancer lesions, are also much more dominant in the peripheral zone, with fewer occurring in the transition zone and very few occurring in the central zone.

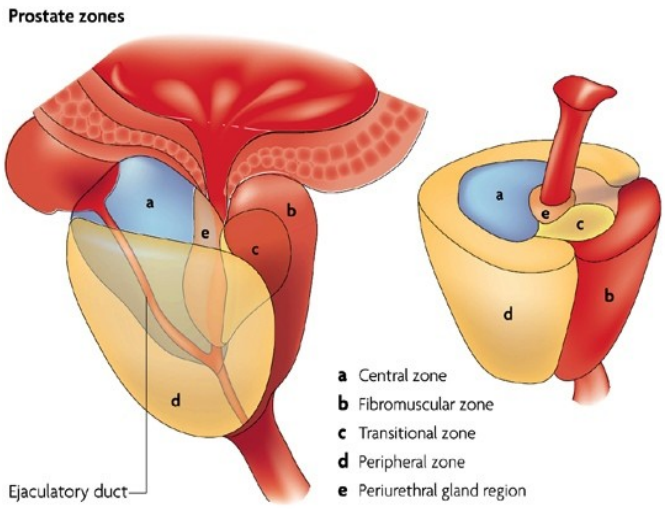

Figure 1-2: Zonal anatomy of prostate

Table 1-1 Summarizing the anatomical location of prostate zones and the fraction of each zone in the total volume of gland and percentage of cancer prevalence in that zone

Zone	Anatomical Location	Fraction of total volume of gland	Percentage of cancer prevalence
Peripheral Zone (PZ)	The sub-capsular portion of the posterior aspect of the prostate gland that surrounds the distal urethra.	Constitutes up to 70% of the normal prostate gland	70% of PCas originate from this portion of gland
Central Zone (CZ)	This zone surrounds the ejaculatory ducts	Constitutes approximately 25% of the normal prostate gland	Central zone tumors account for more than 25% of all PCas.
Transition Zone (TZ)	The transition zone surrounds the proximal urethra and is the region of the prostate gland which grows throughout life and is responsible	Constitutes for 5% of the prostate volume	This zone is very rarely associated with cancer.

1.1 Prostate Cancer Screening

Current PCa screening techniques include serum prostate-specific antigen (PSA), digital rectal examination (DRE) and a combination of these two tests. PSA is a substance produced almost exclusively by certain types of cells located within the prostate gland. The role of PSA is to liquefy the semen following ejaculation. Most of the PSA produced by the prostate gland is carried out of the body in semen, but a very small amount escapes into the blood stream, so PSA is normally found in low amounts (nanograms per milliliter or ng/mL) in the blood [6]. PSA levels in the blood are increased due to disruption of the prostate's cellular architecture. This can occur in due to different prostate diseases, including PCa. Therefore, elevations in PSA may indicate the presence of any kind of prostate disease. The most common cause of PSA elevation includes benign prostatic hyperplasia [7] (BPH = enlargement of the prostate, secondary to a noncancerous proliferation of prostate gland cells) and prostatitis (inflammation of the prostate). Other factors, which elevate PSA levels, include ejaculation, prostate examination, urinary retention or catheter placement, and prostate biopsy. PSA levels less than 4 ng/mL are usually considered "normal," levels over 10 ng/mL are usually considered "high," and results between 4 and 10 ng/mL are usually considered "intermediate."

DRE exam is performed to detect abnormalities that can be felt (palpated) from within the rectum [8]. The physician inserts a lubricated, gloved finger into the rectum and examines the prostate for any irregularities in size, shape, and texture. Usually, an urologist helps to distinguish between PCa and non-cancerous conditions by performing DRE.

Among those exams mentioned above, Prostate specific antigen (PSA) test turns on the alert of PCa very early; The traditional cutoff for an abnormal PSA level in the

major screening studies has been 4.0 ng/mL [9-11]. In a pooled analysis made by American cancer society [12], the estimated sensitivity of a PSA cutoff of 4.0ng/mL was 21 percent for detecting any PCa and 51 percent for detecting high-grade cancers (Gleason ≥8). Using a cutoff of 3.0 ng/mL increased these sensitivities to 32 and 68 percent, respectively. The estimated specificity was 91 percent for a PSA cutoff of 4.0 ng/mL and 85 percent for a 3.0 ng/mL cutoff. PSA has poorer discriminating ability in men with symptomatic benign prostatic hyperplasia [13]. A meta-analysis of DRE estimated a sensitivity for detecting PCa of 59 percent and a specificity of 94 percent [14]. The prostate specific antigen (PSA) and digital rectal examination (DRE) can be considered as complementary, and their combined use can increase the overall rate of cancer detection. As an example, a multicenter screening study of 6630 men reported a detection rate of 3.2 percent for DRE, 4.6 percent for PSA, and 5.8 percent for the two methods combined [15]. PSA detected significantly more of the cancers than digital examination (82 versus 55 percent). Overall, 45 percent of the cancers were detected only by PSA, while just 18 percent were detected solely by digital examination.

With abnormal screening results, the gold standard for PCa diagnosis is a TRUS guided needle biopsy, which involves resection of prostate tissue with the guidance of an ultrasound probe. In TRUS-guided biopsy, a biopsy needle loaded on a automatic biopsy device is commonly used to procure multiple prostate biopsy specimens. The tissue samples have to be taken throughout the prostate at minimum of six sites as a systematic yet random approach. The current standard of prostate biopsy routinely uses 10 to 12 cores of tissue obtained throughout the prostate for the initial assessment. The collected samples will be sent to the pathological examination where the Gleason Score will be given to the sample. A cancer grade (Gleason Score) is to determine the degree how the tumor cells look different from normal cells. It should be noted that the majority of

biopsies are found to be negative, and in men with persistent suspicion of PCa after several negative biopsies, repeated biopsy and more extensive protocols (>12 cores) up to saturation biopsy (24 cores) represent a necessary diagnostic procedure.

1.2 Prostate Imaging Techniques

Several imaging techniques have been applied to prostate imaging. Among them: Ultrasonography, Magnetic Resonance Imaging (MRI), and Positron Emission Tomography (PET) are the main imaging techniques in clinical applications or in the research [16].

Ultrasound imaging (US) is one of the most widely used diagnostic modalities in medicine and uses sounds above the highest audible frequency of 20 KHz is ultrasound. US imaging probe consists of piezoelectric transducer, which is used to generate pulses of high frequency (2 to 10 MHz) and to detect the returning echo signals. Echoes are produced at the boundaries of different tissues where a change in acoustic impedance occurs. The time between the transmission of a pulse and the arrival of an echo is used to estimate the depth to a reflecting tissue surface located below the transducer. The US images reveal the positions of tissue boundaries within the body. The piezoelectric transducer serves as a transmitter and a receiver, where electrical and acoustic signals are converted back and forth by a phenomenon known as peizo-electric effect. US technology is capable of imaging muscle and soft tissue. It has no known long-term side effects and rarely causes any discomfort to the patient. Equipment is widely available, including portable scanners. US imaging is inexpensive compared to MRI or PET.

Magnetic Resonance Imaging (MRI) uses the phenomena of Nuclear Magnetic Resonance (NMR) to allow us to measure the properties of proton (water) within the body. NMR occurs when certain atomic nuclei are placed in a magnetic field and excited by radio waves of a particular frequency. The absorbed energy will be re-emitted

(resonance) after the source is switched off. In order to produce a 3D image, resonance signal must be encoded for each dimension. The encoding in the axial direction is accomplished by adding a gradient magnetic field, which results in the linear change of Larmor frequency to in the axial direction. Thus, an axial slice is selected. The 2D spatial reconstruction in each axial slice is accomplished by spatially varying the frequency (in x-direction) and phase (in y-direction) of the magnetic field gradient. The principle advantage of MRI is its ability to take high spatial resolution 2D or 3D images of the body. The spatial resolution of MRI depends on the desired imaging time. For fast image acquisition, resolution of 2 to 3mm can be obtained and for slow acquisition, resolutions of 400um can be obtained. Nevertheless, of resolution, MRI is a truly non-invasive tool that has proven safe over millions of examinations. On the other hand, MRI scanners are expensive instruments in order to purchase or to maintain. MRI is also a relatively slow technique; a high-resolution image requires longer scanning time. Combined T2 and DWI MRI has been used to detect PCa (Gleason score ≥ 6 and diameter > 4 mm) within the peripheral zone [17]. Endo rectal MRI coil also has been developed but it has lower sensitivity. [18]

Positron emission tomography (PET) is a nuclear-based non-invasive imaging method to obtain biochemical and molecular information from the body. Since the technology is nuclear based radioactive compounds (positron emitters) are needed to be injected into the human body. Several forms of radioactive compounds can be injected, such as (1) gas (for investigating hemodynamics or oxygen metabolism) (2) ligands, (fluorine-18 labeled 2-fluoro-2-deoxy-D-glucose for investigating glucose metabolism) and (3) radio labeled receptor agonist or antagonist to investigate specific receptor function. The physical phenomenon of PET is known as “annihilation”. Briefly, in an unstable nuclide, under the influence of other nucleons the proton is converted into a

neutron, a positron and a neutrino. This results in the ejection of the positron and the neutrino from the nucleus. The ejected positron carries kinetic energy depending on the binding energy in the nucleus and loses it while traveling in the surrounding media. The collision between the positron and an electron (in the surrounding media) is called annihilation. Due to annihilation, the masses of the two particles have completely turned into energy. The energy is divided equally between the two photons (each of 511 keV), travelling in the opposite directions. This released photon pair hit the scintillation crystals connected with coincidence logic. PCas has been imaged with PET with different types of radionuclides. [19,20]

Considering the advantages of imaging speed, system expense and availability of radio nuclides, TRUS remains the first modality of choice for imaging the prostate. On the other hand, greyscale ultrasound has an accuracy of only 50–60% with a positive predictive value as low as 6% for the detection of PCa. Its accuracy for local staging is also relatively poor. 60–70% of cancers are echopoor, but only 17–57% of echopoor foci are malignant. 30–40% of cancers are isoechoic and a small percentage is echogenic. Out of all sonographically visible cancers 30% appear as a focal nodule, whereas a focal lesion is accompanied by an infiltrative component in 50% and an infiltrative pattern predominates in approximately 20% [21]. Since there are no significant biological differences noted between isoechoic and hypoechoic PCas, TRUS does not reliably differentiate neoplastic from benign tumors. Improving the cancer detection rate using TRUS-guided biopsy requires TRUS imaging be augmented or aided with a potentially pathognomonic indicator of PCa development that can be detected non-invasively.

Near infrared light, with wavelengths between 600-1000 nm is harmless for imaging thick soft tissue. The main advantage of NIR imaging is providing functional properties of the tissue, which can be used to diagnose the tissue. Light absorption and

light scattering are the physical phenomena responsible for providing the functional information about the tissue. Diffuse optical tomography (DOT) is a non-invasive imaging modality which uses near infrared (NIR) light and provide functional images about the tissue. Since cancer has more vasculature than the surrounding tissue, hemoglobin-based absorption in tumors provides optical contrast in DOT. When imaged at multiple wavelengths, DOT is capable of measuring chromophores concentrations, such as Oxy-hemoglobin, deoxy-hemoglobin, and water, ICG etc. Usage of DOT for breast cancer detection and diagnosis has been extensively studied for nearly 20 years. For PCa, previous ex-vivo studies reported a vasculature gradient in malignant versus benign tissue. Several recent studies have shown promise of trans-rectal DOT as a possible imaging tool for PCa detection and diagnosis.

1.3 Rationale of This Thesis

The strength of diffuse optical tomography is providing functional information about tumors and weakness is lack of proving anatomical images. NIR based DOT imaging suffers from having a relatively poor spatial resolution, about 1cm. Because many immature tumors are small, DOT may not be able to identify them when being used clinically as a stand-alone approach. Moreover, PCa measurements are endoscopic the weakness of DOT makes the measurements blind folded. We cannot identify the exact anatomical location from where the image has been recorded. In order to overcome the problem, an optical clip-on type attachment for existing ultrasound transducer need to be developed. The advantage of the clip-on type attachment is two folded. First, the combination with ultrasound imaging system renders accurate and real-time anatomic information to correlate NIR optical system. Second, the available prior information will be inducted into the reconstruction algorithm to make it more robust. Although inducing hard prior information improves accuracy of reconstructed DOT images, it relies highly on the

ability of TRUS to locate the PCa lesion. Given that TRUS has low PCa detection accuracy and that each region is assumed homogeneous, the reconstructed DOT images of PCa could be erroneous. Overall, this thesis focuses on (1) development of hybrid reconstructive technique by combining or modifying existing reconstruction techniques. (2) Development of TRUS compatible optical clip-on probe. (3) Measuring optical properties benign and cancer tissues in ex-vivo prostate specimen. (4) Validation of clip-on probe by utilizing PCa animal models.

1.4 Organization of This Thesis

Chapter 1 is a brief introduction of the PCa and commonly used PCa imaging and diagnostic methods. In Chapter 2, a review of the NIR diffuse optical tomography describes the optical imaging reconstruction algorithm in detail. In chapter 3, a combined approach of depth compensation algorithm (DCA) with L1 regularization (DCA-L1) to improve the spatial resolution and depth localization of DOT is explored; Hierarchical clustering method (HCM) has been developed to improve the accuracy of image reconstruction with limited prior information has been explored in chapter 4. Chapter 5 discusses about development of portable diffuse optical imaging system and designing the optical clip-on probe for an existing TRUS transducer. In Chapter 6, optical properties of PCa and benign tissues in ex-vivo specimens measured using a frequency domain system. Chapter 7 discusses about testing the clip-on probe by using animal models. Chapters 8 conclude the thesis and provide directions for future work.

Chapter 2

Methods in Diffuse Optical Tomography

2.1 Introduction

When light propagates in biological media, it will interact with the tissue constituents. The two fundamental interactions are elastic scattering and absorption, which are responsible for determining the photon distribution within the medium. These theoretical properties define how the light propagates through the tissue. Absorption depends on the presence of endogenous or exogenous chromophores within the medium, whereas scattering (elastic) depends on microscopic discontinuities in the refractive index of the tissue. When a tissue is irradiated, a stream of discrete photons will enter into the tissue. The photons will propagate in their initial direction until they strike a scatter, which changes its trajectory and continue to propagate in the tissue until it is eventually remitted across a boundary or get absorbed by an absorber. The metrics for absorption and scattering are the absorption coefficient (probability per unit length of photon being absorbed completely) and scattering coefficient (probability per unit length for an elastic scattering event) respectively. In this chapter, fundamentals of diffuse optical tomography will be discussed.

2.2 Optical Absorption

Optical absorption is a process in which the energy of a photon is taken up by the electrons of an atom. Thus, the electromagnetic energy is transformed into internal energy of the absorber such as thermal energy. The fundamental transitions in a molecule are electronic and vibrational transitions. Electronic transition allows electrons to move freely up and down the different energy levels (or quantum states). In vibrational transition, the nuclei of the atoms within a molecule vibrate resonantly with wavelengths

in the infrared spectrum. For an optically absorbing medium, the relation between the attenuation of light power I and the optical path-length L is given by the following equation

$$\frac{I}{I_o} = e^{-\mu_a L} \qquad 2.1$$

Where I is the light intensity after passing through the medium and I_0 is the incident light intensity, L (mm) is the optical path length, and μ_a is the absorption coefficient (mm-1). Optical absorption is related to the concentration C of those absorbing chromophores in the medium, which can be expressed as

$$\mu_a(\lambda) = \varepsilon_1(\lambda) \bullet \mathrm{c}_1 + \varepsilon_2(\lambda) \bullet \mathrm{c}_2 \cdots \quad _n \backslash \ / \bullet \mathrm{c}_n = \sum_{i=1}^{n} \varepsilon_i(\lambda) \bullet \mathrm{c}_i \qquad 2.2$$

Equation 2.1 becomes

$$\frac{I}{I_o} = e^{-\sum_{i=1}^{n} \varepsilon_i(\lambda) \bullet \mathrm{c}_i \bullet L} \qquad 2.3$$

Where ε_i the extinction coefficient (mm-1/Mol) with respective to different wavelength λ and c_i is the concentration of the species in the medium (Mol).

2.3 Optical Scattering

Tissues are composed of cells where the intracellular organelles and extracellular structures form a complex matrix that macroscopically govern the anatomy of the organs. Evidently there exist numerous of different tissue types each with its own composition of constituents. For example, connective tissues hold collagen and elastin proteins whereas muscular tissues made up of myosin and actin. Irrespective of what tissue type, the origin of scattering is due to the variation of refractive index within the medium. In addition, the size of the tissue components will affect the scattering. This fact

has rendered the use of scattering-based diagnostic methods to probe morphological changes in the tissue.

$$\mu_s^{'} = a\lambda^{-b} \qquad 2.4$$

In the theoretical analysis of scattering properties, the tissue components are considered as spherically shaped particles. The electromagnetic wave propagation is then modeled within the framework of Mie theory. The scattering from one sphere can then be described by the radiation caused by a dipole induced through the interaction with the incident electromagneticfield. Mie theory can very well describe the scattering pattern from a limited number of spheres but the complexity of biological tissues make it impractical to adopt in real applications. Then two physical quantities are defined; the scattering coefficient and the anisotropy factor $g = \langle \cos(\theta) \rangle$, where θ is the scattering angle. g holds the information about what direction, on average, the light is scattered. The composition of tissue renders an anisotropy factor approaching unity meaning that a biological medium is forward scattering. In highly scattering tissues, the two quantities are combined into the reduced scattering coefficient ($\mu_s^{'}$).

$$\mu_s^{'} = \mu_s(1-g) \qquad 2.5$$

2.4 Problems in Diffuse Optical Tomography

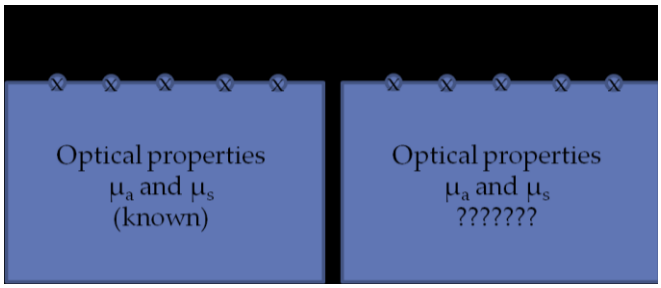

Figure 2-1: Figures illustrating forward and inverse problems in diffuse optical tomography

Diffuse optical tomography (DOT) mainly involves solving two problems, which are illustrated in Fig. 2-1. If μ_a and μ'_s represent the absorption and reduced scattering coefficients of tissue, then the forward problem involves generating the boundary data (y), for a given set of optical properties (μ_a and μ'_s) within the tissue, using a model for light transport in tissue. The solving inverse problem involves reconstructing the optical properties (μa and μs) given the boundary data (y). Unlike many imaging modalities, such as X-ray Computed Tomography (CT), the inverse problem is ill-posed due to dominance of light scattering in the tissue over the absorption. Moreover, the inversion problem can be seriously under-determined, so solving the inverse problem can involve computationally expensive algorithms.

2.4.1 Forward Problem in Diffuse Optical Tomography

As the electromagnetic wave propagation described by Maxwell's equations, the fundamental forward model for photon transport through diffuse media is the radiative transport equation (RTE). The transport theory is a heuristic approach and directly deals with the transport of energy through a medium. The transport theory considers only the particle nature of light so properties such as Coherence, polarization, interference and

non-linearity effects are neglected. Refractive index, absorption coefficient, scattering coefficient and anisotropy factor are assumed time-invariant but space variant. The derived model is stationary in nature. In a medium, photons are either scattered elastically by particles of the medium or absorbed. Next, fundamental quantities such as

Photon distribution, Radiance, Fluence rate and photon flux is explained.

Photon distribution $N(r,\hat{s},t)[1/m^3 sr]$ is the number of photons per unit volume at a position r, propagating in direction $\hat{s}$ within a solid angle $d\omega$ at a specific time t.

Radiance $L(r,\hat{s},t) = h\upsilon cN \quad [W/m^2 sr]$ is the power per steradian and per unit area where *h* is Planck's constant, is the frequency of the light and *c* is the speed of light in the medium.

Fluence rate $\Phi(r,t) = \int_{4\pi} L(r,\hat{s},t)dw \quad [W/m^2 sr]$ is the power per unit area at a given time at a certain position. It is related to the photon density ([$\rho[1/\mathrm{m}^3]$]) through

$\Phi(r,t) = h\nu c\rho(\mathrm{r},\mathrm{t})$

Figure 2-2: Processes in radiative transport equation

Photon flux $\Phi(r,t) = \int_{4\pi} L(r,\hat{s},t)\hat{s}dw \quad [W/m^2]$ is a vector quantity.

RTE is an energy balance equation that can be calculated by considering a small volume V with boundary S and an outward pointing unit normal $\hat{n}$. Let N be the photon distribution as defined previously. According to the energy conservation principle, considered in a direction $\hat{s}$, the net change must be equal the difference between the inward and outward travelling photons. Within the volume, photons are lost and gained through the processes depicted in Fig. 2.2.

The net change of the photon distribution is given by

$$\int_V \frac{\partial N}{\partial t}\partial = .. \qquad 2.6$$

Photon gain

$$+\underbrace{\int qdV}_{i)} + \underbrace{\int c\mu_s \int p(\hat{s}',\hat{s})Nd\omega' dV}_{ii)} \ldots \qquad 2.7$$

Here (i) is Photon gain due to sources inside the volume where q is $q(r,\hat{s},t) \quad [1/smm^3sr]$ is the number of photons emitted per unit volume, time and steradian.

(ii) is photon gain due to scattering from a propagation direction $\hat{s}'$ to the direction $\hat{s}$ where μ_s is $\mu_s(r) \quad [1/mm]$ is the scattering coefficient.

Photon loss

$$\underbrace{-\int cN\hat{s}\hat{n}ds}_{iii)} \underbrace{-\int c\mu_s NdV}_{iv)} \underbrace{-\int c\mu_a NdV}_{v)} \tag{2.8}$$

Photon loss due to photons crossing the boundary. Here Gauss' theorem has been utilized so that the surface integral can be transferred to a volume integral according to

$$-\int_s cN\hat{s}\hat{n}ds = -\int_V c\nabla N \cdot\hat{s}dV \tag{2.9}$$

Photon loss due to scattering is photon gain due to absorption from a propagation direction where μ_a is $\mu_a(r)$ $[1/mm]$ is the absorption coefficient.

$$\frac{1}{c}\frac{\partial L(r,\hat{s},t)}{\partial t} + \nabla .L(r,\hat{s},t)\hat{s} + (\mu_a + \mu_s)L(r,\hat{s},t) = \ldots$$
$$\ldots\ldots\ldots\ldots\ldots\ldots\ldots\ldots\int_{4\pi} L(r,\hat{s},t)p(\hat{s}',\hat{s}) + S(r,\hat{s},t) \tag{2.10}$$

The scattering phase function $p(\hat{s}',\hat{s})$ describes the probability for scattering in any direction. It is a function of the angle between the incoming propagation direction $(\hat{s})$ and the scattered propagation direction $(\hat{s}')$. Hence $p(\hat{s}',\hat{s}) = p(\theta)$ where θ is the scattering angle. The simplest choice of $p(\theta)$ is the isotropic phase function, i.e

$$p(\theta) = \frac{1}{4\pi} \tag{2.11}$$

Photons affected by a scattering phase function of the form in Equation (2.11) will have equal probability to scatter in any direction. Biological tissues are forward scattering. Hence the scattering phase function should adopt another form. There exist several alternatives but the most commonly applied is the Heyney-Greenstein phase function

$$p(\theta) = \frac{1}{4\pi} \frac{1 - g^2}{(1 + g^2 - 2g\cos(\theta))^{3/2}} \qquad 2.12$$

In Equation (2.12) the scattering anisotropy factor is defined through $g = \langle \cos(\theta) \rangle$, meaning the average of the cosine of the scattering angle. Solving the RTE implies finding the radiance in every location as well as every direction of an arbitrary object. Due to limited computational power, RTE should be simplified.

The standard method for simplifying the radiative transport equation is to expand radiance, source term and phase function into an infinite series of spherical harmonics. Then infinite series will the coupled into Equation (2.10) resulting infinite set of coupled equations. In the first order (P1) approximation, spherical harmonics are truncated at the first degree, resulting in the following equation,

$$L(r,s,t) \approx \frac{1}{4\pi}\Phi(r,t) + \frac{1}{4\pi}F(r,t)\cdot\hat{s} \qquad 2.13$$

The first term on the RHS in Equation (2.13) is isotropic and the second term is linearly anisotropic. Utilizing P1 approximation implies that light does not have any directionality and considered as diffused light. Inserting equation 2.13 in RTE results in the following coupled equations,

$$\left(\frac{1}{c}\frac{\partial}{\partial t} + \mu_a\right)\Phi + \nabla F = q_0 \qquad 2.14$$

$$\left(\frac{1}{c}\frac{\partial}{\partial t} + \mu_a + \mu_s^{'}\right)F + \frac{1}{3}\nabla\Phi = q_1 \qquad 2.15$$

In the above equation $\mu_s^{'} = (1-g)\mu_s$ and by assuming (i) only isotropic sources exist (implies q_1 =0) and (ii) Temporal change in the flux is negligible $\frac{\partial F}{\partial t} = 0$ results in $\mu_s^{'} >> \mu_a$

$$F = -\frac{1}{3(\mu_a + \mu_s^{'})}\nabla\Phi = -D\nabla\Phi \qquad 2.16$$

Substituting the equation 2.16 into equation 2.15 results in to the diffusion equation

$$\frac{1}{c}\frac{\partial\varphi(r,t)}{\partial t} - \nabla D(r)\nabla\Phi(r,t) + \mu_a(r)\Phi(r,t) = q_0(r,t) \qquad 2.17$$

By performing the Fourier transform in time ($\frac{\partial}{\partial t} \rightarrow i\omega$) of this equation 2.17 , the frequency domain diffusion equation is obtained,

$$\frac{1}{c}i\omega\varphi(r,t) - \nabla D\nabla\Phi(r,t) + \mu_a(r)\Phi(r,t) = q_0(r,t) \qquad 2.18$$

Rearranging the terms in the above equation results in

$$\nabla D(r)\nabla\Phi(r,t) + \Phi(r,t)\left(\frac{i\omega}{c} + \mu_a(r)\right) = q_0(r,t) \qquad 2.19$$

The above equations can be solved using (1) Analytical methods (2) Monte-carlo methods or (3) Numerical methods.

Analytical Methods: Equations 2.18 and 2.19 can be solved analytically using Green's function approach. A Green's function is the solution when the source is treated as spatial and temporal delta-function. The solutions for extended sources can be derived by convolution of these Green's functions with the source distributions and are easy to compute. The main problem with this method is that the solutions only exist for simple

homogeneous geometries or for media that include a single spherical perturbation. In some cases like layered slab media, these solutions were derived for time-domain DE.

Monte-Carlo Methods: The Monte-Carlo (MC) simulation is one of the stochastic methods used for modeling transport of photons through tissue, such as random walk or Markov-chain models. Practically the photons are treated as photon packages with an initial weight. When launched into the scattering medium the propagation direction is sampled from a distribution given by the scattering phase function. The photon is then moved a step with length. After the move, the weight is decreased by a fraction whereas the leftover is logged as absorption. This process continues until the photon escapes a boundary or the weight is too small. When the latter occurs either the photon package is terminated or it is given a certain probability to survive. If the photon survives, the weight is increased and the propagation continues. A large number, usually 6-10 millions, of photons are required to extract statistically meaningful average quantities such as amplitude and phase in the frequency-domain case. The main advantage of using MC in the forward model is that it is equivalent to solving the RTE. The drawback of these approaches is that they involve more computational time than Analytical or Numerical methods.

Numerical Methods: The Finite Element Method (FEM) is extensively applied to various engineering problems such as fluid mechanics, structural mechanics and electro-magnetism. The methods covered under these techniques include the Finite Difference Method (FDM), finite volume method (FVM), Finite Element Method (FEM), and boundary element method (BEM). Among these FEM is the most popular choice for solving the forward problem in complex cases, like prostate, with irregular boundaries. Classically, FEM has been the popular methods to solve the DOT forward problem. Finite element method is a numerical method to solve partial differential equation characterized by

boundary conditions for complex geometries. The geometrical domain is discretized using sub-domain elements (e.g. triangular elements for 2D geometries). The unknown variable is represented as coefficients in a shape function basis representation. Now, linear matrix equations in these unknown coefficients are obtained using variational or weighted residual schemes. In weighted residual Galerkin scheme, the weight functions are shape functions themselves. Matrices have been formed for each individual element and are assembled to construct the global system matrix, which is solved by conjugate gradient method. (In this work, open source software has been used to solve FEM) The diffusion equation and boundary condition is described as

$$-\nabla\left[\kappa(\vec{r})\nabla\Phi(\vec{r})\right]+\mu_a(\mathrm{r})\Phi(\vec{r})=\mathrm{s}(\vec{r}) \qquad 2.20$$

$$\Phi(\vec{r})+2\,\mathrm{A}\,\kappa(\vec{r})\nabla\Phi(\vec{r})\cdot\hat{\mathrm{a}}_n=-4\Gamma_s(\vec{r}) \qquad 2.21$$

After application of the Galerkin approach, the resulting equation can be written in matrix form as,

$$(\mathrm{K}(\kappa)+\mathrm{C}(\mu_a)+F)\Phi=q+B \qquad 2.22$$

Where,

$$\mathrm{K}_{ji}=\int_{\Omega}\kappa(\vec{r})\nabla N_i(\vec{r})\cdot\nabla N_j(\vec{r})\,d\Omega \qquad 2.23$$

$$C_{ji}=\int_{\Omega}\mathrm{N}_j(\vec{r})N_i(\vec{r})\mu_a(\vec{r})\,d\Omega \qquad 2.24$$

$$F_{ji}=\frac{1}{2A}\int_{\partial\Omega}N_j(\vec{r})N_i(\vec{r})\,dl \qquad 2.25$$

$$q_j = \int_{\Omega} \mathrm{N}_j(\vec{r}) s(\vec{r}) d\Omega \tag{2.26}$$

$$\beta_j = -\frac{2}{A} \int_{\partial\Omega} N_j(\vec{r}) \Gamma_s(\vec{r}) dl \tag{2.27}$$

2.4.2 Inverse Problem in Diffuse Optical Tomography

The DOT inverse problem involves reconstructing the optical properties from the boundary data (Figure 2-1). The inverse problem in DOT is solved by minimizing an objective function (Ω) over the range of optical properties (μ) in the least squares (LS) sense. LS minimization has the effect of reducing high frequency noise, leading to smooth images of optical properties. The next subsection extensively discusses these minimization techniques, giving the mathematical framework.

The objective function for the DOT problem can be defined by the following cost function

$$\Omega = || \mathbf{y} - F(\boldsymbol{\mu}) ||^2 \tag{2.28}$$

where y is the experimental data and F(μ) is the modeled data. F represents a function/governing equation which defines the propagation of light in the tissue. For convenience, we also define

$$\delta = \mathbf{y} - F(\boldsymbol{\mu}) \tag{2.29}$$

Writing equation 2.29 in matrix notation

$$(\mathbf{y} - F(\boldsymbol{\mu}))(\mathbf{y} - F(\boldsymbol{\mu}))^T \tag{2.30}$$

Transpose respects addition or subtraction

$$(y^2 - F(\boldsymbol{\mu})\mathbf{y}^T - \mathbf{y}F(\boldsymbol{\mu})^T + F^2(\mu)) \tag{2.31}$$

The second and third terms of the above equation are equal (a 1X1 matrix and always symmetric) and can be replaced with $-2yF(\mu)^T$ so the equation above becomes

$$y^2 - 2yF(\mu)^T + F^2(\mu)) \quad 2.32$$

The above equation is minimized by setting the first order derivative equal to zero.

$$(-2y\frac{\partial \mathbf{F}(\boldsymbol{\mu})^T}{\partial \mu} + 2F(\mu)\frac{\partial F(\mu)^T}{\partial \mu}) = 0 \quad 2.33$$

$$-2\frac{\partial \mathbf{F}(\boldsymbol{\mu})^T}{\partial \mu}(\mathbf{y} - F(\boldsymbol{\mu})) = 0 \quad 2.34$$

$$\mathbf{J}^T(\mathbf{y} - F(\boldsymbol{\mu})) = 0 \quad 2.35$$

Making a substitution from equation 2.29 in 2.35 gives $\mathbf{J}^T\delta = 0$ 2.36

Next, Imagine a sequence of approximations to μ represented by μ_i, then using a Taylor series on $F(\mu_i)$ and expanding around μ_{i-1} gives(For convenience)

$$F(\boldsymbol{\mu}_i) = F(\boldsymbol{\mu}_{i-1}) + F'(\boldsymbol{\mu}_i - \boldsymbol{\mu}_{i-1}) + \frac{1}{2}F''(\boldsymbol{\mu} - \boldsymbol{\mu}_0)(\boldsymbol{\mu} - \boldsymbol{\mu}_0)^T + \ldots\ldots \quad 2.37$$

Ignoring higher-order terms and linearizing Eq. (2.37)

$$F(\boldsymbol{\mu}_i) = F(\boldsymbol{\mu}_{i-1}) + \mathbf{J}(\boldsymbol{\mu}_i - \boldsymbol{\mu}_{i-1}) \quad 2.38$$

Equation (2.29) can be written in iterative form as

$$\delta_i = \mathbf{y} - F(\boldsymbol{\mu}_i) \quad 2.39$$

Substituting (2.38) in (2.39)

$$\delta_i = \mathbf{y} - F(\boldsymbol{\mu}_{i-1}) - \mathbf{J}(\boldsymbol{\mu}_i - \boldsymbol{\mu}_{i-1})) \quad 2.40$$

Multiplying $\mathbf{J}^T$ on both sides

$$\mathbf{J}^T \delta_i = \mathbf{J}^T ((\mathbf{y} - F(\boldsymbol{\mu}_{i-1}) - \mathbf{J}(\boldsymbol{\mu}_i - \boldsymbol{\mu}_{i-1})) \quad 2.41$$

From equation 2.36 $\mathbf{J}^T \delta = 0$ so Equation 2.41becomes

$$0 = \mathbf{J}^T (\mathbf{y} - F(\boldsymbol{\mu}_{i-1}) - \mathbf{J}(\boldsymbol{\mu}_i - \boldsymbol{\mu}_{i-1})) \quad 2.42$$

$$\mathbf{J}^T (\mathbf{y} - F(\boldsymbol{\mu}_{i-1}) = \mathbf{J}^T \mathbf{J}(\boldsymbol{\mu}_i - \boldsymbol{\mu}_{i-1})) \quad 2.43$$

Making substitution

$$\mathbf{J}^T \delta_{i-1} = \mathbf{J}^T \mathbf{J} \Delta\mu_i \quad 2.44$$

Typically $\mathbf{J}^T \mathbf{J}$ is ill conditioned, a diagonal term is added to stabilize the iteration.

$$\mathbf{J}^T \delta_{i-1} = (\mathbf{J}^T \mathbf{J} + \lambda \mathbf{I}) \Delta\mu_i \quad 2.45$$

where $\Delta\mu_i$ is the update for the parameter in the i[th] step. In practice, λ monotonically decreases with iterations (always > 0). It is important to note that $\mathbf{J}^T \mathbf{J}$ is always symmetric, since $(\mathbf{J}^T \mathbf{J})^T = \mathbf{J}^T (\mathbf{J}^T)^T = \mathbf{J}^T \mathbf{J}$.

$$J = \begin{bmatrix} \frac{\delta \ln I_1}{\delta D_1} & \frac{\delta \ln I_1}{\delta D_2} & \cdots & \frac{\delta \ln I_1}{\delta D_{NN}} & \frac{\delta \ln I_1}{\delta \mu_{a1}} & \frac{\delta \ln I_1}{\delta \mu_{a2}} & \cdots & \frac{\delta \ln I_1}{\delta \mu_{aNN}} \\ \frac{\delta \theta_1}{\delta D_1} & \frac{\delta \theta_1}{\delta D_2} & \cdots & \frac{\delta \theta_1}{\delta D_{NN}} & \frac{\delta \theta_1}{\delta \mu_{a1}} & \frac{\delta \theta_1}{\delta \mu_{a2}} & \cdots & \frac{\delta \theta_1}{\delta \mu_{aNN}} \\ \frac{\delta \ln I_2}{\delta D_1} & \frac{\delta \ln I_2}{\delta D_2} & \cdots & \frac{\delta \ln I_2}{\delta D_{NN}} & \frac{\delta \ln I_2}{\delta \mu_{a1}} & \frac{\delta \ln I_2}{\delta \mu_{a2}} & \cdots & \frac{\delta \ln I_2}{\delta \mu_{aNN}} \\ \frac{\delta \theta_2}{\delta D_1} & \frac{\delta \theta_2}{\delta D_2} & \cdots & \frac{\delta \theta_2}{\delta D_{NN}} & \frac{\delta \theta_2}{\delta \mu_{a1}} & \frac{\delta \theta_2}{\delta \mu_{a2}} & \cdots & \frac{\delta \theta_2}{\delta \mu_{aNN}} \\ \vdots & \vdots & \ddots & \vdots & \vdots & \vdots & \ddots & \vdots \\ \frac{\delta \ln I_{NM}}{\delta D_1} & \frac{\delta \ln I_{NM}}{\delta D_2} & \cdots & \frac{\delta \ln I_{NM}}{\delta D_{NN}} & \frac{\delta \ln I_{NM}}{\delta \mu_{a1}} & \frac{\delta \ln I_{NM}}{\delta \mu_{a2}} & \cdots & \frac{\delta \ln I_{NM}}{\delta \mu_{aNN}} \\ \frac{\delta \theta_{NM}}{\delta D_1} & \frac{\delta \theta_{NM}}{\delta D_2} & \cdots & \frac{\delta \theta_{NM}}{\delta D_{NN}} & \frac{\delta \theta_{NM}}{\delta \mu_{a1}} & \frac{\delta \theta_{NM}}{\delta \mu_{a2}} & \cdots & \frac{\delta \theta_{NM}}{\delta \mu_{aNN}} \end{bmatrix} \quad 2.46$$

It is also important to realize that in frequency domain reconstruction, for simultaneous reconstruction of D and μa, Jacobian takes the form of Eq. 2.46 [22]. In CW, case Jacobian takes the form of Eq. 2.47

$$J = \begin{bmatrix} \frac{\delta \ln I_1}{\delta \mu_{a1}} & \frac{\delta \ln I_1}{\delta \mu_{a2}} & \cdots & \frac{\delta \ln I_1}{\delta \mu_{aNN}} \\ \frac{\delta \ln I_2}{\delta \mu_{a1}} & \frac{\delta \ln I_2}{\delta \mu_{a2}} & \cdots & \frac{\delta \ln I_2}{\delta \mu_{aNN}} \\ \vdots & \vdots & \ddots & \vdots \\ \frac{\delta \ln I_{NM}}{\delta \mu_{a1}} & \frac{\delta \ln I_{NM}}{\delta \mu_{a2}} & \cdots & \frac{\delta \ln I_{NM}}{\delta \mu_{aNN}} \end{bmatrix} \qquad 2.47$$

The initial guess (μ_0) should be close to the actual solution. Even though $J^T J$ is not positive definite (numerically, it is almost singular) in DOT due to the ill-conditioned nature of the problem, the LM approach has been used successfully in a number of instances.

2.4.3 Inclusion of Spatial-Priors in the Inverse Problem

Because of the interest in using spatial information derived from conventional imaging modalities in the DOT inverse problem, a number of methods have been presented in the literature. This multimodality optical imaging, for example, combining MRI with NIR, can provide high-resolution functional images, especially, for breast cancer imaging. These multimodal image reconstruction techniques were initially proposed by Schweiger et al [23]and used in to improve the quantitative outcome of reconstructed images. Li et al [24] used an X-ray tomosynthesis volume to segment the breast into different sub-regions and used different regularization parameters depending on the size of the sub-regions.. Pogue and Paulsen [25], Brooksby et al [26], Yalavarthy et al [27] have extended these approaches for the use of anatomical prior information in which, depending on the connectivity and size of the sub-region, the regularization term was

scaled. Xu et al [28]. studied the combined TRUS and DOT approach for imaging PCa using the anatomical information from ultrasound to reduce the number of unknowns in the DOT image reconstruction. Overall, the LS minimization schemes using spatial priors can be broadly classified into two approaches. (1) Soft-Priors (2) Hard-Priors. The following two subsections will discuss these two approaches.

Soft priors approach mainly uses Tikhonov minimization scheme, in which the L-matrix encodes spatial information. Since soft priors approach is out of scope of this thesis, I am not discussing about the technique. The mathematical details can be found in [29].

Reduction of parameter space to the number of regions segmented from a high resolution imaging modality is known as hard-priors [30]. The estimation optical properties (D and μa) in this procedure are performed through LM minimization. The update equation in this case is given by Eq. 2.16, with Jacobian (J) having dimension of (2*NM) x (2*NR) instead of (2*NM) x (2*NN). In here, NM, NN and NR represent the number of measurements, number of FEM nodes, and number of regions, respectively. The multiplication factor 2 in the dimensions results from the treatment of amplitude and phase separately for the frequency-domain signal, and the estimated parameters being D and μa. The main advantages of this method are: The problem is well-determined, which also implies $J^T J$ is positive definite and computationally efficient. The limitations include: The effect of error or uncertainty in the spatial priors may be amplified by the Technique. The DOT problem may still be ill-posed (and ill-conditioned) after the constraints are added.

2.4.4 Stopping Criterion

The importance of the stopping criterion in an iterative procedure is very high. In any non- linear least-squares based algorithm, experimental data (y) are matched with modeled data (G (μ)) iteratively within the limit approaching a preset value, which is

based on the expected noise level in y. Another approach is to base the stopping criterion on the first-order condition, which in the limit ensures that the problem has reached the global minima. The iterative procedure is stopped when the L2-norm of the data-model misfit (δ) does not improve by more than a certain percentage (in this work, from 20% to 2%). Most usually, the stopping criterion based on the L2-norm of the data-model misfit (δ) is used mainly due to the computational cost required in finding the L2-norm of first order condition.

2.5 Conclusion

In this chapter, basics of diffuse optical tomography have been extensively discussed. Diffuse optical tomography (DOT) mainly involves solving forward and inverse problems. The forward problem involves generating the boundary data, for a given set of optical properties within the tissue, using a model for light transport in tissue. The solving inverse problem involves reconstructing the optical properties given the boundary data. In next two chapters, modification of jacobian matrices will be discussed.

Chapter 3

Enhancing Resolution of DOT with Sparse Regularization and Depth Compensation

3.1 Introduction

In this study, a combined approach of depth compensation algorithm DCA with L1 regularization (DCA-L1) to improve the spatial resolution and depth localization of DOT has been explored. In the combined approach, the reconstructed images are obtained by using L1 regularization technique after modifying the Jacobian or sensitivity matrix by DCA. Specifically, to validate the proposed the DCA-L1 approach, I conducted laboratory phantom experiments using (1) a fiber-based, multichannel DOT system and (2) a camera-based DOT imaging system. Then, a comparison of the reconstructed DOT images using DCA-L1 and DCA with L2 regularization (DCA-L2), has been made by using the following metrics. (1) Volume ratio and (2) contrast to noise ratio (CNR). After the validation with the phantom experiments, the usefulness of the DCA-L1 method has been further demonstrated by using experimental results taken from a human brain measurement under a finger-tapping protocol. By the end of this chapter, it is concluded that DCA combined with L1 regularization outperforms L2 regularization for DOT image reconstruction.

3.2 Methods

3.2.1 Depth compensation method (DCA)

The number of photons decreases dramatically with the increase in propagation depth, leading to the measurement sensitivity in deep tissue significantly lower than that in superficial tissue. The lower measurement sensitivity for deeper layers results in poor depth resolution and biases reconstructed images towards the superficial layers. In order to overcome this problem, weighted matrix M [31] was introduced and calculated, providing a pseudo-exponential increase in magnitude with depth, to compensate the

sensitivity of A in deeper layers. Unlike other spatially variant regularization (SVR) methods [26] which modify the penalty term of regularization, the weighted matrix M is introduced to directly compensate the sensitivity matrix A. Specifically, the weight matrix M is formed as:

$$M = \begin{bmatrix} M(A_L) & & & & \\ & M(A_{L-1}) & & & \\ & & \ddots & & \\ & & & M(A_2) & \\ & & & & M(A_1) \end{bmatrix}^{\gamma} \quad 3.1$$

Where $M(A_i)$ to $M(A_L)$ represents the maximum singular values for measurement sensitivities within the particular layer *i*, which is decomposed from the forward matrix A; γ is an adjustable power and varies between 0 and 3. From the equation 3.1, it is clear that the maximum singular values are arranged inversely with respect to the matrix A, namely, by the order from the bottom to surface, providing the maximum counterbalance for the deepest layer and vice versa. According to the previous studies, γ=1.2-1.6 [32] is considered to be appropriate for high-quality DOT images to recover embedded objects in deep tissue. In this study, I used a medium γ value of 1.3. The adjusted sensitivity matrix $A^{\#}$ is defined as $A^{\#}$=AM; the modified inverse problem is given by

$$y = A^{\#}x. \quad 3.2$$

3.2.2 Combination of DCA with L2 Regularization

Similar to conventional matrix ***A***, $\boldsymbol{A}^{\#}$ is also under-determined and ill-posed, because the number of measurements are usually much fewer than the number of voxels

to be reconstructed, as given in Equation 3.3 . Regularization techniques are often needed to stabilize the inversion of Equation 3.3. In addition, to overcome the ill-posed inverse problem.

In general, regularization techniques involve an addition of a second term that can be adjusted to minimize image artifacts from experimental noise by controlling a regularization parameter at the cost of reducing image spatial resolution. In DOT, the conventional form of regularization used is the L2 norm. Specifically, to solve Eq. (3.3), L2 least squares formulation for DOT can be given as:

$$\min \left\| A^{\#} x - y \right\|_2^2 + \lambda \left\| x \right\|_2^2, \qquad 3.3$$

where λ >0 is the regularization parameter and $\| \ \|_2^2$ denotes L2 norm. Eq. (3.3), has an analytical solution, which can be solved directly or iteratively [33,34] as given by

$$x = A^{\#T} \left(A^{\#} A^{\#^T} + \lambda I \right)^{-1} y \Rightarrow A^{\#T} \left(A^{\#} A^{\#^T} + \alpha S_{\max} I \right)^{-1} y, \qquad 3.4$$

where ***I*** is the identity matrix, S_{max} is the maximum eigenvalue of $A^{\#} A^{\#^T}$, and α is usually set in the range of 10^{-3} to 10^{-1} to suppress the measurement noise and stabilize the solution. While L2 norm regularization is an effective means of achieving stable solutions for the inverse problem and increasing predictive performance, it doesn't promote sparse, sharp-edge solutions.

3.2.3 Combination of DCA with L1 Regularization

On the other hand, L1 regularization promotes sparse solutions and has been reported for its uses [35,36]. As mentioned earlier, L1 regularization has also been studied for DOT, showing improvements in spatial resolution for sharper-edge images. The objective function of L1-regularized least squares is given by:

$$\min \left\| A^{\#} x - y \right\|_2^2 + \lambda \left\| x \right\|_1 , \qquad 3.5$$

where $\| \ \|_1$ denotes L1 norm. In general, Eq. (3.5) does not have any analytical solution; the quality of the regularized solution depends on the choice of the regularization parameter, which was often selected manually. Also, the quality of reconstructed images depends on the user's judgment. Several automatic methods, such as L-curve method, generalized cross validation method, and Morozov disperency principle, all were reported in [37,38] for this particular task. In this work, I do not intend to develop any new methodology for L1 regularization. Instead, I applied the already developed knowledge and methodology of L1 regularization to DOT image reconstruction. Specifically, I utilized the same approach as that reported by ref. [39] to solve the objective function with L1 regularization. While the details can be found in [39], I explain the basis of L1 regularization and how I executed it briefly as follows.

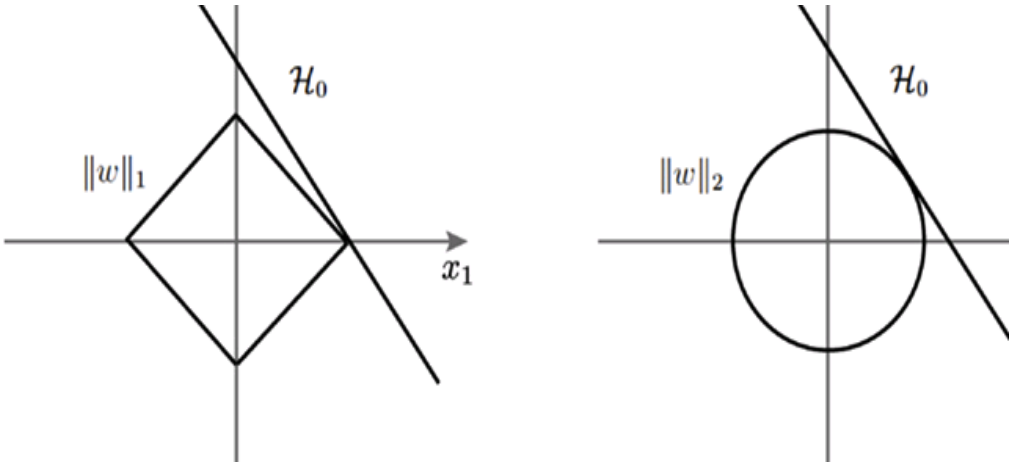

Figure 3-1: A schematic illustration of how different regularization terms lead to sparse and non-sparse solutions (A) L1 regularization corresponds to the diamond shaped ball centered on the origin. (B) L2 regularization corresponds to the spherical ball centered on the origin.

Figure 3-1 provides a geometric intuition of why L1 and L2 regularization lead to sparse and non-sparse solutions, respectively. The solution of L1 or L2 regularized least squares is the intersection of the regularization geometry and a hyper-plane. Figure 3-1 shows the L1 regularization corresponds to the diamond shaped ball centered at the origin. As regularization parameter λ increases, the L1 ball grows and the solution is the point when it hits the hyper-plane. Given the geometry of L1 ball, the solution is more likely to be sparse. Figure 3B shows the L2 regularized logistic regression, where the geometry of the L2 ball is a sphere, therefore leading to a non-sparse solution. We can apply same intuition in DOT by considering x1 and x2 as two variable in the vector x of Eq. (3.2).

In Equation 3.5, A# is the modified sensitivity matrix or Jacobian after incorporating DCA into the objective function, y is the measurement matrix with dimension of NM×1, and λ is the regularization parameter. Eq. (3.5) doesn't have an analytical solution, but can be transformed into a convex quadratic form, which can be solved by standard convex optimization methods, such as interior point methods [39], as given below:

$$\begin{aligned} &\min \left\| A^{\#} x - y \right\|_2^2 + \sum_{i=1}^{n} \lambda u_i; \\ &subject \quad to \quad -u_i \le x_i \le u_i, \quad i = 1, 2, \cdots \end{aligned} \tag{3.6}$$

where the new variable $u \in R^n$ provides constraints on *x*. Next, adding logarithmic barrier penalties results in:

$$t\left\|A^{\#}x-y\right\|_2^2+t\sum_{i=1}^{n}\lambda u_i-\sum_{i=1}^{n}\log\left(u_i+x_i\right)-\sum_{i=1}^{n}\log\left(u_i-x_i\right). \qquad 3.7$$

As *t* varies from 0 to ∞, Eq. (10) converges to an optimal point. Eq. (10) reaches the optimal point by utilizing Newton's steps, NS_{Newton}, and searching directions by pre-conjugate gradient (PCaG) method [23]. Both the number of iterations in PCaG, $NIPCa_G$, and NT_{Newton} have a significant impact on the reconstructed images.

3.2.3 Implementation of Combined DCA with L1 Regularization

Given all the needed mathematical information, our steps to implement the combined DCA-L1 algorithm are described below:

(a) Generate A matrix from PMI (Photon Migration Imaging) toolbox [40];

(b) Modify A matrix to generate the combined matrix of A#=AM according toDCA.

(c) For image reconstruction using L2 regularization, I utilized PMI toolbox [40];

(d) For image reconstruction using L1 regularization, I utilized L1-LS toolbox [41].

(e)

For step 4, with some modification, the L1-LS function can be expressed as x= l1_ls (A#, y, λ, NIPCaG, NSNewton), where x is a vector of NV×1 to cover the 3D image volume, y is again the measurement vector containing the observed data, λ is the regularization parameter, NPCaG are the number of iterations in prec-conjugate gradient method PCaG, NSNewton is no of steps in newton's minimization.

The reason I chose utilizing L1-LS toolbox was that it has been developed, tested, and supported by its publication [39], as well as it has the capability to handle a large set of 3D data and to have a fast computational speed. In practice, I had to address how to determine critical empirical parameters during the regularization process: they were (1)

the regularization parameter, λ (2) the value of gamma, γ, for the weight matrix **M**, (3) the number of iterations in PCaG, NIPCaG, and (4) Newton's steps, NSNewton. The optimal selection of these four parameters determined the final quality of reconstructed DOT images. Based on literature, λ values of 0.1-0.01 were usually chosen, depending on experimental noise levels. Based on our own studies [31,31,32], γ values between 1.2-1.6 were appropriate in order to accurately recover embedded objects in deep tissue. The key issue in DCA-L1 algorithm was how to choose NIPCaG and NSNewton. In this study, I finally selected NIPCaG and NSNewton to be 60 and 15, based on trial and error. The ranges used to choose appropriate values of NIPCaG and NSNewton in the trials were set 20-100 and 10-20, with an increment of 10 and 1, respectively. Specifically, the volume ratio (VR) between the reconstructed and actual objects was calculated for several trails. A large VR served as a good performance criterion since VR was ideally expected to be close to "1". In this way, the selected values of NIPCaG=60 and NSNewton=15 provided us with an optimal VR in our current study. Note that while running the trials to determine optimal values for NIPCaG and NSNewton, values of λ and γ has been fixed to be to be 0.01 and 1.3, respectively.

3.3 Experiments

I utilized laboratory tissue phantoms in order to assess the performance of both DCA-L1 and DCA-L2 regularizations. An optical fiber-based and a CCD-camera-based imager imaged two absorbers embedded inside the tissue phantom. Volumetric image reconstruction was performed using both regularizations. Finally, the reconstructed images were compared and quantified on the basis of VR [42,43] and Contrast to Noise Ratio (CNR) [42,44].

3.3.1 Fiber-Based DOT Imager

The laboratory experiment was performed by utilizing a 32-channel, continuous-wave DOT imager [45] (DYNOT, NIRx Medical Technologies). The system delivers and collects two wavelengths of Laser at 760 nm and 830 nm, sequentially from each optical fiber. For the study, 25 bifurcated optodes were utilized and arranged as a square array of 5x5 (with a separation of 1.4 cm in both x and y direction), which was placed on the surface of the phantom (see Fig. 3-2). The data was selected from the first to sixth nearest S-D pairs (188 measurements) and used for image reconstruction. Our DOT measurement results were wavelength independent since the embedded objects were made with a low concentration of diluted black ink with a flat absorption spectrum. Thus, I utilized the data taken only from 830 nm for image reconstruction.

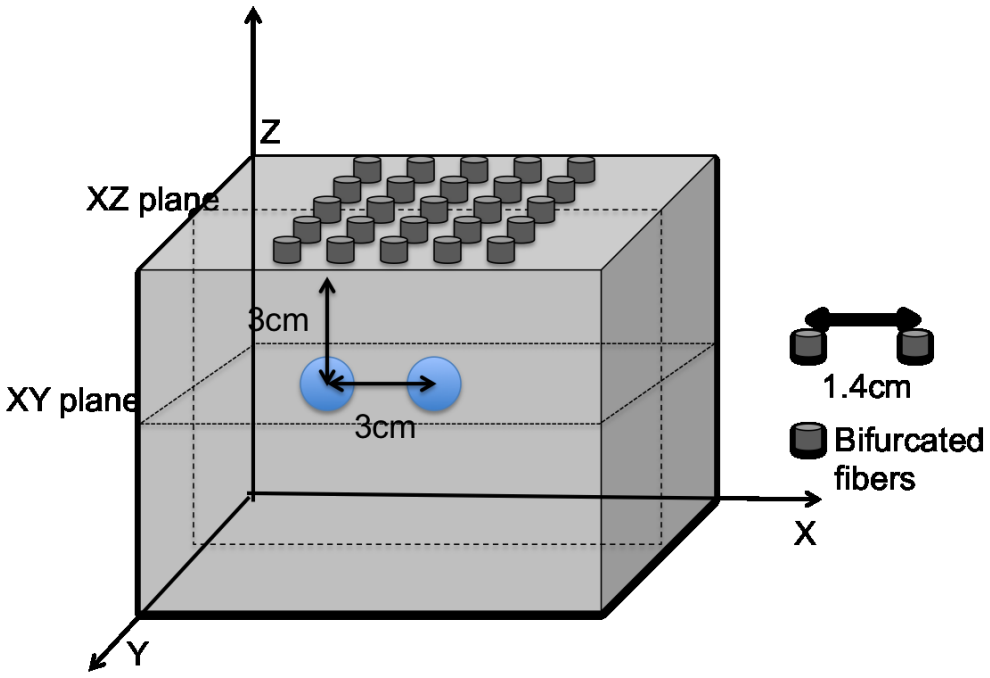

Figure 3-2: Experimental setup showing the locations of absorbers, bifurcated source-detector configuration and slices used for image reconstruction.

A liquid tissue-mimicking phantom was prepared by filling a container of dimensions of 15x10x10 cm^3 with 1% Intralipid solution. This solution served as the homogeneous background medium with an absorption coefficient (μ_a) of 0.08 cm^{-1} and reduced scattering coefficient (μ_s') of 8.8 cm^{-1}. Two spherical absorbers (μ_a = 0.3 cm^{-1}) of 1-cm diameter were placed at 3-cm depth around the center of optode array from the surface of container and separated by 3 cm, as shown in Fig. 3-2(a).

Volumetric image reconstruction was performed with the dimensions of x = -4 cm to 4 cm, y = -4 cm to 4 cm, and z = 0 to -5 cm. The voxel size of the reconstructed images was set to be 0.1x0.1x0.1 cm^3. After reconstruction, the resultant images were sliced along both lateral cross section and depth cross section separately to show the locations of the absorbers. The dotted lines in Fig. 3.2(a) outline the slices of both lateral (XY plane at Z=-3) and vertical cross section (XZ plane). All reconstructed images were normalized between 0 and 1 for comparison.

3.3.2 Camera-Based DOT Imager

Using a fiber-based DOT system has several advantages, such as being compatible with different geometry and shape of a measured organ as well as having low noise because of direct contact of fibers on the tissue surface. However, a limited surface area on small animals is often a constraint to place many fiber optodes, and thus restricts the spatial resolution of reconstructed images. In recent years, CCD cameras have been commonly used as multichannel detectors since they can serve as a detector array with possible thousands of virtual detectors and cover a wide field of view (FOV). Moreover, a CCD-camera-based DOT system is simpler and more portable with lower cost, as compared to a fiber-based, multichannel, DOT system.

Our CCD-camera-based DOT system consisted of an optical multiplexor (Avantes Inc. Multiplexor Channels 1x16) to deliver light at multiple locations and a 12-bit CCD camera (SamBa Q34 with Navitar Zoom 7000 lens) to serve as the detector. The field-of-view (FOV) of the camera was set to be 13×11 mm2. A broadband white light source (Illumination Technologies, Inc. Model 3900, quartz-tungsten halogen lamp) was connected to the multiplexor. Eight source fibers coming out from the multiplexor were arranged on the phantom surface (as shown in Fig. 3.3) to deliver the optical signals; the CCD camera placed above the phantom surface captured the diffuse reflectance signals. The total FOV was divided into 143 (13 columns ×11 rows) virtual detectors, while each virtual detector had 38×38 pixels. Total 8 (sources) x143 (virtual detectors) measurements were grouped and used to perform DOT image reconstructions.

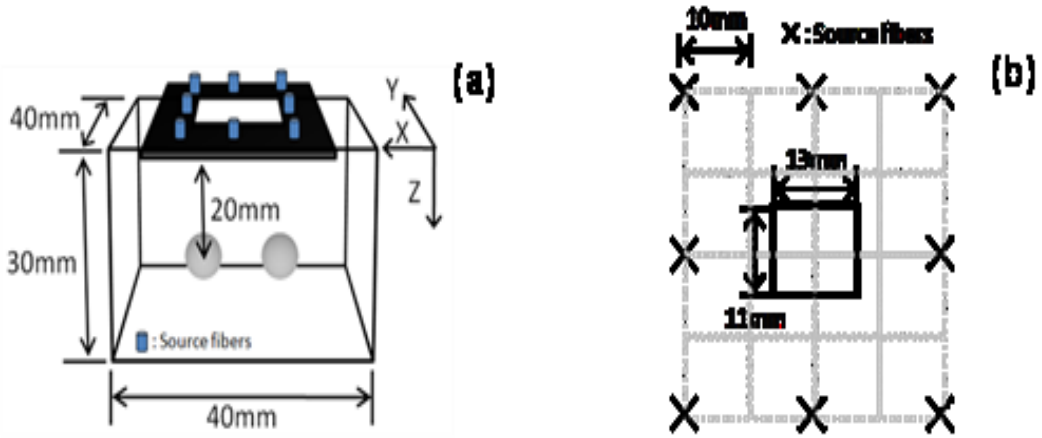

Figure 3-3: (a) Experimental setup; (b) light sources and CCD-camera configuration used.

Similar to the fiber-based DOT experiment, an intralipid solution was used to create the liquid tissue phantom with background optical properties of μ_a =0.1 cm^{-1} and μ_s' =10 cm^{-1}. Two spherical absorbers of 8-mm in diameter were embedded at a depth of

2 cm below the liquid surface and separated by 2.5 cm; the two absorbers had a 3:1 contrast ratio in absorption between the absorbers and background.

The volumetric images were reconstructed with dimension of x = -2 to 2 cm, y = -2 to 2 cm, and z = 0 to -3 cm. The voxel size of the reconstructed images was 0.1x0.1x0.1 cm^3, being the same as that in the fiber-based imaging case. Then, I sliced reconstructed images along lateral cross section (XY-plane at Z=-2mm) and depth cross section (XZ plane) to show the locations of the reconstructed absorbers. Reconstructed images were normalized between 0 and 1 for comparison.

3.3.3 Measurement Metrics

The reconstruction performances using both L1 and L2 regularizations were quantified by two measurement metrics: (1) VR and (2) CNR. Specifically, VR is the ratio of the reconstructed volume of absorber to the true volume of absorber. The volume of the reconstructed absorber was defined as the total volume of the voxels whose reconstructed μ_a values are above 50% of the maximum μ_a in the reconstructed image.

CNR indicates whether the reconstructed object can be clearly distinguished from the background. To calculate CNR, two regions, which are the volume of interest (VOI) and volume of background (VOB), were derived from the reconstructed image. VOI was defined by the location and size of the actual reconstructed object. VOB was defined by the remaining volume of the image. The CNR can be calculated by:

$$CNR = \frac{\mu_{VOI} - \mu_{VOB}}{\left[w_{VOI}\sigma_{VOI}^2 + w_{VOB}\sigma_{VOB}^2 \right]^{1/2}} \qquad 3.8$$

where wVOI and wVOB are the weight factor of the VOI and VOB relative to the entire volume (i.e., VOI or VOB divided by the entire volume), μVOI and μVOB are the mean values of μa in the object and background volumes in a 3D reconstructed image,

and σVOI and σVOB are the standard deviations of the two regions. In general, a high-quality reconstructed image possesses a VR value close to 1 and a high CNR value.

3.4 Results

3.4.1 Results from Tissue Phantom experiments

The reconstructed DOT images from the fiber-based measurement are shown in Fig. 3-5. Figures 3-5 (a) and 3-5 (b) show the results using DCA-L1, along the vertical cross section (XZ plane at Y=0) and lateral cross section (XY plane at Z=-3 cm), respectively. Figures 3-5 (c) and 3-5 (d) show the results using DCA-L2, along the same vertical (XZ plane at Y=0) and lateral cross section (XY plane at Z=-3 cm), respectively. Figures 3-5 (a) and 3-5 (b) clearly reveal that L1-regularization makes the reconstructed absorbers well matched with the real absorbers in size and location. On the other hand, Figs. 3-5 (c) and 3-5 (d) clearly depict that the reconstructed images with L2-regularization are more blurry and diffused, as compared with the images obtained using DCA-L1. These two figures also exhibit that the size of the reconstructed absorbers are larger than their expected sizes (1cm diameter).

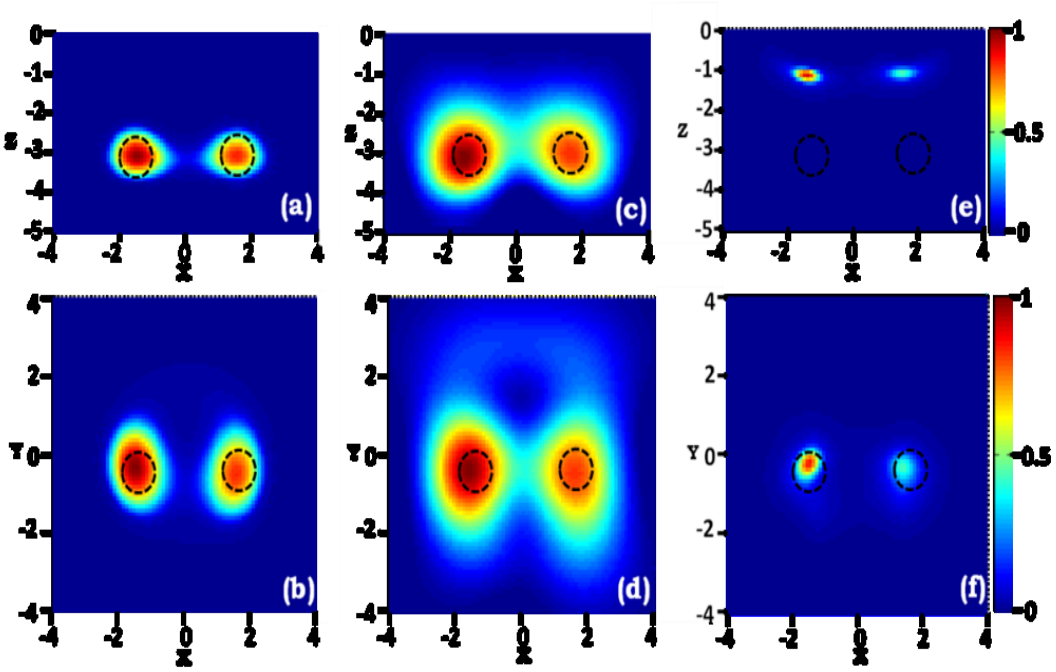

Figure 3-4 Reconstructed images of two objects placed symmetrically around the center of X-Y plane and at Z= -3 cm (See Fig. 1 for geometry details). (a) and (b) were obtained with DCA-L1 and plotted in X-Z and X-Y plane, respectively; (c) and (d) were obtained with DCA-L2 and also plotted in X-Z and X-Y plane, respectively; (e) and (f) were obtained with L1 only and also plotted in X-Z and X-Y plane, respectively. The dashed circles in each panel indicate the true size and location of the absorbers to be reconstructed. The reconstructed images are normalized between 0 and 1.

For comparison, we also reconstructed volumetric DOT images using L1 regularization without DCA, as shown in Figs. 3-5(e) and 3-5(f). These two figures noticeably illustrate that L1 regularization alone does not compensate the severe attenuation of measurement sensitivity with increased depth while it does greatly reduce blurry effects on the lateral plane (i.e., XY plane) of the image. This set of results are

expected since L1-regularization promotes sparsity enhanced image reconstruction, but does not specifically regularize or counterbalance the noise level along depth.

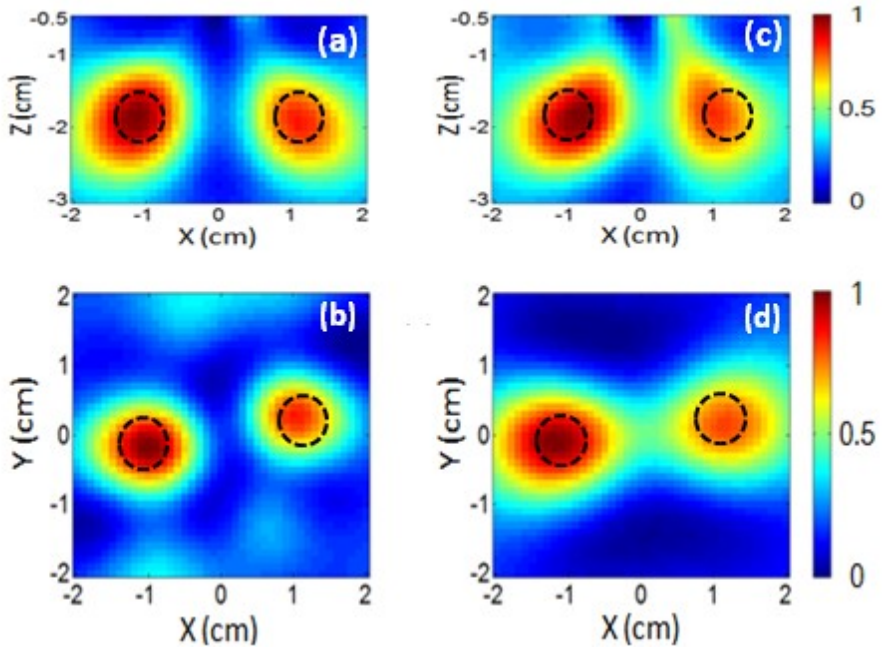

Figure 3-5: Reconstructed images of two objects placed symmetrically around the center of X-Y plane and at Z= -2 cm (see Fig. 2 for the measurement geometry setup). (a) and (b) were obtained with DCA-L1 regularization, in X-Z and X-Y plane, respectively; (c) and (d) were obtained with DCA-L2 regularization and also plotted in X-Z and X-Y plane, respectively. The dashed circles in each panel indicate the true size and location of the absorbers to be reconstructed. The reconstructed images are normalized between 0 and 1.

The data collected by the CCD-camera-based imager was also analyzed to form DOT images, as shown in Fig. 3-6. Figures 3-6(a) and 3-6(b) were obtained using DCA-L2, while Figs. 3-6(c) and 3-6(d) were reconstructed with DCA-L1. It is clearly seen that the two reconstructed absorbers in Figs. 3-6(a) and 3-6(b) are completely separate, while the reconstructed absorbers by L2 regularization [Figs. 3-6(c) and 3-6(d)] are more blurry

and diffused. Moreover, the vertical cross-section plot in Fig. 3-6(c) illustrates that the two reconstructed objects generated by L2 regularization are more distorted in their shape and also pulled toward the center. This can be explained by the fact that the number of overlapping sets of measurements is relatively higher at the center than at periphery regions. Namely, the measurement sensitivities at the center are relatively higher. However, Fig. 3-6(a) depicts better shapes and locations of the reconstructed absorbers with respect to the true objects (dashed circles in the figure). Note that the artifacts seen in Fig. 3-6(c) near the superficial layers (from -0.5 cm to -1 cm) are significantly reduced in Fig. 3-6((a).

In addition, Table 1 lists VRs and CNRs between the two reconstructed absorbers with respect to the actual ones. Those ratios were calculated for both DCA-L1 and DCA-L2 methods and for each of the fiber-based and camera-based DOT imaging systems. In case of the fiber-based imager, it is clearly seen that the VRs of the two absorbers resulting from DCA-L2 are very high, 8-12 times bigger than “1”, indicating that the reconstructed absorbers are 8-10 times larger in their volume than the actual absorbers. On the contrary, DCA-L1 gives rise to the VRs of both absorbers to be close to 1 (i.e., 0.86 and 1.25). Moreover, DCA-L1 leads to a CNR to be 2-3 times better than DCA-L2. In case of camera-based DOT measurement, DCA-L1 still provides 2 times better in VRs and CNRs, as compared to DCA-L2 regularization.

Table 3-1: comparison of DCA-L1 versus DCA-L2 algorithm

	L1-regulariztion		**L2-regulariztion**	
	Fiber-based	*camera-based*	*Fiber-based*	*camera-based*
VR(absorber1, absorber2)	(1.25, 0.86)	(3.68, 1.63)	(12.03, 8.5)	(7.14, 5.71)
CNR	14.45	10.86	5.99	5.74

Overall, the results taken from tissue phantom studies with both fiber-based and camera-based DOT systems confirm that DCA-L1 surely outperforms DCA-L2, improving greatly the spatial resolution and depth localization in volumetric DOT. Next, we wish to demonstrate the usefulness of DCA-L1 using actual human brain measurement data, as an example.

3.5 Applications of DCA-L1 Method for Human Brain in-vivo Measurements

The phantom study provided us with an accurate and quantitative means to compare the performance between DCA-L1 and DCA-L2 and to validate that DCA-L1 outperforms DCA-L2. Then, I wished to demonstrate improved quality of DOT images by DCA-L1 using actual functional brain imaging data taken from human in vivo measurements, as an example. Specifically, I chose to image the motor cortex with our DOT while having the human subject perform a motor task (i.e., finger-tapping task) as a brain stimulation protocol. The reason to choose the motor task for assessing DOT was that this protocol has been studied intensively with either single-channel or multichannel near infrared spectroscopy (NIRS) by many research groups over the last decade. According to ref. [46], there were more than 180 papers published in this area. Thus, temporal and spatial patterns of DOT images in response to finger tapping tasks are well known and adequately published. Such knowledge could help us determine and verify whether our reconstructed DOT images were accurate with improved spatial resolution.

In the actual human measurements, I followed the protocol which was previously reported in [47] for the human brain measurements. Briefly, the subject was instructed to simultaneously tap four fingers (except thumb) up and down without moving the wrist and arm. For reliability, the subject watched a video clip of finger tapping at a frequency of ~1.5 Hz while being asked to follow the same rhythm. Specifically, an epoch

of 15 seconds of tapping and 25 seconds of rest was repeated 10 times in each session. A 30-second, pre-session baseline and a 20-second, post-session baseline were also recorded. Before a formal session, the subject was instructed to perform a practice session. The experimental protocol has been approved by the Institution Review board of the University of Texas at Arlington and the University of Texas Southwestern Medical Center at Dallas.

For data acquisition from the sensorimotor cortex, a multichannel, continuous-wave NIRS system (CW-5, Techen Inc., Milford, MA) [48] was used. As shown in Fig. 3, eight sources and sixteen detectors were used for a bilateral imaging scan. The sources were designed to emit light at 690 nm and at 830 nm, since two wavelengths were required to calculate changes in concentrations of oxy- and deoxy- hemoglobin (ΔHbO and ΔHbR) [49,50]. The source and detector optodes were arranged in such a way that they covered an area of ~8×5.2 cm2 on each lateral side of the subject's head and provided a total of 28 nearest S-D channels at a nearest S-D distance of 3.0 cm, as marked in Fig. 3(b). It has been reported that a high-density probe array used in DOT would greatly improve DOT spatial resolution [51]. In the meantime, our recent study using laboratory phantom measurements has revealed that the quality of reconstructed DOT images depends on the measurement density asymptotically, having an optimal point for measurement density beyond which more overlapping measurements would not significantly improve the quality of reconstructed images [42]. Based on the conclusion from ref. [42] , we decided to utilize the probe geometry shown in Figure 3-6 since it would provide us with a moderate spatial resolution while the setup time to place the probe array on the subject's head with good optical contacts was reasonable (about 10-15 minutes).

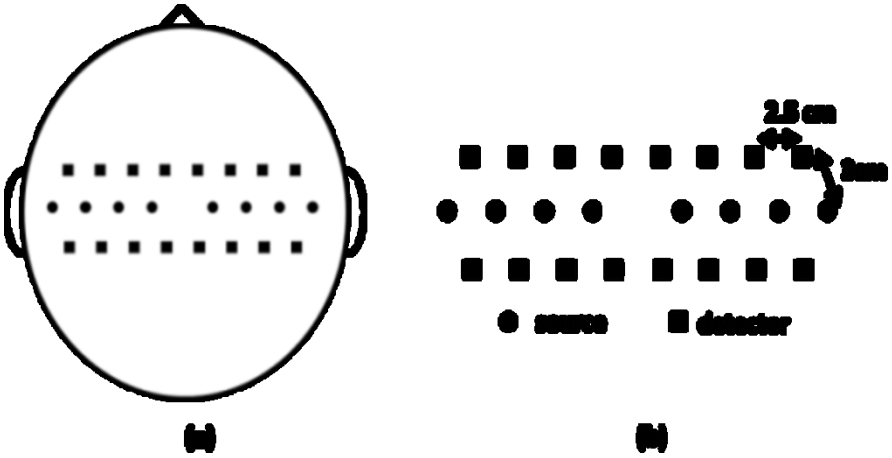

Figure 3-6 (a) placement of optodes on the subject's head; (b) S-D (Source-detector) configuration showing optode separations.

The actual data acquisition rate was at 100 Hz, which was later down-sampled to 10 Hz for data processing and image reconstruction. The data was high-pass and low-pass filtered at 0.01 Hz and 0.3 Hz, respectively, to remove the baseline drift and interference due to arterial pulsations. Changes in optical density were calculated as a function of time at each wavelength. Then, the data from each S-D channel was block-averaged across time. Consequently, the block-averaged time profiles were further temporally averaged within the stimulation (i.e., finger tapping) period for each S-D channel, all of which served as inputs of y_i for Eq. (5). Reconstructed hemodynamic images of motor activation were obtained after following the steps given in Section 2.2 (more specifically in Section 2.2.4). The sensitivity matrix, $\boldsymbol{A}$, was generated assuming μ_a (background) = 0.1 cm^{-1} and μ_s' (background) = 10 cm^{-1} for both wavelengths. In the process of DOT image reconstruction, volumetric imaging space of 20.32 (5.84×4 cm^3 was created with a voxel size of 0.2x0.2x0.1 mm^3. The constructed images were sliced at

2.5-cm depth along the lateral cross section (i.e., in XY plane at Z=-2.5 cm) in order to compare the performance of L1 and L2 regularizations.

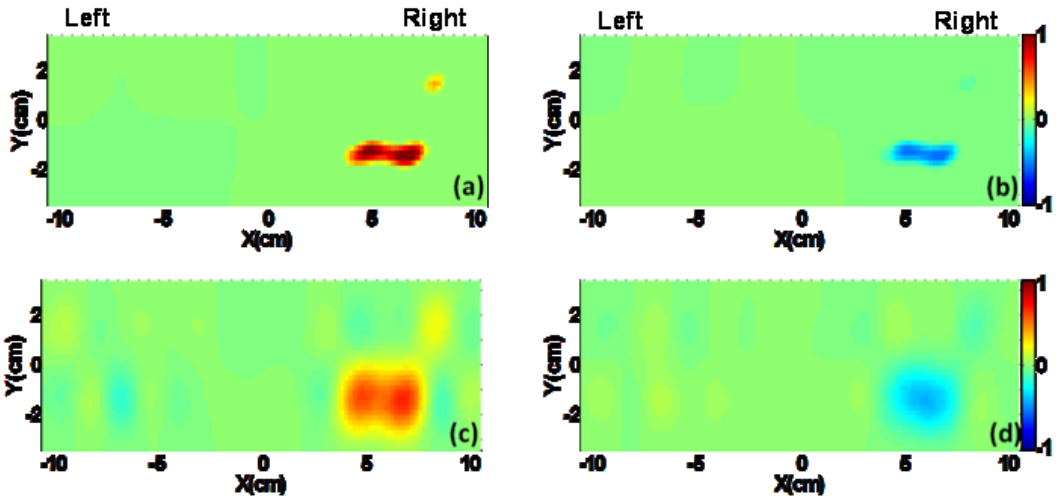

Figure 3-7: 2D slices (2.5 cm below the scalp surface) of reconstructed human brain images induced by finger tapping tasks. It shows a localized area with (a) an increase in oxy-hemoglobin concentration and (b) a decrease in deoxy-hemoglobin concentration when DCA-L1 is applied. In contrast, a larger or more diffused region is observed with (c) an increase in oxy-hemoglobin and (d) a decrease in deoxy-hemoglobin concentration when DCA-L2 is utilized for image reconstruction.

The original study was reported in ref.[35] having a total number of 8 human control subjects measured. The corresponding data across all controls were analyzed to conclude the study. A data set was randomly selected as a representative from the 8 human subjects data which was the part of original study [47] and performed 2D DOT images using both DCA-L1 and DCA-L2, as follows.

As expected, the subject had brain activation on the right side of the brain due to the left hand finger tapping (contra-lateral activation). Four panels in Fig. 3-7 show 2D

slices from the reconstructed volumetric images at 2.5 cm depth from the scalp surface (i.e., XY plane at Z=-2.5 cm). The images were normalized between -1 and 1 for comparison. Figures 3-7(a) and 3-7(b) present the reconstructed ΔHbO and ΔHbR images obtained using L1 regularization; Figs. 3-7(c) and 3-7(d) show the reconstructed ΔHbO and ΔHbR images obtained using L2 regularization. In comparison, Figs. 3-7(a) and 3-7(b) show much sharper and more localized reconstructed images with L1 regularization, as compared to the blurred L2-dervied images in Figs. 3-7(c) and 3-7(d). These figures clearly demonstrate that L1 regularization can be valuably applied to functional human brain studies, and can greatly improve the spatial resolution of *in vivo* human brain images.

3.6 Application to Prostate Imaging

From the previous sections, it is evident that DCA-L1 is promising technique to improve the resolution of DOT images. It should be noted that DCA-L1 algorithm has be designed to improve the image reconstruction in the context of dynamic DOT or perturbation DOT. While applying L1-DCA towards PCa imaging two specific questions needs to be answered. (1) How to create perturbation in PCa. (2) PCa imaging should be performed via rectum and the space is limited to incorporate large number of sources and detectors. The geometries utilized in the previous sections (5X5 sources and detectors) are targeted towards brain imaging. Will L1-DCA work for sparse source detector geometries? First question is still exploratory in PCa imaging and has been successfully applied towards breast cancer and arthritis. In breast cancer, a perturbation has been created via gas challenge [C.M. Carpenter 2010]. When subjects are breathe oxygen, air and carbogen the response of the tumor is different between the gases and it creates contrast for imaging. To answer second question I also performed six simulations with

prostate geometry (8X2 sources and detectors). A simulated absorber is placed in six locations as shown in figure 3.8. The optical properties of the absorber are set to 0.01 cm-1 for the background and 0.02 cm-1 for the absorber. The metrics form previous sections i.e. VR and Z error (difference between reconstructed Z(depth) location and target Z location) are utilized to measure the quality of reconstructed images. The results are tabulated as shown in table below.

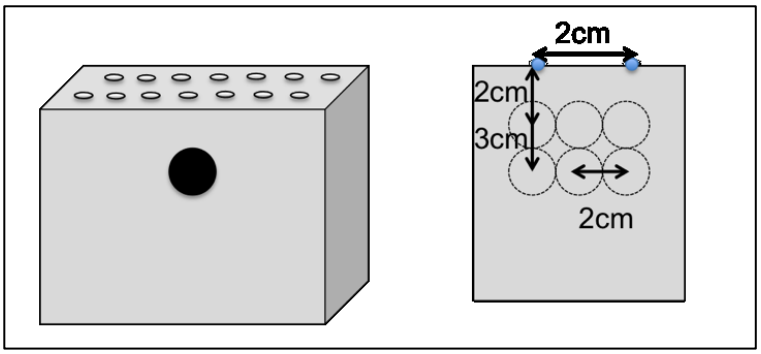

Figure 3-8 (a) Simulation setup and probe geometry utilized to check the feasibility of L1-DCA in PCa imaging. (b) Dotted circles indicate the six locations of absorber used for testing.

Table 3-2: Volume ratios and position error at six simulated locations

	Volume ratio (VR)		**Position error**	
Location	2cm depth	3cm depth	2cm depth	3cm depth
Right	0.69	1.23	2mm	3mm
Left	0.7	1.2	2mm	3mm
Center	0.883	0.9961	2mm	2mm

From the table, the range of volume ratio (VR) across six simulations performed is 0.69-0.991. While volume ratio is slightly off when the absorber is on the side, overall volume ratio is close to 1. Z error is approximately 2mm in most of the simulations that is common in DOT reconstruction. From the simulations we can say that L1-DCA can be applied for PCa imaging when provided a way to create perturbation.

3.7 Discussion

In this study, I combined two previously published techniques, (1) DCA and (2) L1-regularization, for enhancing or improving the quality of reconstructed DOT images. Investigations on these two methods have been individually reported [35,36]: the DCA method compensates the loss of measurement sensitivity in depth and has been used with L2 regularization for volumetric DOT imaging. Such a combination, however, still cannot greatly improve the diffuse nature of DOT with over-smoothed image edges [see Figs. 3.5(c) and 3.5(d)]. On the other hand, L1 regularization has the ability to provide sharper reconstructed images and to reduce the blurry effect on the images. However, L1 regularization alone doesn't compensate for the severe attenuation of measurement sensitivity with increased depth, as demonstrated in Figs. 3.5(e) and 3.5(f).

The key idea of this study is to make good use of both DCA and L1-regularization jointly to yield high-quality reconstructed images with improved depth localization and spatial resolution. I tested and validated the combined approach using laboratory tissue phantoms, with two typical scenarios of DOT, namely, a fiber-based and camera-based imaging system. The phantom studies yielded conclusive results based on two measurement metrics of VR and CNR. The VRs from both imaging systems indicate clearly that DCA-L1 algorithm outperforms DCA-L2 algorithm, at least 2-3 times better for

volumetric DOT imaging. Furthermore, CNR from L1 regularization is 2 times larger than that from L2 regularization.

Throughout the study, I have also observed that the reconstructed images with the fiber-based DOT system appear to be less noisy and more accurate than the images obtained with the camera-based system. This can be mainly attributed to the bifurcated optode geometry used in the fiber-based system. If non-bifurcated fibers were used, both imaging systems would generate similar quality of DOT images regardless of the locations of absorbers [28, 38]. Furthermore, as shown in Figs. 1 and 2, the two absorbers were placed symmetrically on both sides of the volumetric space (not in the center) [43].

The usefulness of the DCA-L1 approach has been also examined using actual functional brain imaging data taken from human *in vivo* measurements. With DCA-L1, the reconstructed human brain images from a randomly selected human subject show significant improvement in depth localization and spatial resolution of the imaged activation region/volume in the brain. Specifically, reconstructed ΔHbO and ΔHbR changes derived from DCA-L1 are more localized and concentrated in the specific or expected region (see Figs. 3.6(a) and 3.6(b)), as compared to those resulting from DCA-L2 method. In contrast, the blurry effect of L2 regularization is clearly seen in reconstructed images [see Figs. 3.6(c) and 3.6(d)].

It is well accepted by the biomedical optics community that functional brain images derived from multi-channel NIRS or DOT suffer from low-spatial resolution, as compared to fMRI, due to the scattering nature of light when it interacts with tissue. Without setting up a high cut-off threshold in ΔHbO or ΔHbR amplitude, the cortical activation regions imaged by DOT are usually bigger and less localized than those given by fMRI [52]unless a high-density DOT is utilized. In the latter case, the reconstructed

DOT images may have comparable spatial resolutions with respect to fMRI. According to ref., the motor cortex often exhibits prompt hemodynamic responses (i.e., ΔHbO) in the hemisphere contralateral to the performing limb. Consistently, we did observe contralateral activation in this study, which was approximately located near the motor cortical strip. While we did not have a quantitative measure to determine the width of motor strip in the current study, we estimated that the size of motor activation should be smaller than 2-3 cm across the motor strip (i.e., along the x-axis). This estimation was based on a recent, similar study that was performed over several human subjects using the same DOT system as used in this study, but with a high-density probe array [53]. The data in ref. [53] allowed us to deduce that the activation size near the motor cortex evoked by a simple finger-tapping task was about ~2x2 cm. The reconstructed images in Fig. 6 clearly illustrate that DCA-L1 leads to the reconstructed brain activation size more localized and accurate than DCA-L2, with respect to the expected activation region. Note that in this human brain study, the optimized empirical parameters (i.e., $NIPCa_G$ and NS_{Newton}) were derived from our phantom results. For quantitative or rigorous validation of DCA-L1, in future a joint fMRI-DOT study in order to make volumetric DOT possible for human brain imaging.

3.8 Conclusion

In conclusion, based on tissue-phantom studies, we have validated that the combination of DCA with L1-regularization can offer significant improvement in depth localization and spatial resolution for DOT images. We have further demonstrated the applicability and usefulness of this method using in vivo measurements of functional human brain imaging. In general, this DCA-L1 approach can be extended to other applications of DOT, such as breast and PCa detection, and can be further explored to

improve quantification of tumor optical properties because of more localized targets identified.

Chapter 4

Hierarchical Clustering Method to Image Prostate Cancer Using Diffuse Optical Tomography

4.1 Introduction

In order to have trans-rectal DOT be able to provide excellent reconstructed images for PCa detection, obstacles has to be acknowledged in order to find appropriate solutions. One main obstacle is closely associated to the location of measurements: the human rectum, where we have a limited space (leading to a limited number of optodes to be implemented) and only reflectance geometry of DOT can be utilized. Given the nature of light scattering in tissues, DOT suffers from poor spatial resolution. Measurements with reflectance geometry face a harder challenge to achieve an excellent spatial resolution than those by transmission geometry. One way to improve the spatial resolution is to couple DOT with other imaging techniques, such as MRI and ultrasound. In particular, a combined TRUS and DOT probe for imaging PCa has been studied previously, utilizing the anatomical information from ultrasound to reduce the number of unknowns in the DOT image reconstruction. As shown in ref [28], each anatomical region was considered to be homogenous; uniform optical properties were reconstructed in each respective region. While the combined TRUS-DOT method improves accuracy of reconstructed DOT images, it relies highly on the ability of TRUS to locate the PCa lesion. Given the fact that TRUS has a low accuracy to detect PCa and that each region is assumed homogenous, the reconstructed DOT images of PCa could be erroneous.

In order to limit the dependency of DOT image reconstruction on TRUS sensitivity, a hybrid reconstruction technique has been developed by combining a piecewise cluster reconstruction approach with hard prior anatomy of prostate available from TRUS. The proposed method utilizes a hierarchical scheme of clustering where a

cluster can be defined as a group of nodes/voxels within a predefined volume. By utilizing hierarchical clustering, a region of interest (ROI, i.e., the prostate) can be transformed into a partially heterogeneous medium, within which we can search and further reconstruct potential cancer lesions. The inverse problem of DOT is solved in multiple steps by changing cluster sizes within the image domain. Multi-step reconstruction in DOT has been reported earlier [54] for breast cancer detection based on a frequency-domain study. It is understood according to reference [54] that the size and location of the absorber were partially or roughly estimated in the first step of reconstruction; more steps were utilized to further improve the quality of reconstructed images. In the TRUS-DOT scenario, however, a rough reconstruction in the first step is futile to effectively detect PCa due to the multi-layer tissue compositions, reflectance measurement geometry, limitation in the number of measurements, and particularly the inability of ultrasound to identify PCa lesion or lesions. Thus, to improve the effectiveness and accuracy of PCa imaging, piecewise division of the image domain in DOT has been considered, assuming that the domain consists of disjoint sub domains with different optical properties.

Specifically, in this work, the piecewise division of the image domain for a human prostate is performed in the inverse calculation. By doing so, combination of the piecewise division with hard-prior anatomic information for DOT image reconstruction is possible. Specifically, in this chapter, a detailed procedures of our proposed method and its validation is presented by showing its performance with the following computer simulations: 1) one anomaly at a depth of 1 cm to 3 cm below the measurement surface, 2) two anomalies at 1 cm and at 2 cm, respectively, 3) variable background absorption from 0.005 to 0.015 mm-1), 4) variable noise percentage from 0% to 3%.

4.2 Methods

In hierarchical clustering method (HCM), the reduction of a parameter space is realized by segmenting the medium or region of interest (ROI) into several geometric units or clusters. Each of the geometric clusters was assumed to be homogeneous and had the same optical property. In this way, the medium or image domain could be partially heterogeneous since the domain may contain several geometric clusters. During the DOT image reconstruction process, a value of μa from each cluster was updated using Eq 2.45. Since the size of each cluster was user-defined, the smallest could be a single FEM mesh node and the largest be the entire domain region, similar to that used in the regular reconstruction method without any spatial prior. Specifically, the nodes in the mesh were tagged and separated into clusters, as indicated by c1, c2…cj with respect to each cluster. The Jacobian matrix in eq. (5) was then modified to be J* and given by [30]

$$J^* = JC \tag{4.1}$$

where matrix C had the size of NN×NC (number of nodes × number of clusters). The elements of matrix C were given as follows:

$$C(i,j) = \begin{cases} 1 & if\ i \in c_j \\ 0 & else \end{cases} \tag{4.2}$$

where i marks the number of nodes and j labels the number of clusters. By the end of each iteration, the solution vector of δμa was mapped back to each node using eq.

$$\delta\mu_a = C(\delta\mu_a^*) \tag{4.3}$$

where δμa* is the vector with optical properties in respective geometric clusters solved from Eq. (4.3). The function of matrix C is to transform the initial image domain into a new image domain where the inverse procedure is performed with cluster-based

geometric structures. It is a mediator or operator that converts the regular geometry to and from cluster-based geometry for the reconstructed object. So, technically no inversion or transpose of C is directly involved.

Initially, two ROIs were considered for reconstruction, such as background and an anomaly; the background mesh was geometrically segmented in a heterogeneous fashion. For multiple ROIs, we hierarchically implemented the proposed method by segmenting the region which was more prone to cancer, while utilizing available prior information. Specifically, the proposed method is implemented in four steps, as shown in Fig. 4.1. To image PCa through trans-rectal DOT imaging, four types of tissues were examined: rectum wall, peri-prostate tissue, prostate and tumor. Each of these tissues may have their own optical properties. When being imaged without any prior anatomic information, different types of tissues are highly likely to be mixed among one another because their optical contrasts are relatively subtle and difficult to distinctly separate them. Thus, our HCM is critical for us to achieve an improved spatial resolution for prostate imaging.

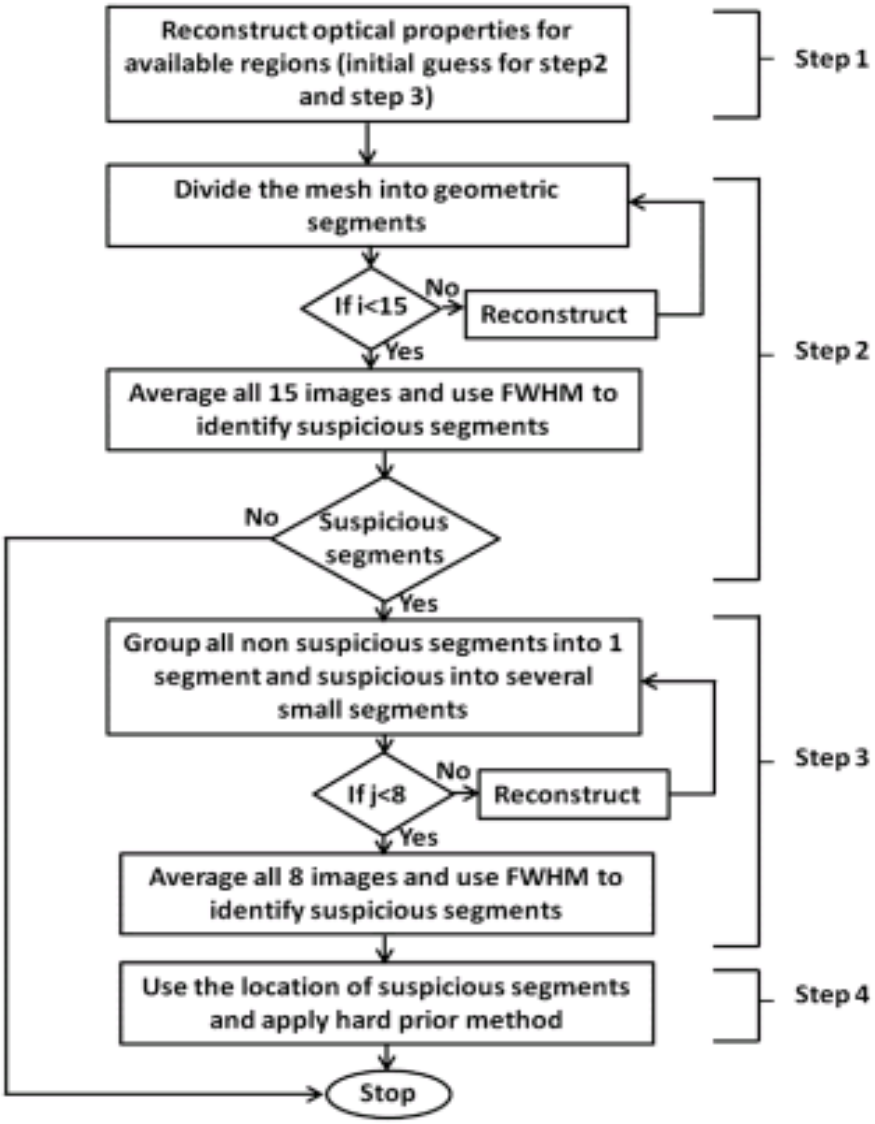

Figure 4-1: Steps or a flow chart showing HCM

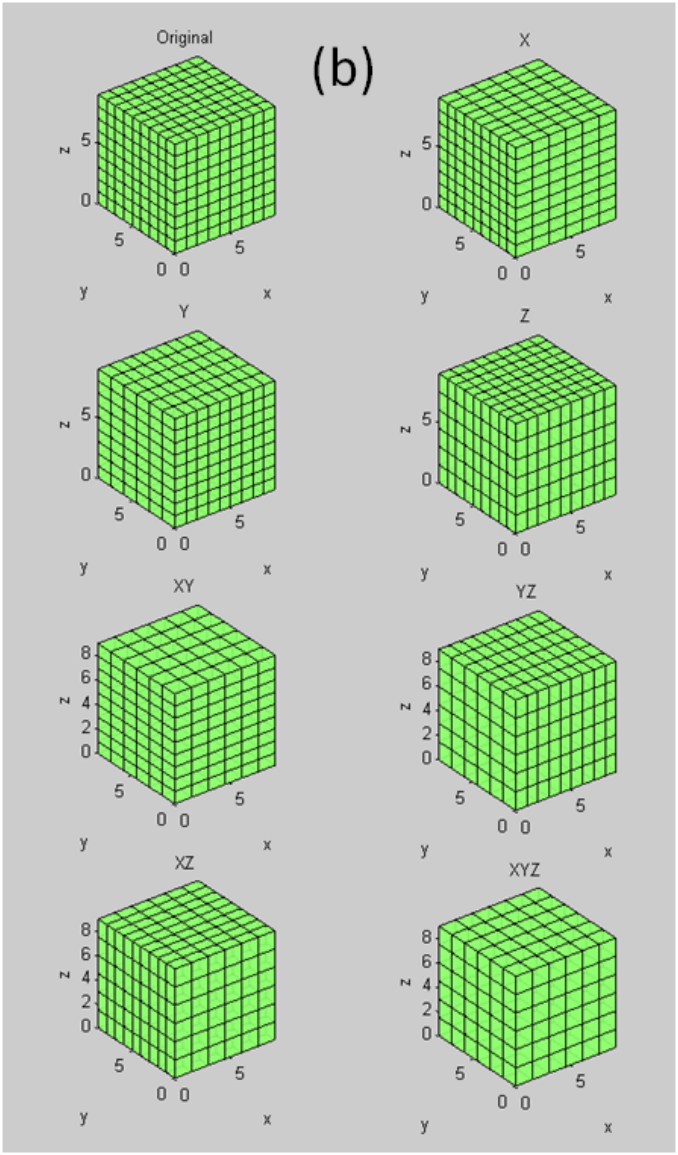

Figure 4-2 Geometrical illustration of clustering

In Step 1, reconstruction was performed based on prostate anatomic images offered by TRUS and the assumption of a homogeneous prostate. With such prior spatial information, the reconstructed μa values in both background and prostate regions (as two ROIs) should be reasonably accurate with respect to the actual values, assuming that the

sizes of prostate tumors are much smaller than the size of the prostate. Then, the reconstructed μa values in available ROIs would serve as the initial guess in Step 2 and Step 3.

Step 2 of HCM was dedicated to finding the probable locations of anomalies (i.e., prostate tumors). To achieve this, prostate region has been geometrically divided into several clusters, so the prostate tissue became a heterogeneous medium. However, without prior knowledge of suspicious locations, dividing the prostate into several clusters or elements may result in a mixing of suspicious tissue with normal prostate tissue and vice versa. In order to prevent mixing, hierarchical approach is used to cluster the prostate volume with different unit volume sizes iteratively, to minimize the mixing effect of cancer and normal tissues within a cluster.

Specifically, the initial volume of a cluster was considered to be 1x1x1 cm3 in each of the x, y and z dimensions. Then, we varied the volume of the cluster by increasing the length of the cluster in each dimension iteratively. For example, an increase in length of 0.5 cm in only x direction gave rise to a unit volume of 1.5 x 1 x 1 cm3, followed by the same length increase in only y or only z direction. In this way, 8 different unit volumes can be generated in three x, y, z directions, by increasing the linear length in only one dimension (x, y, z), or in two dimensions (xy, yz, xz), or in three dimensions (xyz) and the initial size. The procedure is given as follows: (1) reconstruct an initial μa image with a starting base unit size (i.e., 1x1x1 cm3), (2) save the reconstructed image, and go back and change the unit volume size (e.g., 1.5x1x1 cm3 or 1.5x1.5x1 cm3 or 1.5x1.5x1.5 cm3) and reconstruct the image again (Step 2 in Fig.1). To be more comprehensive, base unit volume size has been increased 1x1x1 cm3 to 1.5x1.5x1.5 cm3, for the latter of which the same length interval (0.5 cm) is applied to increase the base unit (e.g., 2x1.5x1.5 cm3, 2x2x1.5 cm3, or 2x2x2 cm3). In this way, another set of 8

reconstructed images can be generated with varied base unit volumes, resulting in an overall 15 (i=15) images (resulting from 15 combinations) by the end of Step 2. (3) all of the reconstructed μa images is averaged to obtain the final image. (4) Next, we search for suspicious clusters that have high μa values with respect to the background, as an indication of cancer. The location of suspicious clusters was selected using full width half maximum (FWHM) of the updated μa values within the prostate region. If no suspicious cluster is identified, we conclude that the prostate has a low probability of having cancer.

In Step 3, if some suspicious clusters in Step 2 are seen, we then group all the non-suspicious clusters as one new single cluster and subdivide the suspicious clusters into further smaller clusters. Now, the initial unit volume size used within the suspicious regions in Step 3 is set to be 0.5 x 0.5 x 0.5 cm3. The procedure explained in Step 2 is repeated here with a length variation of 0.25 cm in any one of three dimensions. Similar to Step 2, the final reconstructed image of Step 3 is an average of the 8 images (j=8) obtained by varying the unit volume in 8 different fashions. FWHM of the μa values is still used to localize suspicious regions for further inspection with an improved spatial resolution.

In steps 2 and 3, a region-specific regularization parameter has been utilized to favor the reconstruction in the prostate region, using a hierarchical approach. The underlying rationale of this approach was previously reported in ref. [54] that the regularization parameter controls the level of optical property updates at each iteration. A larger regularization parameter gives rise to a subtle update, while a smaller regularization parameter offers a steeper update with a broader solution range. In our case, a smaller regularization value applied to the prostate region allows us to focus only on the prostate and to accurately update the reconstructed optical properties of the prostate. Finally, in Step 4, reconstruction process has been repeated using the

suspicious regions identified in Step 3 as a hard prior or as given cancer regions, with a uniform initial guess as used in Step 1.

In principle, selections of regularization parameters and stopping criterion play a key role in any iteration-based reconstruction techniques. In HCM, regularization parameters and the stopping criteria are selected empirically. For Step 1, the regularization parameter was 10 and the stopping criterion was when the change in projection error was less than 2% of that in the previous iteration. For Step 2, the regularization parameter was 0.1 and the stopping criterion was when the change in projection error is less than 20% of the previous iteration. The reason for this criterion at Step 2 was that the value of the regularization parameter was small so that the noise began to dominate the reconstructed images. For Step 3, regularization parameter was further decreased the to 0.001 while keeping the same stopping criterion as that in Step 2.

4.3. Simulation and Experiment Results

4.3.1 Trans-rectal DOT Image Reconstruction by HCM with Limited Prior Information

To validate HCM, a simulated TRUS-DOT probe was used, having 16 co-located or bifurcated optodes that could serve as both sources and detectors [see Fig. 4.3(a)]. Computer simulations have been performed by considering a FEM mesh, which was anatomically similar to a TRUS image of a human prostate [see Fig. 4.3(b)]. It consisted of four ROIs, such as prostate (sky blue region), peri-prostate tissue (blue region), rectum wall (green) and prostatic tumor (anomaly) [see Fig. 4.3(c)]. The mesh used in this study was an unstructured tetrahedral mesh with 28,174 nodes and 156,191 elements. The thickness of the rectum wall was set to be 5 mm and a curvature radius of 50 mm. The following optical property (i.e., absorption coefficient) distributions were used: 0.01 mm-1

for rectum wall, 0.002 mm-1 for surrounding tissue, 0.006 mm-1 for prostate, and 0.02 mm-1 for anomaly [28]. An anomaly has been created at 1-cm depth from the rectum wall to test HCM. The CW mode was utilized in the simulations; 1% random noise was added to the data to mimic the instrument noise.

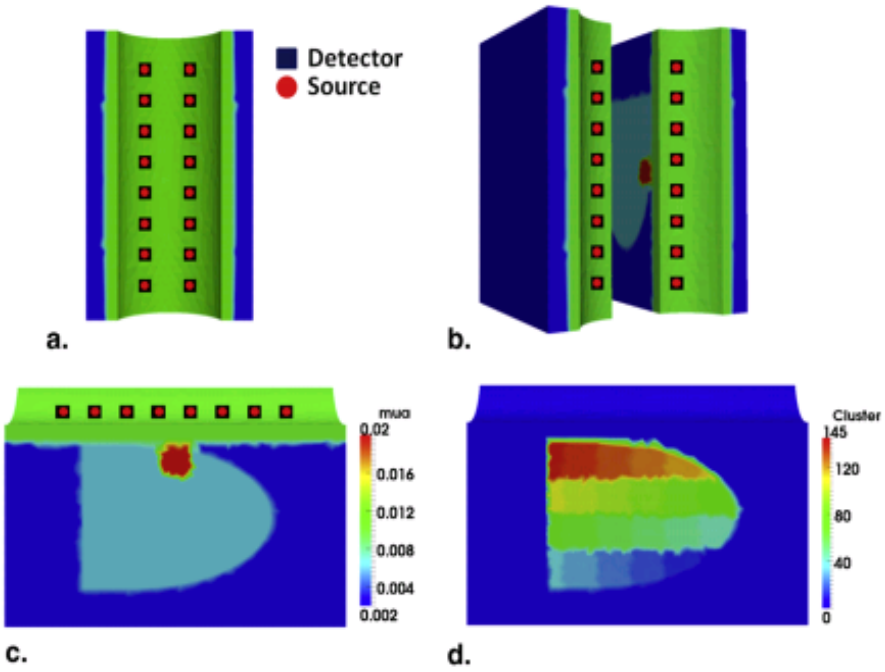

Figure 4-3: (a) Probe geometry used in this study; each optode is bifurcated to serve as a source and detector. (b) Mesh (elements not highlighted) has been rotated and sliced vertically into two halves to show the simulation geometry. (c) A slice from the mesh cut along the longitudinal direction, showing simulated rectum wall (green), surrounding tissue (blue), prostate (sky blue).An anomaly has been created at 1-cm depth from the rectum wall. (d) Image reconstruction in progress, showing clusters within the prostate region.

Simulated DOT data was computed using the diffusion forward model with FEM; NIRFAST [22] was used to perform the forward calculation. The procedure explained in chapter 2 and section 2 of current chapter was used to reconstruct images from all

simulated data. Specifically, Step-1 reconstruction was done using an initial guess of μa=0.01 mm-1 to recover the optical property of the rectum wall, prostate, and surrounding tissue. Then the reconstructed data from Step 1 served as the initial guess for Steps 2 and 3. Next, the prostate region was divided into several clusters [see figure 2(d)], which had tissue volumes of 1.00 to 8 cm3. As noted earlier, the final image obtained after Step 2 was an average over 16 independent reconstructions. In Step 3, the suspicious region identified (using FWHM) in Step 2 was further divided into smaller clusters (0.125 – 0.42 cm3 in volume). The final image of Step 3 was an average over 8 image reconstructions. FWHM was again used to find the suspicious regions, which were treated as individual regions and entered as the hard prior conditions for finer reconstruction in Step 4.

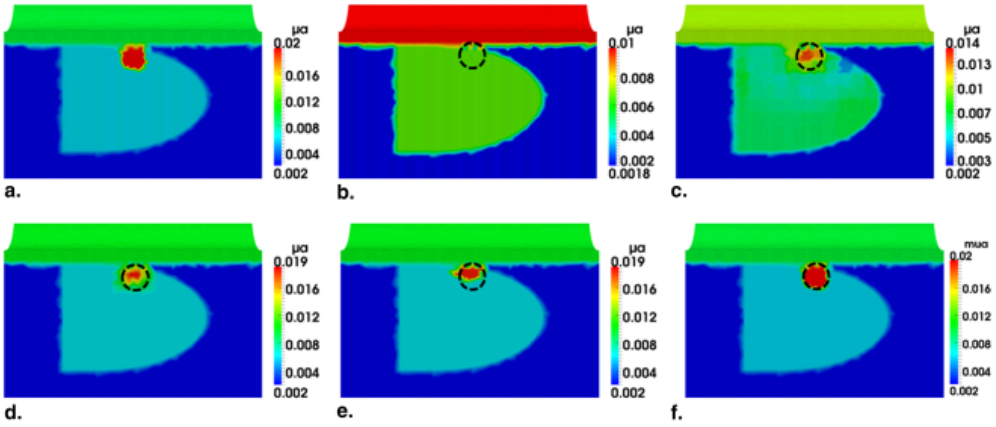

Figure 4-4: reconstructed μa values in mm-1 using different reconstruction steps for (a) an anomaly located within a simulated prostate. The dotted circles indicate the real locations of the anomaly. Reconstructed images (b) after Step 1 of HCM, (c) after Step 2 of HCM, (d) after Step 3 of HCM, (e) after Step 4 of HCM. (f) Reconstructed image for the same case using a known hard prior for the inclusion.

Panels in Fig.4.4 provide overall steps involved in HCM to perform DOT image reconstructions. As shown in Fig. 4.4 (a), an anomaly was embedded at 1-cm depth from the surface of the rectum. Figure 4.4 (b) demonstrates the result after Step 1, showing that the reconstructed image is biased with the known priori information of the prostate, peri-prostate tissue and rectum wall. As seen in Fig. 4.4 (c), Step 2 of HCM is able to determine a probable location of the anomaly inside the prostate, without prior anatomical information. Figures 4.4 (d) and 4.4 (e) shows the results from Steps 3 and 4 of HCM and clearly depict the location of the simulated tumor. After Step 3, while the optical properties in the anomaly region are not completely uniform, absorber can be located accurately inside the prostate. Finally by Step 4, the reconstructed μa value of the anomaly has been improved. For comparison, Fig. 4.4 (f) illustrates a recovered μa image using the given spatial prior information on the anomaly location. Moreover, Table 1 shows that HCM resulted in a recovery rate of 95% for the embedded target, without using any spatial prior information.

Table 4-1 Comparison of reconstructed μa values by HCM with and without prior anatomical information

Tissue type	**μ_a (mm^{-1})**	
	without prior information (%)	with prior information (%)
Peri-prostate	0.002 (100)	0.002 (100)
Rectum wall	0.01 (100)	0.01 (100)
Prostate	0.006 (100)	0.006 (100)
Anomaly	0.019 (95)	0.02 (100)

4.3.2 Investigation of HCM on Depth Sensitivity

In order to test depth sensitivity of HCM, an anomaly was created at depths of 1 cm, 2 cm and 3 cm from the surface of the rectum wall. Reconstructed images from all three locations were compared as shown in Fig. 4.5. The doted circles in Fig. 4.5 indicate the actual location of the targeted anomaly. Figures 4.5(a) and 4.5(b) are the reconstructed images after Step 4 using HCM with anomaly placed at 1-cm and 2-cm depths, respectively; Figure 4.5(c) is the reconstructed image after Step 2 using HCM with anamoly placed at 3-cm depth. The algorithm was stopped after Step 2 in this case because of its inability to find any absorbers. Figure 4.5(c) demonstrates that HCM is incapable of recovering the anomaly at a 3-cm depth because of the severe decrease in measurement sensitivity with increasing depth, the number of optodes used, and the absorption coefficient of the prostate.

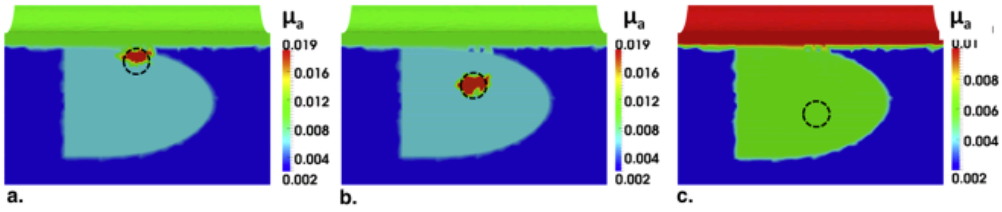

Figure 4-5: (a) shows the two anomalies separated by 2 cm and created at a depth of 2 cm; (b) shows the two anomalies separated by 4 cm and located at depths of 1 cm and 2 cm. Dotted circles show the actual locations of the anomalies.

For quantitative comparison, Table 2 lists the actual and recovered optical property and their recovery percentage rate for the reconstructed absorber at the three respective depths. This simulation-based summary table implies that HCM has the ability to reconstruct an absorbing-anomaly within a human prostate at a depth of 2 cm with a possible recovery rate of 95%, if 2x8 bifurcated optodes are used. Whether the detection

sensitivity may go deeper than 2 cm in practice remains to be seen since it also depends highly on the number of optodes, the power of light sources, and the type of detectors used for the measurement.

Table 4-2 comparison of reconstructed μ_a value of the target at different depths using HCM

Depth	Target (mm^{-1})	Reconstructed (mm^{-1})	% recovered of μ_a
1cm	0.02	0.019	95
2cm	0.02	0.019	95
3cm	0.02	---	---

4.3.3 Trans-rectal DOT Image Reconstruction by HCM with Two Absorbers

The capability of differentiating two absorbers by HCM is important in PCa imaging because of the existence of multifocal cancer regions. Moreover, the results from Section 3.2 indicate that HCM is not able to detect an anomaly at a depth of 3 cm. So within the depth limit, I investigated whether HCM is able to reconstruct two absorbers in this sub-section. For this purpose, simulations has been performed with cases. In Case 1, two anomalies of 1-cm diameter were created at the depth of 2 cm from the surface.

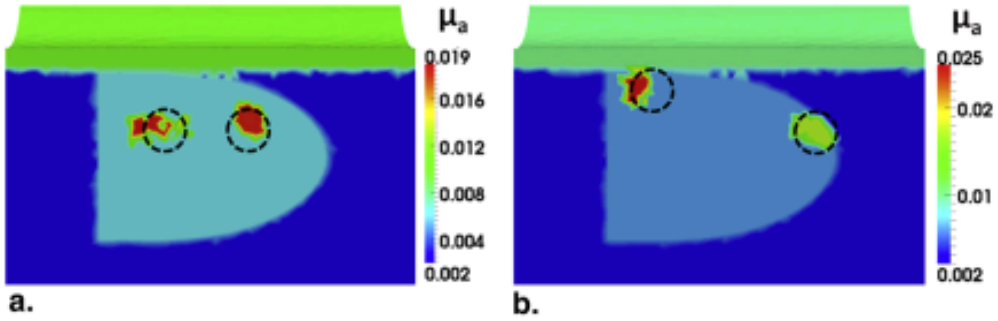

Figure 4-6: (a) shows the two anomalies separated by 2 cm and created at a depth of 2 cm; (b) shows the two anomalies separated by 4 cm and located at depths of 1 cm and 2 cm. Dotted circles show the actual locations of the anomalies.

The two anomalies were separated by 2 cm, as shown by dotted circles in Fig. 4-6(a). This test was useful in understanding the minimum separation between two absorbers that is required to recover them as two separable absorbers in reconstructed images. This test also allowed us to estimate the recovery of off-centered absorbers. This estimation is important because the sensitivity of DOT is often higher in the center of the image domain due to the number of overlapping measurements. In Case 2, the absorbers were created at the depths of 1 cm and 2 cm, respectively, as drawn by dotted circles in Fig. 4-6(b). The separation between the two absorbers was increased to 4 cm. Figures 4-6(a) and 4-6(b) also show the reconstructed images after Step 4 using HCM, demonstrating that the locations of the anomalies were successfully recovered.

4.3.4 Investigation of HCM on Effects of Different Background (Prostate Region) Contrast

Further investigation of HCM on variation of background absorption in the prostate region is helpful for us to understand and estimate effects of the background optical properties on the reconstructed DOT images. As explained in Section 2, in Step 2 of HCM, the overall area of the anomaly was identified by selecting the full width at half

maxima (FWHM) of the recovered optical properties. If the recovered optical properties were not much higher than that of the background, no probable anomaly would be identified, similar to the case shown Fig. 4-7(c). So, the background absorption or contrast plays an important role in achieving high-quality DOT images of PCa. To estimate effects of the background optical properties,a total of 11 simulations were performed, as listed and shown in Fig. 6, by varying the optical properties or μa values of the prostate (i.e., background tissue) from 0.005 to 0.015 mm-1.

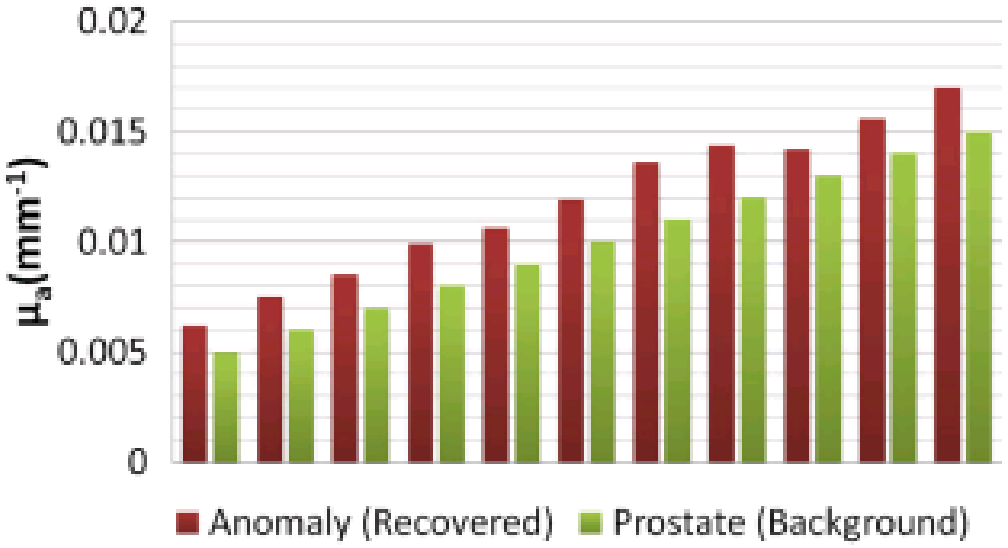

Figure 4-7 Comparison of absorption coefficients between the recovered anomaly and the prostate background after Step 2.

The absorption coefficients for the surrounding tissue and the rectum wall were fixed; the anomaly contrast was set to be 3 times of the background (0.015 to 0.045 mm-1) in all the simulations. The reconstructed results are plotted by comparing the recovered optical properties to the background in Fig. 4.7, which shows the recovered contrast from the background after Step 2 using HCM. We also calculated a recovery rate

(RR) based on the recovered absorption (RA) versus expected absorption (EA), as expressed by RR = (RA/EA)*100. Specifically, our calculations gave rise to an averaged RR of 40% over all 11 simulations. This 40% recovery rate of the expected contrast indicates that variations in background optical properties would still allow us to locate the probable location of an anomaly in Step 2 as long as the absorption contrast between the anomaly and background is 3 times.

The reason why we stopped at stage 2 was that this stage was very crucial for the success of our algorithm. If we succeeded to obtain an enough contrast in absorption with respect to the background in this step, we would be able to identify the region of interest for possible cancer lesions. Further steps would allow us to refine the size, location, and optical properties to achieve final reconstructed images with high quality. If our algorithm failed to recover a reasonable amount of contrast in Step 2, then the algorithm would fail to give rise to correct results. Indeed, this is the major difference between our approach and that by refs. [28,55]

4.3.5 Investigation of HCM on Effects of Different Noise Levels

To further understand and support HCM, we performed another simulation with an anomaly placed at 2 cm below the surface of rectum wall; the reconstructed images by HCM were generated while varying the noise levels at 1, 2 and 3% of measured signals. For comparison, we also reconstructed an image, as shown in Fig. 4.8(a), without any anomaly and with 1% noise added to the simulated data. Specifically, Fig. 4.8(a) was obtained after all the clusters were updated, illustrating a uniform distribution within the prostate region.

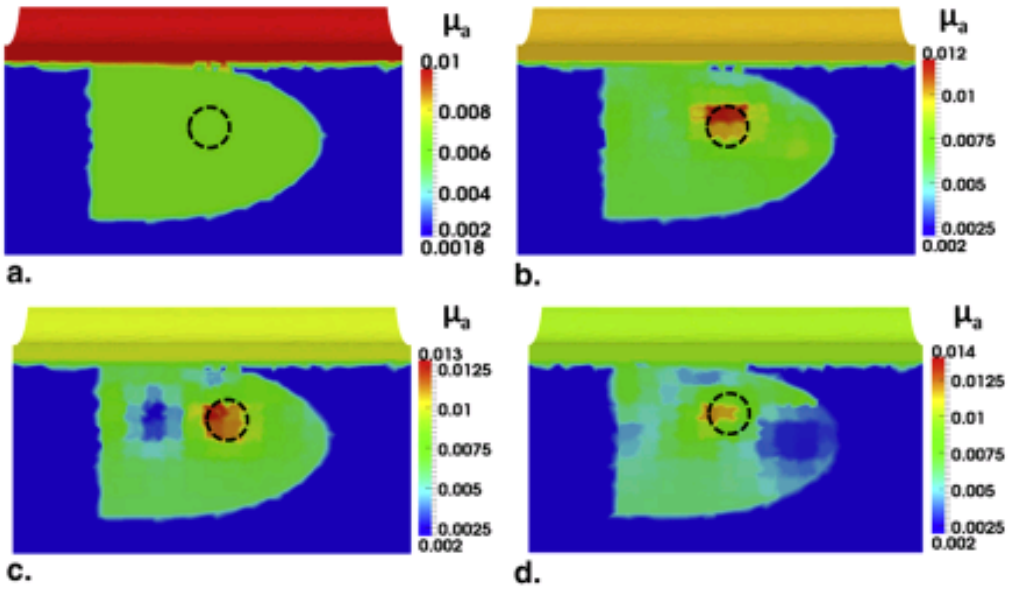

Figure 4-8: (a) shows the reconstructed image with 1% noise added to the data and without any anomalies. (b), (c), and (d) show the reconstructed image with 1%, 2%, 3% noise level, respectively.

On the other hand, Figures 4.8(b), 4.8(c), and 4.8(d) are the reconstructed images after Step 2 with 1%, 2% and 3% noise levels added to the data, respectively. From this set of figures, it is evident that HCM is robust if the noise level remains up to 1%. Figure 4.8(c) is slightly corrupted due to the 2% noise while Fig. 4.8(d) is heavily corrupted due to 3% noise.

4.4 Discussion

4.4.1 Investigation and Confirmation of HCM by Simulations

In this work, we have investigated the feasibility of TRUS-guided DOT imaging of human PCa through computer simulations and laboratory phantom experiments. While a trans-rectal DOT-only probe can possibly image cancer lesions within a human prostate

without ultrasound guidance, reconstructed DOT images suffer from lack of anatomical landmarks and poor spatial resolution, as well as a possible mixing of optical contrasts among the prostate gland, its surrounding tissues, and cancer lesions. In general, the spatial resolution of DOT imaging can be improved by increasing the number of optode channels; however, this is not a viable solution in our case because of the limited space available on a trans-rectal probe. Unlike previous work reported by references [28,55], which required anatomic images of PCa, we proposed and investigated a DOT-based HCM to image PCa by utilizing anatomic images of the prostate, not the images of PCa. This is because the former images can be readily available by clinical TRUS facility, which has very low sensitivity to provide PCa images.

While the combined TRUS-DOT method can improve accuracy of reconstructed DOT images, the problem is not completely solved since TRUS-DOT highly relies on the ability of TRUS to locate the PCa lesion. Given the fact that TRUS has low signature for PCa and that each region is assumed to be homogenous, the reconstructed DOT images could be erroneous. Thus, we further targeted the problem by (1) utilizing the available prior information on the locations of prostate, peri-prostate tissue and rectum wall and then (2) dividing the probable location of a prostate tumor or tumors into several clusters. This latter step made the prostate partially heterogeneous. The dimensions of the clusters were iteratively changed to limit the mixing of normal tissue with cancerous tissue and vice versa. Our HCM approach was implemented in four steps: The location of the absorber was identified in Steps 2 and 3 and the optical properties reconstructed in Step 4. The figures shown in Section 4.3.1 demonstrate excellent reconstruction results when HCM was used. Table 1 also reports that the recovered optical properties of the target and surrounding tissues were matched well with the expected values. Furthermore, the reconstructed images shown in Section 4.3.2 reveal the depth sensitivity of HCM: due

to the exponential decay of measurement sensitivity with depth, our method is limited to reconstruct an anomaly located not deeper than 3 cm in depth.

Moreover, Section 4.3.3 illustrates the ability of HCM to recover up to two anomalies located inside the prostate. The optical properties were overestimated when the two absorbers were sited at different depths. This overestimation resulted from the fact that the measurement sensitivity is biased toward more superficial nodes than those of deeper nodes. In Section 4.3.4, HCM has been investigated with 11 simulation-based cases on the effects of background absorption of the prostate tissue. The results indicate that a recovery rate of 40% for the target contrast could be achieved in all cases after Step 2 in HCM. Achieving a good contrast in a suspicious ROI after Step 2 is very crucial for the success of our algorithm. With a well localized target contrast after Step 2, further steps would allow us to refine the size, location, and optical properties to achieve final reconstructed images with high quality. Last, Section 4.3.5 shows that noise can have a significant impact on the image quality, while Section 3.6 confirms the performance of HCM by performing an actual experiment with a liquid tissue phantom. We demonstrated that a hidden absorber without prior location information was reconstructed with a recovery rate of 100% in its location and 83% in its optical property. Overall, the results indicate that both location and absorption contrast of the embedded absorber could be well reconstructed to meet the expected values when HCM was utilized.

4.4.2 Potential Usefulness of HCM for PCa Detection and Diagnosis

While the current development of HCM is not yet tested in the clinical settings by human prostate specimen measurements, it can be readily available for clinical investigations since the results from both computer simulations and laboratory experiments are supportive for HCM. The feasibility of implementing a TRUS-coupled

DOT probe has been demonstrated by ref. [28]. By combining such a TRUS-DOT optical probe with HCM, we may be able to develop a portable, diagnostic imaging device for early screening and diagnosis of PCa. Further testing with human prostate measurements and optimal refinements are the next steps in order to make this technology clinically useful in detection and diagnosis of PCa.

4.4.3 Limitation of the Method and Future Work

While the reported results for HCM are promising for improved detection of PCa, few weaknesses have to be recognized in order to either improve them in the near future or understand the limitation of the method. First, although HCM recovered well the absorption properties of imaged targets with a recovering rate of 95% in simulated results and of 83% in experimental results, excellent recovery in the target's shape was not much achieved. This may be partially due to the fact that the reconstructed images were defined by the FWHM in Steps 2 and 3 of HCM. Also, the inability to recover the target's shape resulted from the reflectance geometry of the probe setup (see Fig. 2) and the limited number of channels available for the measurements. It is known that a reduced number of source-detector channels would reduce image sensitivity and spatial resolution of DOT. The method proposed by references [56,57] could afford better results in recovering the shape of an anomaly when using circular or cylindrical probe geometries. This is because such geometries allow light to penetrate or pass through more tissue volumes under study, as compared to reflection geometries. Thus, while HCM approach is simpler to implement than that given by [56],it is not able to recover the imaged object's shape, partially due to the limited space (i.e., a human rectum) available to accommodate a fixed number of light sources/detectors, which are set in reflectance geometry for data

acquisition. Under the same argument, it is expected that the best spatial resolution of DOT-derived PCa images reconstructed by HCM would be in an order of 5-8 mm.

Second, in Section 4.2.1 it was stated the assumption of this study that variation in light scattering across the prostate and its surrounding tissues is minimal. This assumption was made because CW-based DOT measurements cannot provide enough independent data quantities to uniquely solve both light scattering and absorption coefficients of the imaged objects. With this assumption, it is possible to focus on DOT reconstruction of absorption coefficients of simulated PCa, using both simulation and experimental data, to implement and validate HCM. I acknowledge that the assumption of constant light scattering across the human prostate tissues may not be accurate, resulting in two negative impacts on our conclusion. (1) There exist variations in light scattering within the prostate tissue, which may create a large noise level to diminish the optical contrast between cancerous and normal prostate tissues. (2) PCa may result in light scattering changes, which may indeed be useful as an optical contrast for DOT but is ignored in the current HCM approach. In order to know whether or not these two negative impacts exist to HCM, it is necessary to perform human prostate specimen ex vivo and in vivo measurements with histology analysis confirmation, which is our next step in our research plan. Our expectation is that variations in light scattering within the prostate tissue are not large enough to diminish the optical contrast between cancerous and normal prostate tissues, based on previous reports on both breast cancer [58] and PCa studies [28,59]. If the variations in light scattering does affect DOT reconstruction results, we plan to modify Step 1 of HCM by utilizing a global algorithm to find both absorption and scattering from CW data. Further development to solve this problem will be reported elsewhere for our future work.

It is worthwhile to point out that if PCa does give rise to light scattering changes, they may help enhance the optical contrast for DOT as long as cancer tissues yield an increase in light scattering with respect to the normal prostate tissues, which seems to be the case according to the limited reports [60-62]. The rationale of increases in light scattering within PCa tissues is that cancer cells have enlarged nucleuses with a higher and irregular cell density, both of which result in a significant increase in light scattering. As mentioned in Section 2.1, CW-based DOT are sensitive only to $\mu_{eff}(r) = \mu_a(r) \bullet \mu_s'(r)$; an increase in due to PCa is mathematically equivalent to an increase in optical contrast for reconstructed DOT images, and thus our HCM will still function well or even better with an increase in contrast.

This chapter explored HCM method, which improves the image reconstruction in the absence of prior information on cancer location in PCa imaging with diffuse optical tomography. We believe that our hierarchical clustering method able to produce good results for experimental data is a significant step towards future investigation on the feasibility of the method for clinical applications. HCM will be particularly useful for the cases where prior location information of cancer is not clearly available, including PCa and others.

Chapter 5

Development of Optical Clip-On Rectal Probe for Existing TRUS Transducer

5.1 Introduction

The strength of diffuse optical tomography is providing functional information about tumors and weakness is lack of proving anatomical images. Since PCa measurements are endoscopic, the weakness of DOT makes the measurements blind folded. We cannot identify the exact anatomical location from where the image has been recorded. In order to overcome the problem, an optical clip-on type attachment for existing ultrasound transducer need to be developed. The advantage of the clip-on type attachment is two folded. First, the combination with ultrasound imaging system renders accurate and real-time anatomic information to correlate NIR optical system. Second, the available prior information will be inducted into the reconstruction algorithm to make it more robust. The difficulties in designing TRUS compatible optical probe are, (a) the axial dimension of the probe is restricted within 20~30mm (diameter). (b) It is required to deploy many optodes in a very limited space. On the other hand several researchers also developed transrectal probes for PCa imaging based on various technologies such as photoacoustics [63] DOT [55] and rectal MRI [64].

In my research work I, explored two types of TRUS coupled optical probe designs. In design 1, photodiodes were placed directly on the side of the TRUS probe to minimize the coupling loss. The rationale of this design is to minimize coupling loss and making the system economically viable. In design 2, 3d printing technology has been utilized. To be more specific probe has been designed to be compatible with a specific commercially available TRUS probe. Both designs have been tested with phantoms. In next sections I will discuss about two deigns in more details.

5.2 Design 1

Design 1 utilizes two optode arrays consisting of 8 source fibers and 8 photodiodes were placed on one side surface of the container in such a dimension that both source-to-source and detector-to-detector intervals were 1 cm between center to center and the distance between the source array and detector array was 2 cm. A broadband-pulsed laser source (SC-450, Fianium Inc., Eugene, Oregon) with a maximal output power of 40 mW (as measured at the tip of an

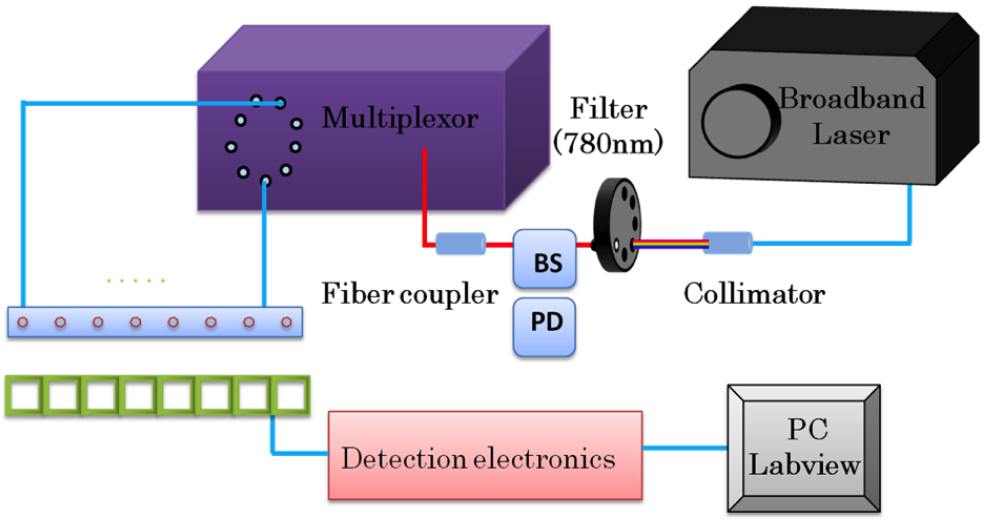

Figure 5-1 Instrumentation and probe setup utilized for laboratory phantom experiment. Eight sources and detectors were used for light delivery and detection. BS: beam splitter; PD: photodiode.

optical fiber) was utilized as the illumination source. Several photodiodes (OPT 101, Burr-Brown Corp., Tucson, Arizona) were implemented for diffuse light detection. Although our laser had a repetition rate of 20 MHz, due to the limited response speed of the photodiodes, we still considered our system as a CW system. As shown in Fig. 5-1, the laser output from the source was collimated and fed through a filter wheel where a

desired wavelength of 780 nm was selected. In order to calibrate light fluctuations from the laser source, a beam splitter (BS) was utilized, and a small portion of the beam was fed into another photodiode (PD) for further calibration. The larger portion of the light was coupled into another optical fiber and fed into a multiplexor. The multiplexor, as controlled by a computer, was connected to 8 silica optical fibers of 600 μm in diameter for light illuminations in sequence to 8 locations on an optode probe.

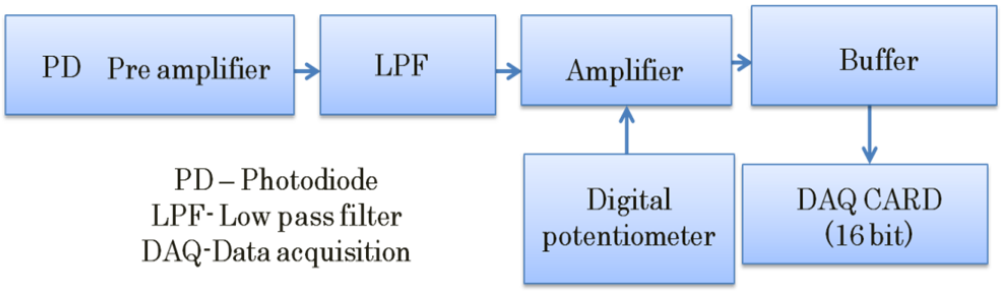

Figure 5-2 Flow chart depicting various stages of detection electronics utilized in proposed instrumentation.

For the detection electronics (see Fig. 5-2), the detected light was collected and converted to electrical signals by the photodiodes, an analog low pass filter (LPF) was employed to filter out unwanted higher frequencies. Next, the electrical signals were amplified using an operational amplifier in the inverting mode. The operational amplifier's gain was controlled by changing the resistance of a feedback resistor. A digital potentiometer was utilized such that the gain was controlled from the computer. Then, the electrical signal was further fed into a buffer amplifier which itself was an operational amplifier in a non-inverting mode with unity gain. Finally, we utilized a National Instruments DAQ card with 16-bit resolution to convert analog signals into a digital format and stored in the computer. The entire instrument control and data collection, including

light source switching, multiplexer sequencing, electrical gain selection, and data acquisition, were computer-driven using Labview software.

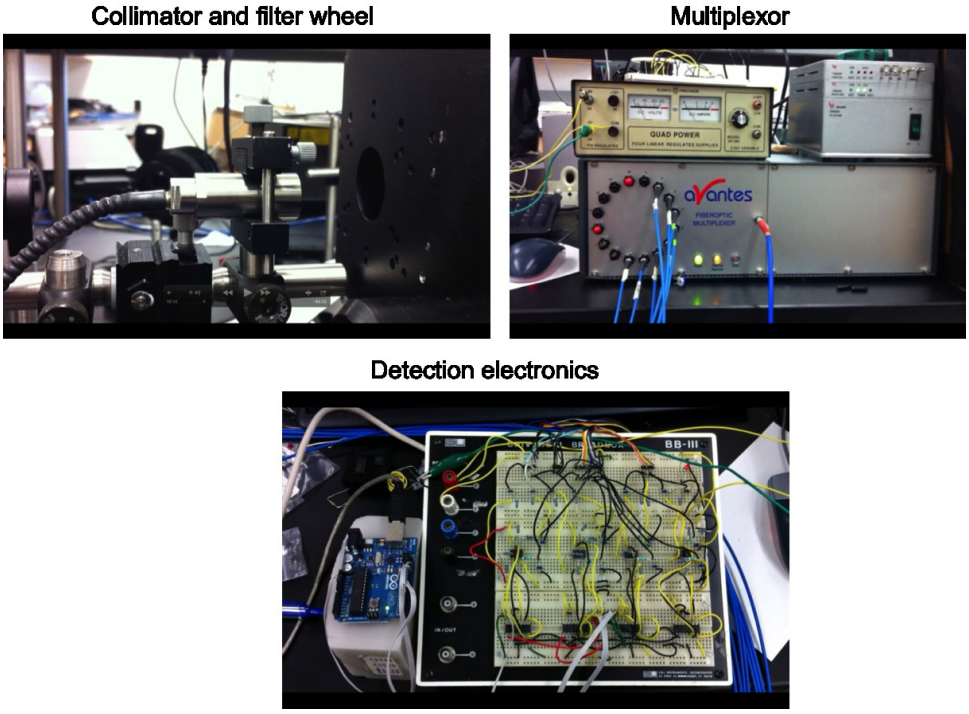

Figure 5-3 Pictures of the developed instrument

5.2.1 Validation

Although we demonstrated our HCM using a multilayered model in computer simulations, we utilized a single-layer phantom for experimental demonstration. We preferred a single-layer phantom because it could serve the need or confirm HCM with a relatively simple tissue phantom. Using a single-layered phantom with an absorber embedded inside, we

skipped Step 1 in HCM and directly started the reconstruction from

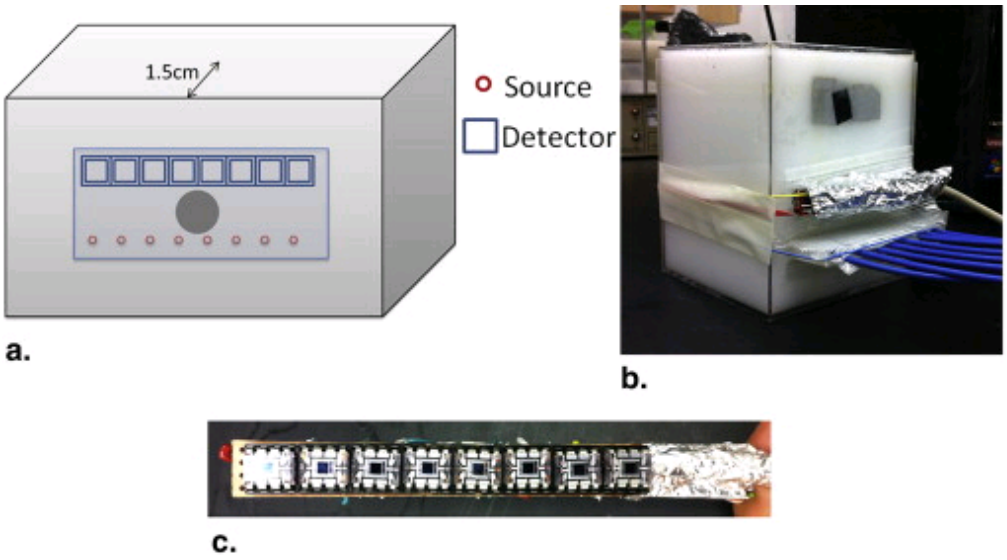

Figure 5-4 (a) Experimental setup used in this study. The probe was placed on one side of the tank to avoid contact with the intralipid solution. An absorber was placed 1.5 cm from the probe side of the tank. (b) Photograph showing the experimental setup. (c) Photograph showing the photodiode array.

Step 2. The reason for skipping Step 1 was that it involved inducing the prior information; for this particular case, we did not use any prior information. The phantom setup is depicted in Fig. 5-3(a) with a photograph of the actual setup shown in Fig. 5-3 (b). A homogeneous liquid tissue-mimicking phantom was prepared by filling a 15x10x10 cm3 container with 1% intralipid solution [see Fig. 5-3(b)]. An appropriate amount of India ink was added to the solution to make the absorption coefficient of the solution to be 0.01 mm-1. This solution served as a homogeneous background medium with an approximate μs' value of 1 mm−1 and μa value of 0.01 mm−1. A spherical 1-cm-diameter absorber with μa = 0.03 mm−1 was made and placed within the phantom solution and 1.5 cm from the source-detector array surface. The lateral dimension of the photodiode array from

end to end was ~ 8 cm, as illustrated in Fig. 5-3(c), with an active detection area of 0.23×0.23 cm2.

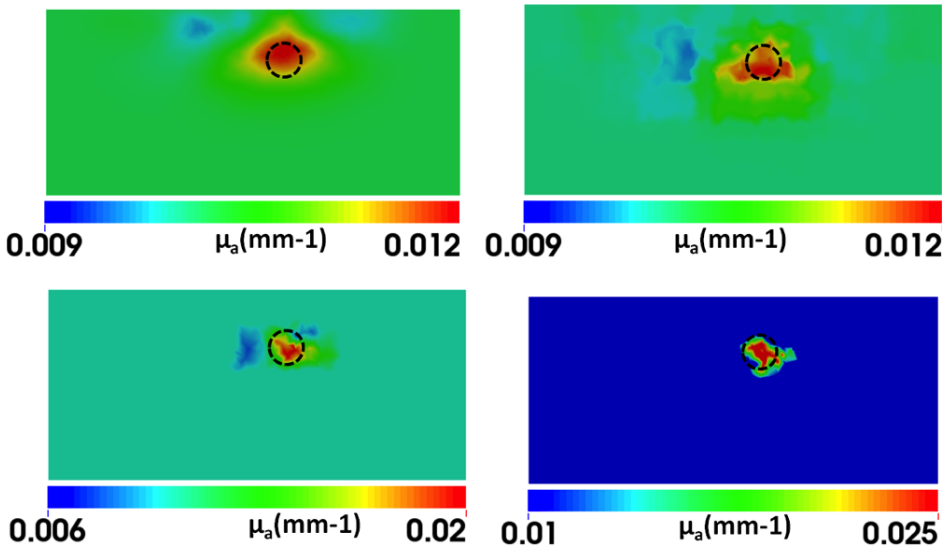

Figure 5-5 reconstructed μa values in mm-1 using (a) regular DOT iterative reconstruction and HCM after (b) step 2, (c) step 3, and (d) step 4. The dashed circles indicate the actual location of the 1-cm absorber with a depth of 1.5 cm below the measurement surface.

Panels in Fig. 5-4 provide overall comparisons among the reconstructed images that were obtained using the experimental setup given in Figs. 5-1 to 5-3. Figure 5-4(a) demonstrates the result obtained from the regular iterative DOT reconstruction technique. While this figure shows relatively good reconstruction in both location and size for the embedded absorber, we see very poor recovery in absorption contrast for the reconstructed object: the reconstructed value of μa was 0.012 mm-1 while the expected value was 0.03 mm-1. As seen in Fig. 5-4(b), Step 2 of HCM is able to determine the probable location of the absorber; Figs. 5-4(c) and 5-4(d) show the gradual improvement in the contrast recovery. By the end, both location and absorption contrast of the

embedded absorber were reconstructed much better to meet the expected values. Moreover, Table 3 shows that HCM resulted in a recovery rate of 83% for the embedded target, without using any spatial prior information. Moreover, Table 3 shows that HCM resulted in a recovery rate of 83% for the embedded target, without using any spatial prior information.

Table 5-1 comparison of reconstructed μa value between regular DOT reconstruction and HCM for experimental data.

	Target (mm-1)	Recovered (mm-1)	Recovery Percentage
DOT reconstruction	0.03	0.0115	38.3%
HCM	0.03	0.025	83.3%

5.3 Design 2

In design 1 the probe is handcrafted and, the process was time-consuming and it is too far away from real word application. Due to anatomical location of the prostate, the probe design should strictly follow the diameter requirements. Moreover, the probe should be fabricated with respective to the existing TRUS probe. Today several TRUS probes are commercially available and their usage depends up on the doctors training. In order to test DOT technology on human subjects proposed design should be scalable. In order to address the above problems 3d printing technology was utilized. In design 2, commercially available DOT system has been used to image anomalies.

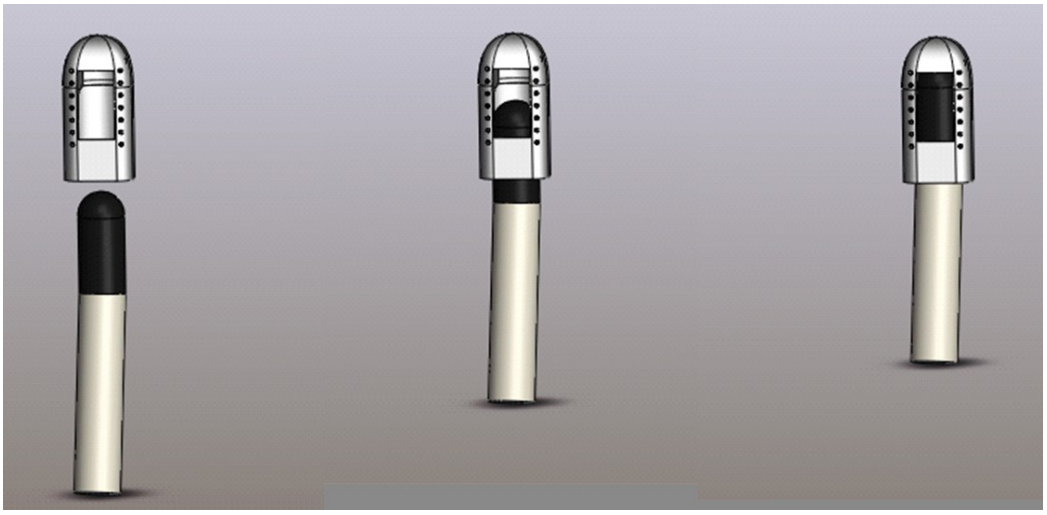

Figure 5-6 Drawing shows the insertion of TRUS probe into clip-on optical probe

Figure 5-5 shows the fitting mechanism with the existing probe. Figure 5-6 shows three generations of probes developed. In generation-1, plastic pipe has been cut and drilled to hold the optical fibers. In generation-2 3d-probes has been designed using software (Solidworks) and printed using 3d printer. Four designs have been considered and two-part design has been finalized in generation-2 due to the ease of placing optical fibers. In generation-3 the two parts has been attached with silicone. . The advantage of silicone is it can create a rubber mould for TRUS probe inside the optical clip-on.

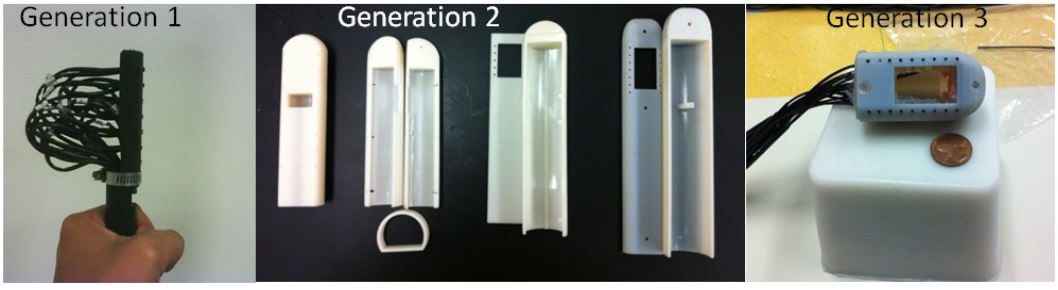

Figure 5-7 pictures showing various generations of the optical Clip-on probes developed

5.3.1 Validation of Clip-On Probe

In order to test the designed probe solid phantoms has been fabricated. Rationale for fabricating solid phantoms are (1) They can be used of system calibration before the experiment (2) can be used repeatedly during the optimization of probe geometry and validating algorithms (3) They are long lasting and can be transported easily. For fabrication the protocol below has been followed.

Volume of both silicone and silicone catalyst was measured and set to be in 10:1 ratio. Large Titanium oxide particles are mixed with silicone catalyst and sonicated for 40 mins. Occasionally steel spatula was used to mix the catalyst. Next, india ink was mixed with silicone thoroughly with the help of blender. Silicone catalyst was mixed with the silicone thoroughly again with the blender. This process mixes lot of air with the silicone and it needs to be degassed. Silicone with air bubbles was poured into 3X large container and placed into a vacuum chamber. In vacuum, while air is getting out, the silicone expands (the reason for 3X large container) and compresses after some time. Silicone was degassed for is 30 mins. Next, the solidifying silicone was poured into a mould and was allowed to cure for 24 hrs. Pieces of 1X1X1 cm3 were cut from the solid phantoms and utilized as absorbers for the experiments.To validate proposed algorithms and developed clip-on probe, six experimental data sets has been considered. Specifically two experiments have been performed and in each experiment, three datasets have been recorded. The overall goals of the experiment are (1) to validate HCM method with clip-on probe, (2) to check the reconstructions with the prostate related absorption and scattering coefficients, (3) to prove that the reconstructed image is related to the embedded inclusion and not from an artifact/noise. To achieve the above goal an absorbing/scattering inclusion fixed at a location and the clip-on probe was translated horizontally. The expected results are the images showing the movement of the inclusion.

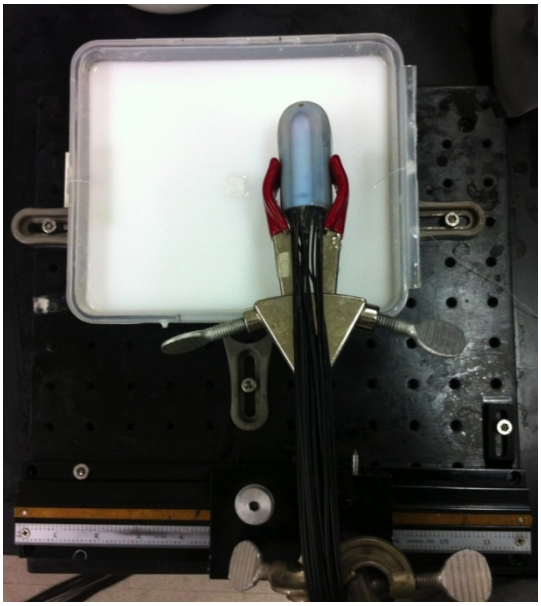

Figure 5-8: Experimental setup showing the horizontal translation of the probe across the absorber (located at center of the plastic container). Pictures were taken after the experiment.

For both experiments, a homogeneous liquid tissue-mimicking phantom was prepared by filling a container with Intralipid solution. A cubical inclusion with dimensions of 1X1X1 cm has been placed at 1.5-cm depth from the surface of intralipid with the help of a string (less than 1mm diameter). The clip-on optical probe was placed on the surface of the intralipid by holding it with a test tube clamp. The other side of the test tube clamp was connected to a linear translational stage. See Figure 5-8: Experimental setup showing the horizontal translation of the probe across the absorber (located at center of the plastic container). Pictures were taken after the experiment.. The initial location of the probe was adjusted such that one side of the source-detectors sees the inclusion (Left position with respective to the inclusion). Next, the probe has been translated to the center position (both sides of sources and detectors see the inclusion). Next, the probe has been translated to the right position. Finally the probe was placed on the calibrating

phantom to collect the reference data. Experiment 1 was designed to simulate a change in scattering and experiment 2 was designed simulate a change in absorption. In experiment 1, the background absorption was set to 0.0047 mm-1 and scattering was set to 0.51 mm-1. The absorption of inclusion is 0.0046 mm-1 and scattering is 1.05 mm-1. In experiment 2, the background absorption was set to 0.005 mm-1 and scattering was set to 0.69 mm-1. The absorption of inclusion is 0.01 mm-1 and scattering is 0.69 mm-1. These values are within the limits of PCa measurements from previous study.

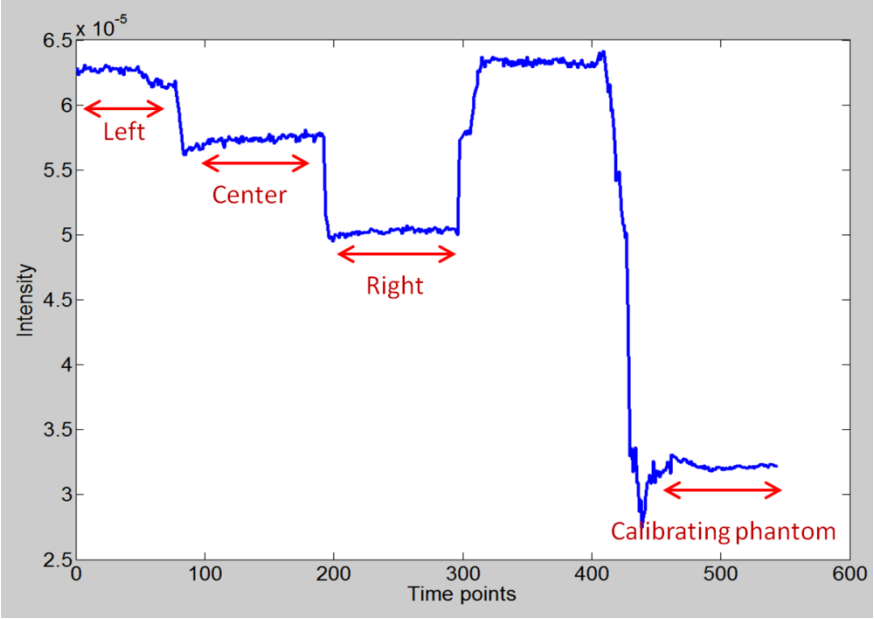

Figure 5-9 Raw data from a channel showing the changes in the data while translation of the clip-on probe

In the reconstruction, the probe's location was fixed so there should be movement in the reconstructed location. Figures 4.22 and 4.23 clearly show the horizontal moving absorber. The locations of the absorber were also recovered accurately. The above experiment proves that the proposed reconstruction methodologies can reconstruct images with low contrast. On the other hand the

experiment also proves that the designed clip-on probe can be useful to image PCa. The results so far are qualitative more quantitative analysis will be done.

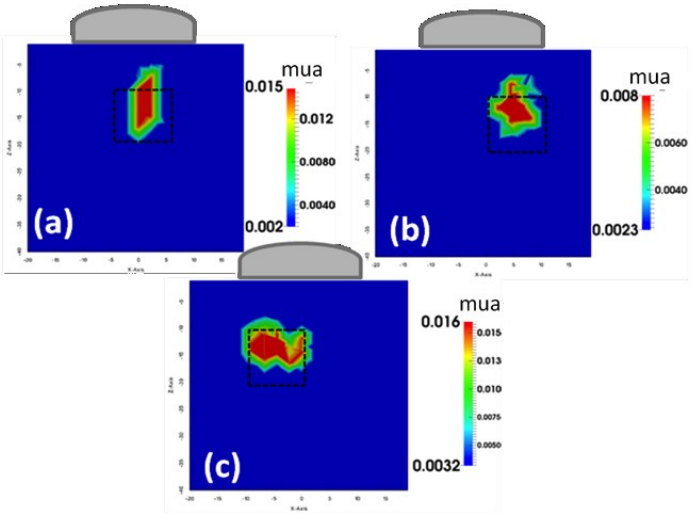

Figure 5-10 Panels (a) (b) and(c) shows the reconstructed images which depicts the translation of the absorber (scattering contrast). Dotted rectangles shows the target locations

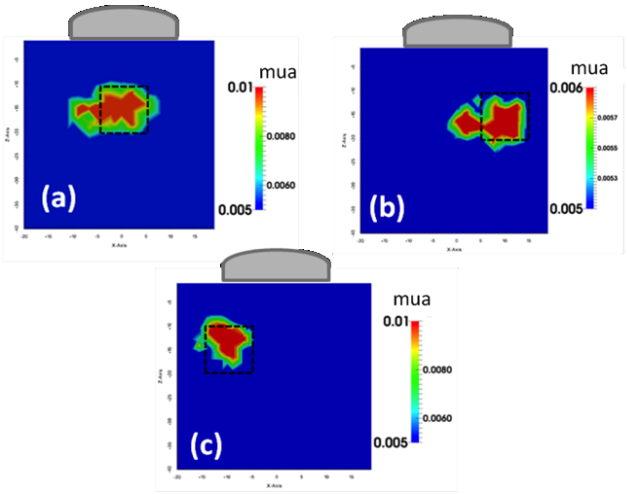

Figure 5-11 Panels (a) (b) and(c) shows the reconstructed images which depicts the translation of the absorber (absorption contrast). Dotted rectangles shows the target locations

5.4 Conclusion

In this chapter, two types of TRUS coupled optical probe designs were explored. In design 1, photodiodes were placed directly on the side of the TRUS probe. In design 2, 3d printing technology has been utilized to create a clip-on optical probe compatible with existing clinical TRUS facility. Both the designs were tested successfully by utilizing laboratory phantoms. However, two major issues have to be discussed when using a clip-on optical probe. (1) Probe contact: Measurements in DOT are very sensitive to optical contact between the optodes and tissues. It is very critical to ensure sufficient contact or good optical coupling. However, in transrectal measurements, it is impossible to learn such information because of anatomical location. (2) Calibration: Calibration in DOT is also very sensitive to bend losses in the optical fiber.

Chapter 6

Measurement of Bulk Optical Properties of Ex-vivo Prostate Tissues

6.1 Introduction

Prostate cancer (PCaa) is one of the leading causes among cancer deaths in men in the United States. Despite many advances in the diagnostic techniques, fundamental questions about how to differentiate the aggressive PCaa from localized PCaa still exists. Statistics indicate that the lifetime risk of PCaa for men in the United States is as high as 15.33%, but only 2.71% of men will die of it [65]. An autopsy study with 249 cases found that 64% of men in their seventh decade of life had undiagnosed invasive PCa and died of other causes [66]. Current treatment options for localized PCa such as radical prostatectomy and external radiation therapy (XRD) are effective in curing patients, but they carry significant risks. A 5-year outcome study indicates that, 79.3% patients suffered from erectile dysfunction due to radical prostatectomy 63.5% due to XRD. Incontinency rates about 15% in radical prostatectomy and 4% in external beam radiotherapy patients. Bowel urgency and painful hemorrhoids were more common in the external beam radiotherapy group than in the radical prostatectomy group. On the other hand, radiation therapy is associated with acute proctitis and cystitis at the rates of 20% and 30% respectively [67]. There are dilemmas associated with the diagnosis and prognosis of PCaa which has lead to the over diagnosis and over treatment of the disease.

Prediction tools for PCaa have been developed to assist in the accurate diagnosis and treatment of the disease, and address a wide variety outcomes; e.g. the Partin tables [68,69], Partin nomogram [70], Kattan and Stephenson nomograms [71] and, CAPRA score [72]. The Partin table uses clinical stage based on digital rectal exam (DRE), Gleason score (GS) of the prostate needle biopsy, and serum prostate specific

antigen (PSA) to predict stage [73,74]. These specimens subject to sampling error since they are obtained from blind random biopsies of the prostate. Imaging modalities are also used to determine PCaa stage and aggressiveness; however, these also have several limitations regarding sensitivity and cost of the procedure. Positron emission tomography has low sensitivity and is unable to detect differences between benign and malignant tissue. Novel methods, such as multiparametric MRI, have demonstrated the potential for improved detection of high grade cancer and risk stratification in newly detected PCas, but confirmatory biopsies are still required. Other imaging modalities such as ultrasound and computed tomography also lack sensitivity and specificity. Further, these modalities often require the use of intravenous contrast to improve detection rates.

Because of the currently employed imperfect tools, many men undergo unnecessary treatment for a disease that would not have caused their deaths. Studies estimate that, in order to prevent one PCa-specific death, 100 men with low-risk PCa need to be treated [75,76]. Another study indicates that, 42% of men diagnosed with PCa by prostate specific antigen (PSA) testing will be over-diagnosed [77]. Over-diagnosis results in increased health care costs and unnecessary morbidity from treatment-related complications. Patients with life expectancy of less than 10 years may die of other causes before experiencing any benefit from screening but are still exposed to potential harms from the screening test itself, a resulting diagnostic work up, or unnecessary treatments. An improved method to detect PCa and risk-stratify those with PCa prior to definitive therapy may reduce the over-treatment rate, while maintaining or improving mortality.

Investigation of PCa by DOT has been very limited. Thus far, in-vivo optical properties of prostate have been reported by ([60-62,78-80]), and ex-vivo specimen were investigated by [81-83]. Specifically [80] investigated PCa with interstisial trans-pernial

method to collect μ_{eff} using CW diffuse optical technique. [61,62,78,79] performed same methods(interstitial trans-pernial method using CW light) on recurrent PCa(RPCa) and utilized differential evolution algorithm developed by [84] to recover both absorption and scattering of RPCa. Svensoon et al. [60] utilized time domain technique to record absorption and scattering of PCa using interstitial trans-pernial method. In ex-vivo prostate measurements [81,82] examined normal prostates using CW light. Prostates were collected from cadaver donors who died from non urological cause. Sharma et. al [83] examined PCa and benign tissues using auto-fluorescence lifetime spectroscopy (AFLS) and light reflectance spectroscopy (LRS). AFLS used excitation at 447 nm with four emission wavelengths (532, 562, 632, and 684 nm), where their lifetimes and weights were analyzed using a double exponent model. LRS was measured between 500 and 840 nm and analyzed by a quantitative model to determine hemoglobin concentrations and light scattering. The optical signatures of prostate and PCa are scattered, often measured though invasive approaches.

Our hope or hypothesis for this study is that DOT has the ability to image PCa and to differentiate aggressive cancer from slow growing cancer in order to help clinicians make necessary treatment decisions. diffuse optical tomography has a weakness of not being able to provide anatomical images or locations for the measured organs or specimens. Since PCa measurements are endoscopic, the weakness of DOT makes the measurements blind folded. This implies that we cannot identify the exact anatomical locations of the measurement sites and reconstructed images. In order to overcome this problem, an optical attachment that can be clipped on an existing TRUS probe needs to be developed. In this study, we measured optical signatures of both benign versus PCa tissues from ex vivo human prostate specimens right after prostatectomy in order to determine the feasibility of DOT as a possible imaging tool.

6.2 Experimental Methods

We investigated the feasibility of using DOT to measure the differences between benign and cancerous tissues by utilizing frequency domain (FD) machine. Specifically ISS oximeter (OxiplexTS, ISS Medical, Champaign, IL) with four channels (Four sources and

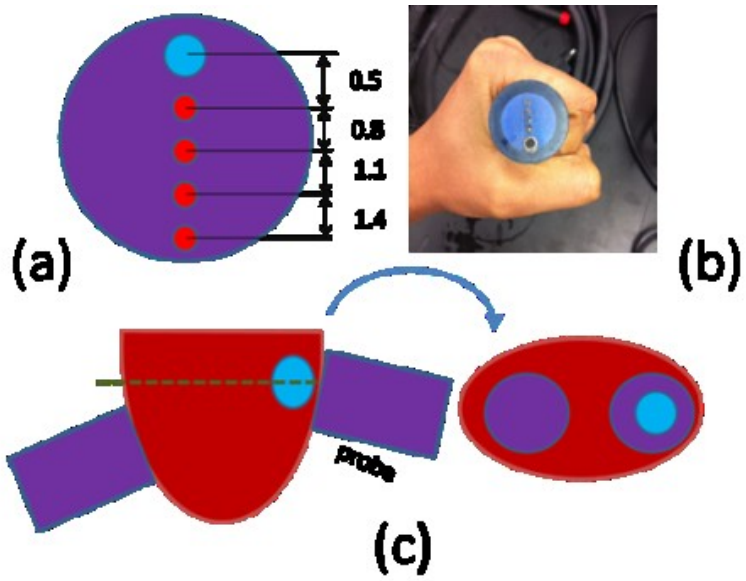

6-1: (a) Source detector geometry used; (b) showing the actual probe used for the measurement; (c) explaining the measurement procedure

one detector) has been utilized. Although ISS oximeter, designed to measure and determine the absolute values of HbO, HbR, and HbT in tissues, a single wavelength (i.e 811nm) has been utilized in this study. Reduced scattering coefficient and absorption coefficient are recorded in the measurements.

Fig. 6-1 (a) shows the source-detector geometry of the customized probe holder made for the measurements. The nearest distance between the source and detector pair detector is 0.5 cm and the farthest is 1.4 cm. In Fig. 1a, the large blue dot represents the detection fiber bundle, while the other 4 red dots correspond to the detection fibers. The

custom probe holder was designed (in Solidworks®) based upon the size of the prostate (Fig. 6-1 (b)) and printed using a 3d printer (Makerbot®). Measurements were performed at two areas of the prostate, i.e., on (1) prostate capsule and (2) intra prostate tissue. Within the above two areas, the two regions were measured; they are (i) near and (ii) far away from a highly suspicious cancer region. The FD-NIRS data were collected on the capsule first (see Fig. 6-1(c)) before the prostate was bivalve, followed by another set of measurements directly on top of the suspicious region after cutting it open. Then, the measured tissue samples were removed from the gland (inked with appropriate colors), and sent to the histology lab for histology confirmation. Initially, with 811nm wavelength scattering of prostate tissues was measured. Later, encouraged by the differences in scattering between benign and cancerous tissues, absorption was also measured. Finally, we also expanded the study by adding one more wavelength (785 nm).

Fifteen prostate specimens were measured and five measurements were taken at each site by rotating the probe by ~30 degrees to cover or average the local region yielding 300 data points (75 of each tissue type). After pathological analysis, cancer locations of three specimens were turned out to be benign tissue. Therefore, in our analysis, we considered them as benign tissues, although the measurements were made at suspicious cancer locations. The acquired data are analyzed in two ways (1) By considering each data point independent (2) and by averaging the five measurements, which were taken at each site by rotating the probe by ~30 degrees and considering it as one data point. Both types of analysis were statistically analyzed and the details of the analysis were discussed in the next section.

6.3 Statistical Analysis:

Both scattering and absorption data were analyzed with one-way ANOVA and post-analysis with Tukey's multiple comparison test. Tukey's test is essentially a t-test, except that it corrects for error rate with respect to the experiment (when there are multiple comparisons being made, the probability of making a type I error increases).

To further check the validity of the estimators, residual analysis was performed in order to check ANOVA assumptions. Specifically the following assumptions were checked.

(1) Check for outliers: Outliers in the data has been checked by two ways (1) identifying the outliers by visualizing the data, i.e. plotting the data (Tissue type vs residuals) (2) By statistical test such as bonfferoni outlier test. In bonferroni outlier test, studentized deleted residuals (SAS RSTUDENT) are calculated by

$$t_{it} = e_{it}\sqrt{\frac{n-v-1}{SSE(1-\frac{1}{r_i})-e_{it}^2}}$$

If $\left|t_{it}\right| > t_{n-v-1,\frac{\alpha}{2n}}$ then it is concluded as outlier.

(2) Check for normality: Normally distributed errors have been checked by plotting Q-Q plot and calculating the sample correlation $\hat{\rho}$ between the residuals and their normal scores. Next cutoff $c(\alpha, \mathrm{n})$ has been taken from Neter et al. (1996). If $\rho < c(\alpha, \mathrm{n})$ then it is considered as a violation of normality.

(3) Check for constant variance: Anova assumes that the error variables have similar variances for each factor. To check for constant variables two tests modified levene test has been performed.

In modified Levene test, initially sample median $\tilde{y}_i$ was calculated. Next absolute differences d_{it} are calculated by $d_{it} = \left| y_{it} - \tilde{y}_{i} \right|$. After calculating d_{it} one-way ANOVA will be used to test the differences in d_{it} observations. The following hypothesis will be tested. Ho: Variance is constant. H_A: Variance is not constant. Decision rule: if F value from ANOVA > α=0.05 fail to reject Ho which means variance is constant.

(4) Check for serially correlated errors: To check serially correlated errors data will be plotted across measurement order and jaggedness will be examined. If the data exhibits random jaggedness there are no serially correlated errors and vice versa.

6.4 Results

A total of 16 patients were enrolled for this part of study (12 patients for absorption). Mean (standard deviation) patient age was 60.7 (6.0) years. After the measurements, pathological analysis was performed to confirm the cancer and benign regions. One out of 15 samples was excluded because the sample has necrotic tissue. After data collection, we sorted the data into cancer and benign according to the pathological analysis. For example, if the measurement from cancer locations turns out to be benign then we treated that sample as benign. Table 1 shows the final number of samples after sorting into four tissue types.

Table 6-1 Table showing number of measurements made per tissue type

Tissue Type	Scattering	Absorption
Cancer on capsule	11	9
Benign on Capsule	18	14
Cancer in Parenchyma	14	12
Benign in Parenchyma	16	12

Figure 6-2 shows the calculated scattering coefficients from the ex vivo human prostate measurements performed on intra- and extra-capsule tissues in two areas (i) near and (ii) far away from a highly suspicious cancer region. It is evident that the pathology-confirmed cancer has higher scattering and absorption values in both areas than those of benign tissue. Moreover, the measured optical properties of PCa taken from intra- and extra-capsule tissues are very consistent. The mean reduced scattering for cancer on capsule is 7.52±1.26 cm-1 and on parenchyma is 7.73±1.51 cm-1. The benign tissue on the capsule has reduced scattering about 5.37±1.27 cm-1 and parenchymal benign tissues has about 5.40 ± 0.9 cm-1. The p-values from ANOVA (<0.001) indicate that there is a significant difference in each optical property between cancer and normal tissues. We also did Tukey's pairwise comparisons (violet bars in figure) and statistically conclude the following: (1) we are 95% confident that the optical coefficients of cancer on the capsule are different from those of benign tissues on and within the capsule of the human prostate. (2) We also are 95% confident that the optical coefficients of PCa within the capsule are different from those of benign tissues on and within the prostate glands.

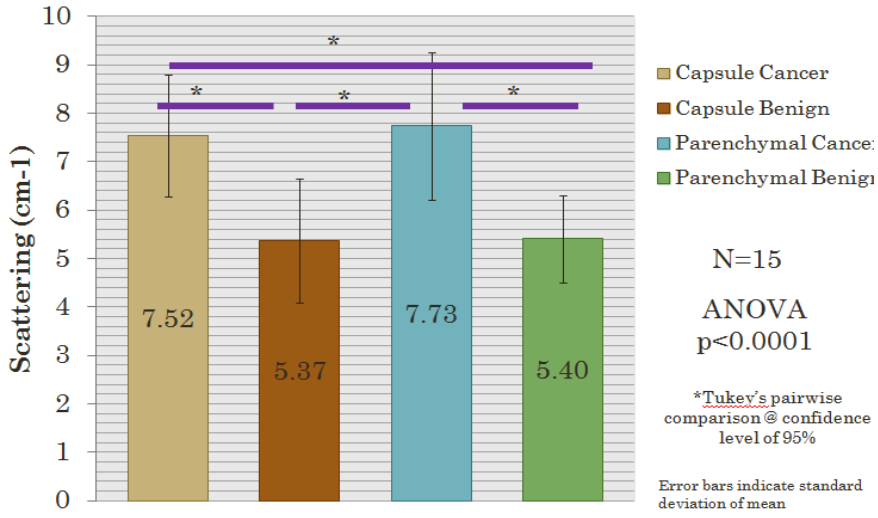

Figure 6-2 Bar plot showing the optical scattering of four prostate tissues. Error bars represents standard deviation of the mean. * represents significant differences with Tukey's pairwire comparisons

Fig. 6-3 shows the absorption results from the actual measurements were performed on intra- and extra-capsule tissues in two areas (i) near and (ii) far away from a highly suspicious region. It is evident that the cancer has slightly higher absorption in both areas than that of benign tissue. Moreover, the measurements from intra- and extra-capsule tissues are similar. The mean absorption coefficient for cancer on capsule is 0.125±0.02 cm-1 and on parenchyma is 0.13±0.027 cm-1. The benign tissue on the capsule has reduced scattering about 0.109±0.026 cm-1 and parenchymal benign tissues has about 0.094 ± 0.011cm-1. The p-values from ANOVA (<0.001) indicate that there is a significant difference in each optical property between

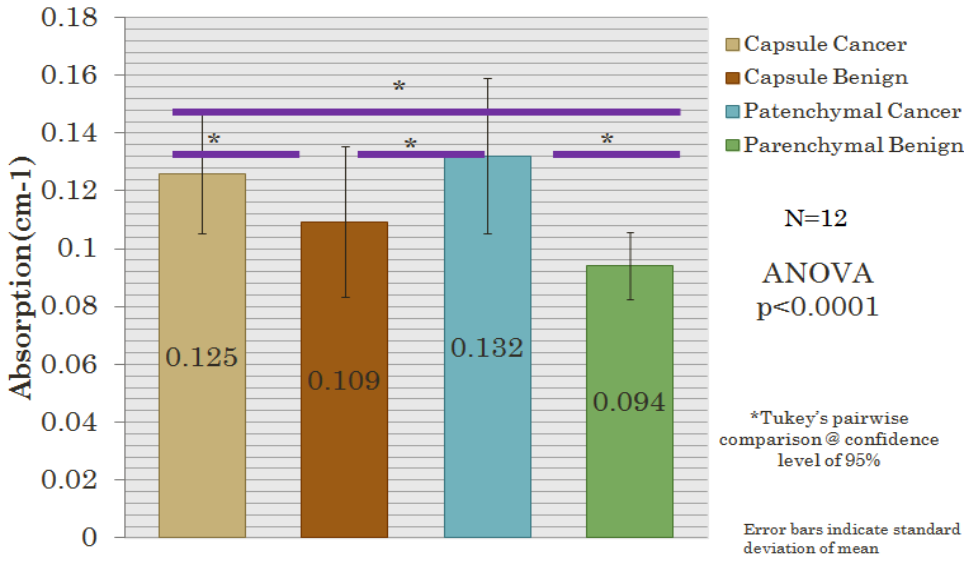

Figure 6-3 Bar plot showing the optical absorption of four prostate tissues. Error bars represents standard deviation of the mean. * represents significant differences with Tukey's pairwire comparisons

To check assumptions of ANOVA outliers in the data has been checked with Bonferroni outlier test. Figure 6-4 (a) shows modulus of studentized deleted residuals of scattering data vs scattering in four tissue types measured. From the figure it is clear that all $|t_{it}|$ values < threshold value 3.505. (Threshold= $t_{n-v-1,\frac{\alpha}{2n}}$ = $t_{295\text{-}4\text{-}1\ 0.05/2*295}$). It indicates that statistically there are no outliers in the data. Similarly, Fig.Figure 6-4(b) shows studentized deleted residuals of scattering data vs scattering in four tissue types measured. From the figure it is clear that all $|t_{it}|$ values < threshold value 3.51. (threshold= $t_{n-v-1,\frac{\alpha}{2n}}$ = $t_{235\text{-}4\text{-}1,0.05/2*235}$). It indicates that statistically there are no outliers in the data. Threshold has been generated from SAS statement "t=tinv(1-alpha,df)"

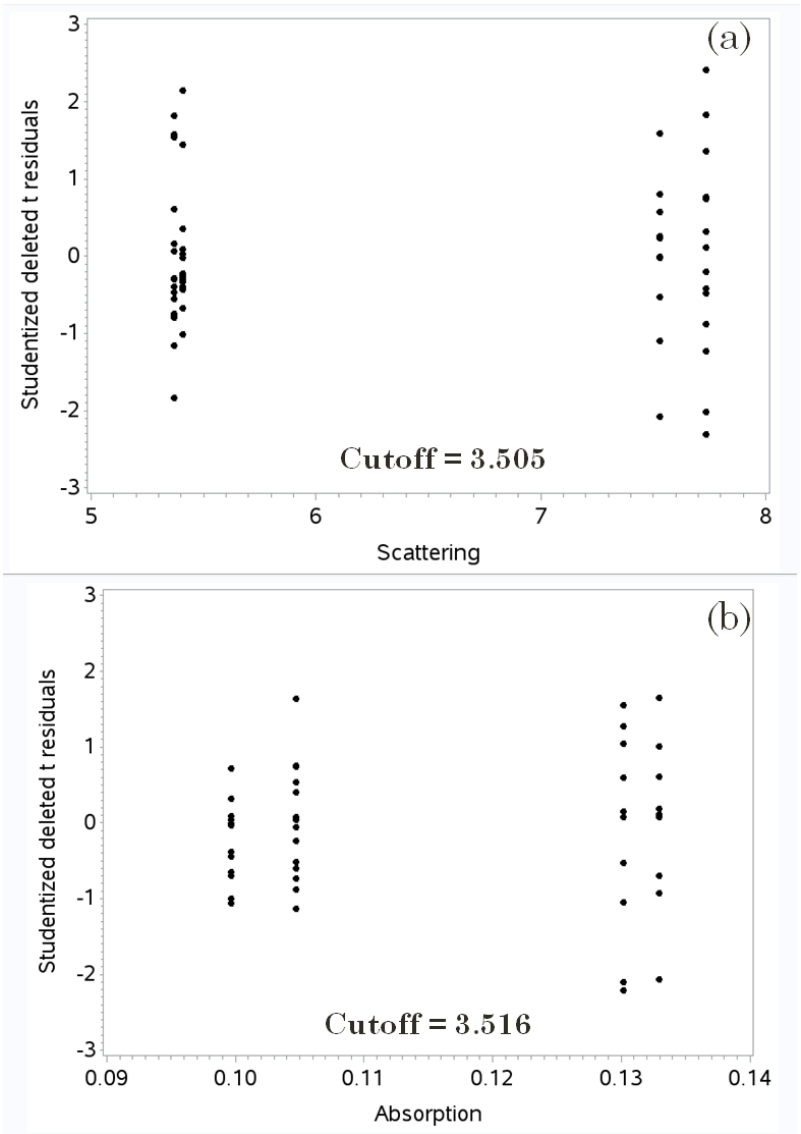

Figure 6-4 Plots (a) and (b) showing studentized deleted t residuals and cutoff values for scattering and absorption.

Figure 6-5 (a) and (b) shows normal probability plots of both scattering and absorption. X axis indicates the normal scores and y axis indicates the corresponding residuals. Next, sample correlation (Perason correlation coefficient) $\hat{\rho}$ between the

residuals and their normal scores. The cut off c(α,n) = c(0.01,59) for scattering is 0.971. From the figure $\hat{\rho}$ > c this indicates that scattering data is normally distributed. Similarly, the cut off value for absorption is c (α,n) = c(0.01,47) is 0.963. From the figure $\hat{\rho}$ > c this indicates that scattering data is normally distributed.

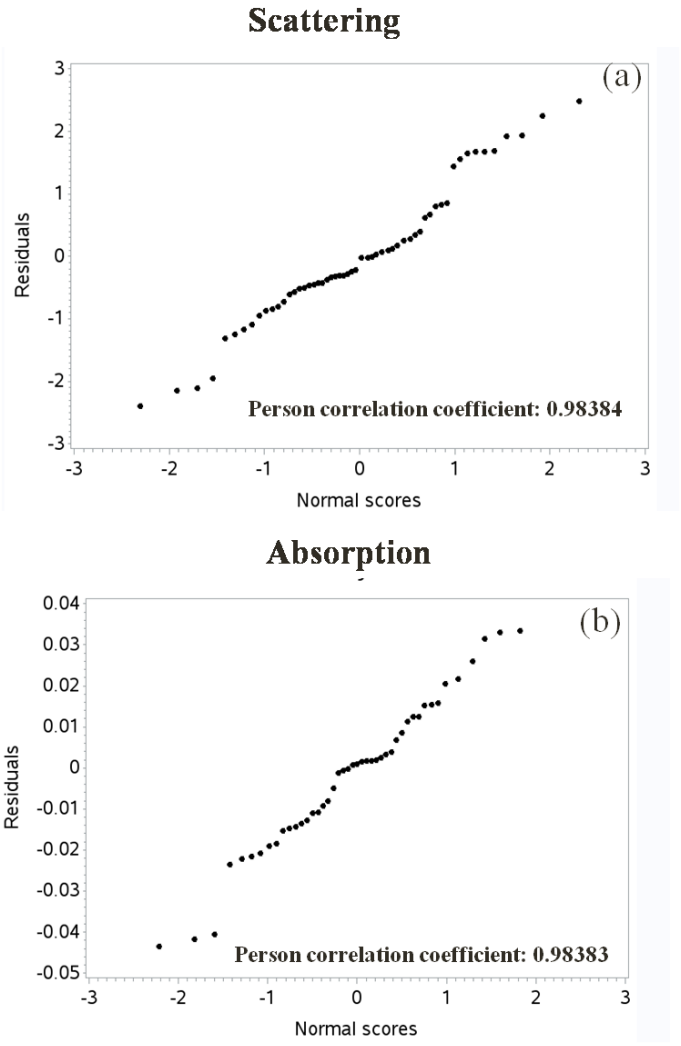

Figure 6-5 Panels (a) and (b) showing the normal probability plots of both scattering and absorption respectively and person correlation coefficient respectively

The F value from ANOVA for modified levene test is 0.1536 for scattering data and 0.81 for absorption data. For both scattering and absorption F value > α=0.05. So the null hypothesis is rejected which means variance is constant. Therefore, from Modified Levene test, it is clear that the scattering and absorption data has constant variance.

Figures 6-6 and 6-7 depicts the plotted residuals vs. measurement order for scattering and absorption respectively. From Figure 6-6, it is clear that the data has random jaggedness except in prostate benign case. There are slight trends in parenchymal benign case, but overall we can say that there is no serial correlation. From Figure 6-7 slight downward trend appear in the beginning of measurements parenchymal benign case, later there is jaggedness. Overall the data has random jaggedness.

The statistical analysis above indicates that all model assumptions were satisfied. Since normality and constant variance is satisfied we do not need transformation of the response variables (scattering and absorption) and the data has constant variance with normally distributed errors then weighted least squares is not applicable in this case.

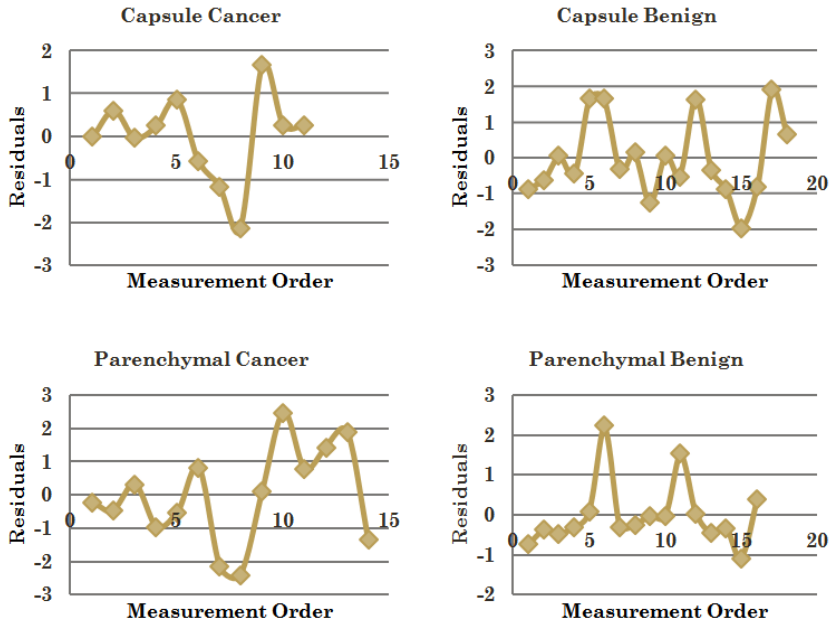

Figure 6-6 Residuals Vs Measurements order

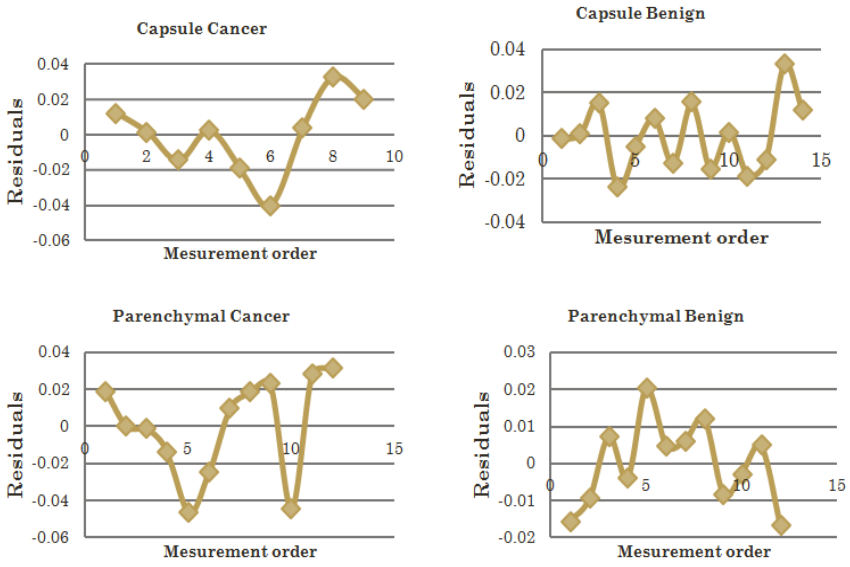

Figure 6-7 Residuals Vs Measurements order

6.5 Discussion

As specified in previous chapters the long-term goal is to develop a combined NIR and TRUS probe, which can be used to detect and risk-stratify PCa prior to definitive therapy. With combined NIR and TRUS, the information from TRUS can be utilized as prior in DOT reconstruction. While the combined TRUS-NIR method improves accuracy of reconstructed DOT images, it highly relies on the ability of TRUS to locate the PCa lesion. The above problem has been solved by creating hierarchical clustering method, which improves the image reconstruction in the absence of prior information about cancer in PCa imaging using DOT. This Chapter explored PCa imaging using DOT by measuring optical signatures of both benign versus PCa tissues from ex vivo human prostate specimens. In this section, I compared the optical properties from our study with previously published optical properties of prostate. In the next paragraph, morphological reasons behind increase of scattering and absorption in cancer tissues will be discussed.

Origin of scattering and absorption signals has been well understood and described in the literature of biomedical optics. Micrometer-sized organelles such as vesicles, mitochondria, and nuclei are responsible for the origin of scattering signal. The increased scattering coefficient in cancerous tissues indicates larger cell sizes and higher densities (cancer cells are poorly differentiated). In our study, frequency domain data collected form ex-vivo prostate specimen shows a consistent scattering and absorption differences between benign and cancerous human prostate tissue. Before explaining the specific reason for increase in scattering, the basic morphology of prostate tissues will be explained.

The normal prostate is composed of glands and fibromuscular stroma(see Figure 6-8(a) and (b)). The epithelial cells of the glands are organized as acini(cluster of cells resembles berry) that secrete into the luminal space that converges upon a duct and into

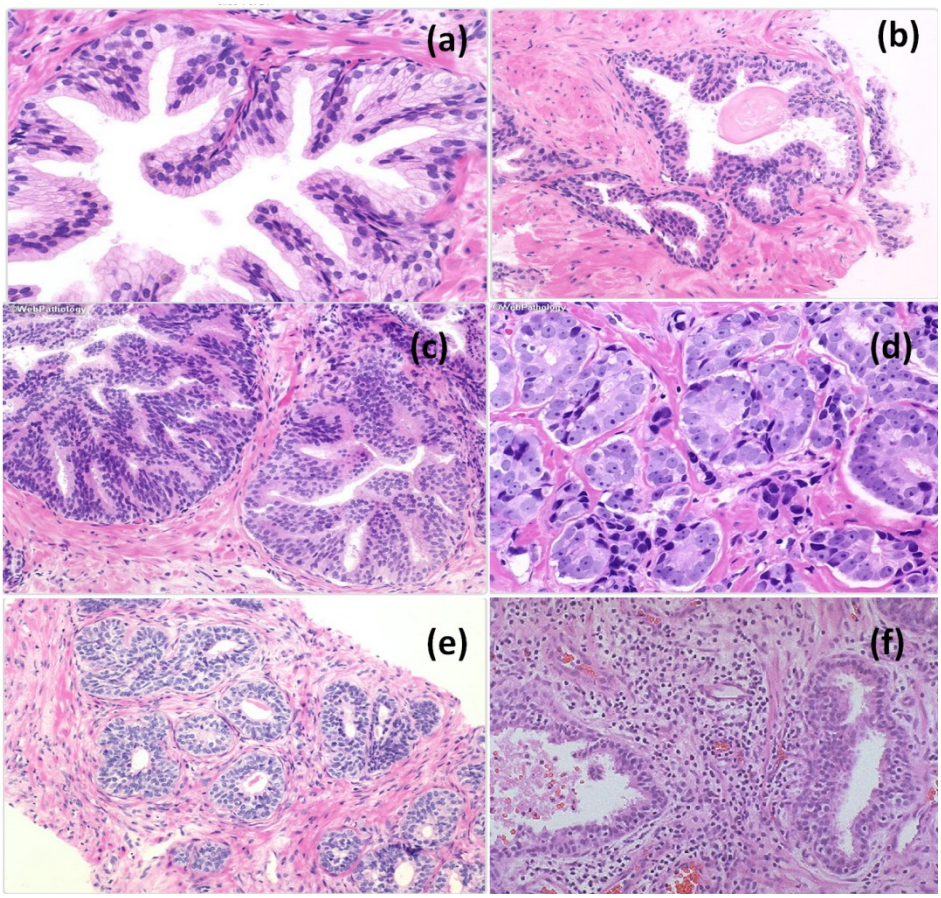

Figure 6-8 Figure showing pathological slides obtained from biopsy samples. (a) Benign prostate glands (b) Benign prostate glands with stroma (c) PIN (d)Adenocarcinoma (e) Benign prostatic hyperplasia (f) Prostattitis

the urethra. Within the prostatic epithelium, there are at least three distinct cell types that can be distinguished by their morphological characteristics, functional significance, and relevance for carcinogenesis [85]. The predominant cell type is the secretory luminal cell, which produces prostatic secretions. The second major epithelial cell type corresponds to the basal cells, which are found between the luminal cells and the underlying basement membrane, and which form a continuous layer in the human prostate, but not in the mouse prostate. Finally, the third prostatic epithelial cell type is

the neuroendocrine cell, a minor population of uncertain embryological origin, which is believed to provide paracrine signals that support the growth of luminal cells. Fibromuscular stroma is situated on the opposite side of the basal cells. Stroma is composed of fibroblasts, smooth muscle cells, and an extracellular matrix rich in collagen fibers that intervenes between the secretory acini. The fibromuscular stroma between the glands accounts for about half of the volume of the prostate.

Scattering changes in PCa tissues majorly comes from four conditions in the prostate. (a) Prostatic intraepithelial neoplasia(PIN) (b)Adenocarcinoma (c) Benign prostatic hyperplasia (d) Prostatitis. From histopathological studies of PCa tissues it is believed that PIN represent the primary precursor of human PCa [86]. A microscopic image of PIN depicts a collection of irregular luminal cells and they are confined to prostate acinus or duct (see Figure 6-8(c)). The architecture of the glands and ducts remains normal. In PCa, the abnormal cells spread beyond the boundaries of the acinus and form clusters without basal cells. Nuclei of PCa cells are enlarged round and have a single prominent nucleolus. In both PIN and PCa (adenocarcinoma) luminial cells will abnormally multiply and leads to increased scattering.

However, from the Figure 6-8(e) and (f) BPH and Prostattitis also has increased number of cells than normal tissues. Benign enlargement of the prostate (BPH) consists of hyperplastic growth of the epithelium and fibromuscular tissue of the transition zone and periurethral area(around urethra where ejaculatory ducts enter prostate) [87,88]. Stromal changes are increased smooth muscle, lymphocytes and ducts (not associated with infectious process of Prostattitis in most cases), reduced elastic tissue. Prostatitis is swelling and inflammation of the prostate gland. In Prostattitis the glands ans stroma are filled with neutrophils explaining the presence of neutrophils on urine microscopic examination. Scattering also changes with BPH and Prostattitis and in principle it is

difficult to separate scattering change is due to cancer, BPH, or Prostattitis. However, in TRUS-NIR scenario the probing depth is approximately two centimeters. BPH occurs in transition zone that is in deeper location for NIR measurements to reach.

Absorption in NIR region is related to chromophore concentrations, such as HbO and Hb. Studies such as indicates that there is immunohistolocal evidence that micro vessel density were associated increased long-term risk for death from PCa. However, the absorption of cancer tissue measured from ex vivo specimens is not expected to be representative because of lack of blood supply and of natural vascular environment.

In addition, the results from this work have been compared with scattering and absorption values from literature (see table 6-2). When comparing our results to previously published data, two important facts must be noted. First, differences such as patient groups (e.g., untreated or recurrent PCa) measurement type (ex-vivo and in-vivo) must be taken into account. The prostate physiology changes drastically upon radiation therapy. Ex-vivo studies measures the prostate after isolation from blood circulation. So the measured absorption coefficient from ex-vivo studies is not reliable as in-vivo studies.

Secondly, CW instrumentation and global minimization techniques are utilized to calculate absorption and scattering. Evolution-strategy (ES) algorithm and genetic algorithms (GAs) borrow from ideas in biological evolution theory to find global minima of objective functions. On the other hand Marcov-chain Monte-carlo methods such as Simulated Annealing algorithm can also be used to separate absorption and scattering from CW data. However, the noise in the measurements has significant impact on the calculated absorption and scattering values.

From the table it is clear that the optical signatures of prostate and PCa are scattered, often measured though an invasive approach. From the table, data from Svensson et al [60] is similar with the current study because the data was recorded

using time domain system. As explained in chapter 2, time domain and frequency domain systems can separate absorption and scattering values. However, absorption values are showing higher differences because of the ex-vivo study.

Table 6-2: Comparison of optical properties of prostate and various wavelengths in literature

Study	Year	wavelength	technology	Measurement type	Cancer type	N	μa	μs'	μeff
Pantelides et al.	1990	633	steady state data	Ex-vivo	normal whole prostates	3	0.7±0.2	8.6±0.5	4.3±0.5
Whitehurst et al.	1994	633	steady state data	In-vivo	untreated BPH and PCa	11			3.6±0.2
Lee et al.	1995	665	steady state data	In-vivo	untreated BPH and PCa	11			3.9±0.5
Lee et al.	1995	630	steady state data	In-vivo	untreated BPH and PCa	11			3.2±0.5
Lee et al.	1999	660	steady state data	In-vivo	untreated PCa	7			3.5±0.7
Svensson et al.	2007	660	time-resolved data	In-vivo	untreated PCa	9	0.5±0.1	8.7±1.9	3.6±0.8
Weersink et al.	2005	762	steady state data	In-vivo	recurrent PCa	22	0.4±0.2	3.4±1.6	2.0±0.6
Zhu et al.	2005	732	steady state data	In-vivo	recurrent PCa	13	0.4±0.2	11.8±8.2	3.3±0.5
Svensson et al.	2007	786	time-resolved data	In-vivo	untreated PCa	9	0.4±0.1	7.1±1.6	2.9±0.7
This study	2014	811	Frequency domain data	Ex vivo	untreated PCa	15		7.73	
Svensson et al.	2007	916	time-resolved data	In-vivo	untreated PCa	9	0.6±0.1	7.7±1.8	3.8±0.8
Essenpreis et al.	1992	1064	Integrating sphere	Ex-vivo	normal whole prostates		1.5±0.2	6.4	

6.6 Conclusion

In this study, we measured the bulk optical properties of benign and PCa tissues from human ex vivo specimens. It is clear that the cancer tissues carry different optical signatures from the benign tissues. It is important to learn that a change in light scattering from benign to cancer tissues is more noticeable or prevailing than that in absorption. This change is attributed to higher cell densities in glandular space and stroma of prostate. Light absorption, on the other hand, remains to be further tested, as a valid optical signature of PCa for DOT, by performing in vivo human prostate measurements. Therefore, light scattering seems to be a robust and promising biomarker for DOT to image if we wish to use DOT for high-grade PCa detection.

Chapter 7

Imaging hemodynamics of prostate cancer during gas stimulus

7.1 Introduction

In previous chapters, TRUS coupled NIR probe has been designed developed and tested using computer simulations and laboratory phantoms. The optical contrast from ex-vivo prostate tissues was also examined in chapter 6. Several previous studies from breast cancer indicated that absorption and light-scattering properties of tumors may be different from those of surrounding tissues, the optical contrast between tumor and surrounding tissue is about 2–3-fold at most in absorption, and much less in light scattering. From chapter 6, tumors has 2.5-4 cm-1 higher scattering than normal tissues. The absorption of cancer tissue measured from ex vivo specimens is not expected to be representative because of lack of blood supply and of natural vascular environment. Low contrast form tumors could be a potential drawback in NIR imaging when used for absolute value reconstructions. An alternative contrast mechanism has to be explored in order to minimize the potential drawbacks of NIR imaging.

Tumor vasculature is known to lack proper vasomotor function because of the deficiency in smooth muscle cells lining the endothelial cells. Thus, tumors are expected to respond differently to changes in the local environment than in normal tissue. The local response of the tumors can be initiated by modulating the tissue oxygenation by changing inhaled gas oxygen percentage. Additionally, the contrast induced by gas modulation may also have the potential to identify tissues that are less susceptible to therapy. Hypoxic cells in vitro and in animal tumors in vivo are documented to be three times more resistant to radiation-induced killing compared with aerobic cell. Therefore, evaluation of tumor oxygenation distributions can be useful indentifying various stages of

tumor growth and efficacy of therapeutic interventions allowing physicians to identify those patients who would benefit from such interventions.

In NIR breast imaging, Carpenter et al. [89] investigated and concluded that gas stimulus consisting of alternating oxygen/carbogen induced the largest and most robust hemodynamic response in healthy breast parenchyma relative to the changes that occurred during the breathing of room air. Gas stimulus caused increases in total hemoglobin and oxygen saturation during the carbogen phase of gas inhalation, and decreases during the oxygen phase. In prostate cancer imaging, validated that hypoxia is related to tumor growth rate and degree of differentiation. During gas intervention Dunning prostate R3327 rat tumor sublines exhibited higher oxygen tension in small tumors than large tumors.

In this chapter, gas modulation was used on the animal models to validate the clip-on probe developed in previous chapters. Additionally, differences between hemodynamics of muscle and prostate were tumors also recorded.

7.2 Experimental Methods

7.2.1 Animal preparation

For validating HCM method, six adult male Copenhagen rats with AT1 prostate rat tumors (on thigh) were utilized. Once the tumor diameter reaches approximately 1 cm, the experiments were planned. The tumor area and the muscle area of the rats are shaved by applying Nair. Next, rats were anesthetized with isoflurane in air through a mask placed over the mouth and nose. A warm water blanket maintained the body temperature of the rats. Two matching phantoms (for both sides) was made by filling plastic bags with intralipid and sealing the bag with vacuum sealer. The plastic bag has a width of ~1cm. Next, the intralipid bag was placed on the tumor of the rat maintain

contact with be thigh of the rat. The designed clip-on probe will be placed on the intralipid bag.

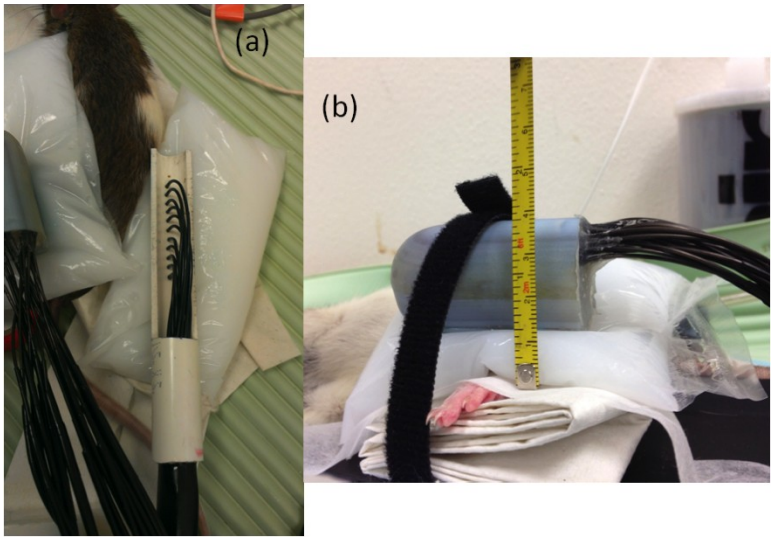

Figure 7-1 (a) Picture showing locations of two probes on rat thighs the two probes have been utilized to record the hemodynamic changes of the tumor and normal muscle. (b) Picture showing the width of the intralipid bag

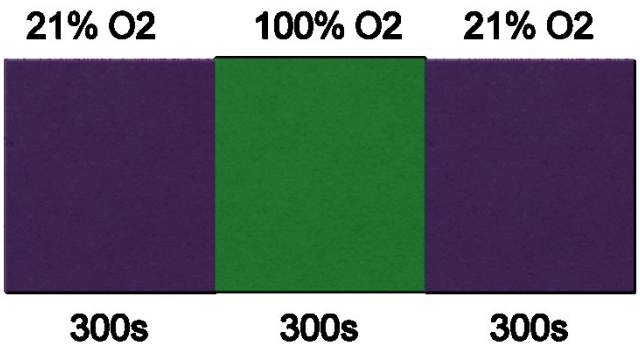

Figure 7-2 Picture showing rats breathing protocol

Specifically, the rat was monitored for 300 seconds (5 mins) while breathing air and the gas was changed into 100% oxygen for another 300 seconds. After 100% oxygen the gas was changed back to air and monitored for 300s. The following protocol was followed for the measurements.

7.2.2 Instrumentation

The laboratory experiment was performed by utilizing a 32-channel, continuous-wave DOT imager [45] (DYNOT, NIRx Medical Technologies). The system delivers and collects two wavelengths of Laser at 760 nm and 830 nm, sequentially from each optical fiber. For the study, 24 bifurcated optodes were utilized and divided into two groups for measuring both cancer and muscle tissues. The first group has 18 optodes (9 sources and 9 detectors) connected to the clip-on rectal probe. The second group is a linear array with six sources and six detectors arranged alternatively separated by a distance of 0.5 cm. The data was selected from the first to fifth nearest S-D pairs and used for image reconstruction.

7.2.3 Image Reconstruction

Optical images are reconstructed every 30 Sec starting from gas challenge. Nineteen images are reconstructed (9 during Oxygen phase and 10 during air phase). The data were calibrated with the first time point in a given stimulus series in order to reduce experimental noise from changes in fiber coupling, fiber attenuation, and other systematic errors. The calibrated data at the nth time point Φ^{n}_{CB} was calculated according to the following equation

$$\Phi^{n}_{CB} = \Phi^{n}_{M} - (\Phi^{1}_{M} - \Phi^{1}_{C}) \qquad 7.1$$

Where Φ^{n}_{M} is the measured data Φ^{1}_{M} and Φ^{1}_{c} are the measured and calculated data for the first frame. This routine is similar to phantom calibration from the previous chapters except that the calibrating phantom data has been replaced by the data from the first frame. Movies were created displaying HbO and Hb dynamics during the gas challenge. Later, 830 nm wavelength data from best three rats is selected to reconstruct images with HCM.

7.3 Results

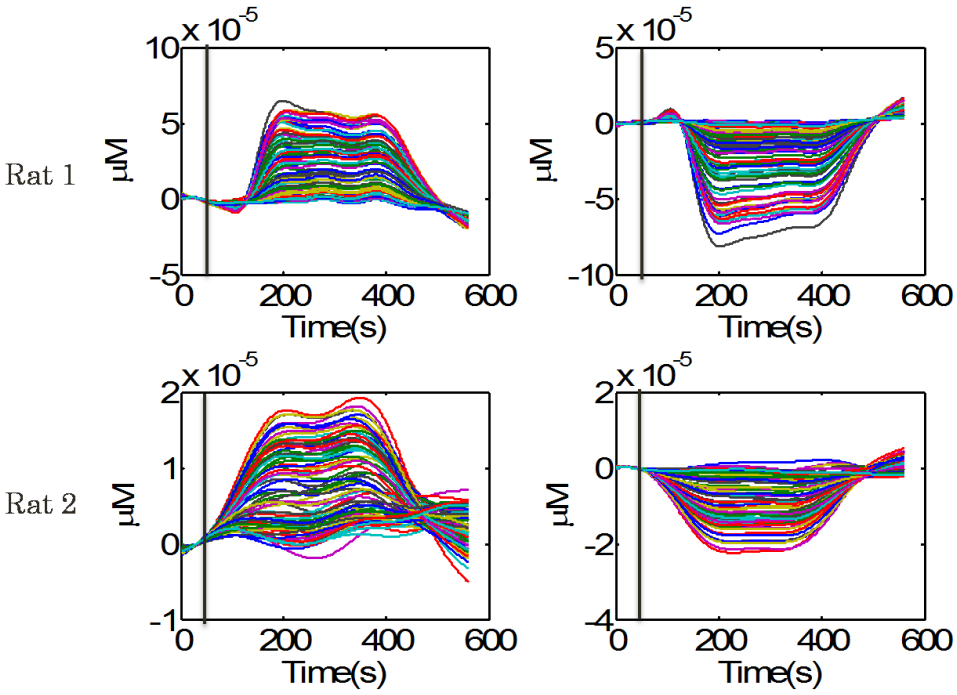

Figure 7-3 Changes in oxy-hemoglobin in cancer and normal tissues during gas challenge. Changes from all channels all rats have been potted

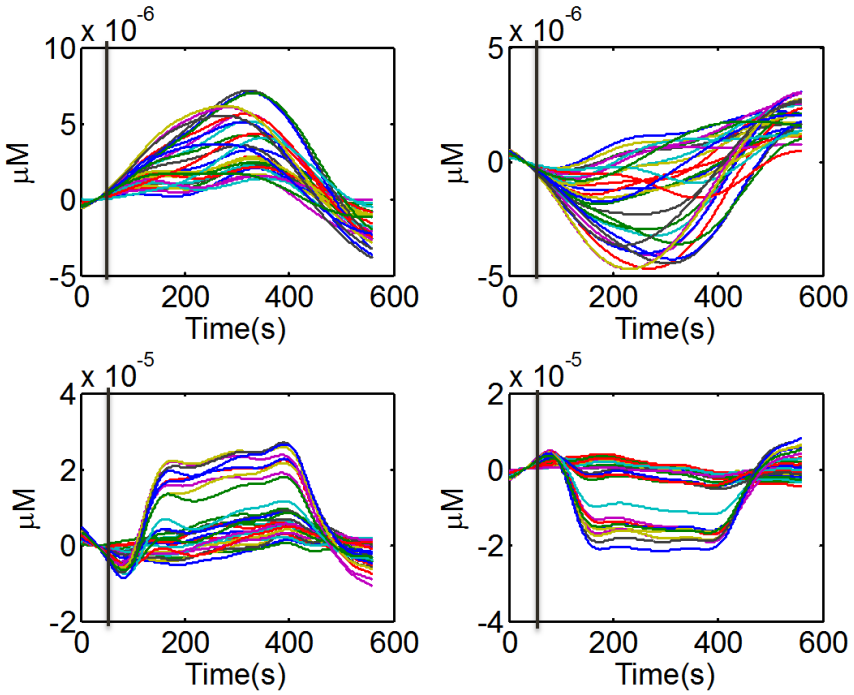

Figure 7-4 Changes in oxy-hemoglobin in cancer and normal tissues during gas challenge

From Figs 7-3 and 7-4 it is clear that Oxy and deoxyhemoglobins are going in opposite directions. Howerver with these plots we are not able to fully distinguish between cancer and normal muscle.

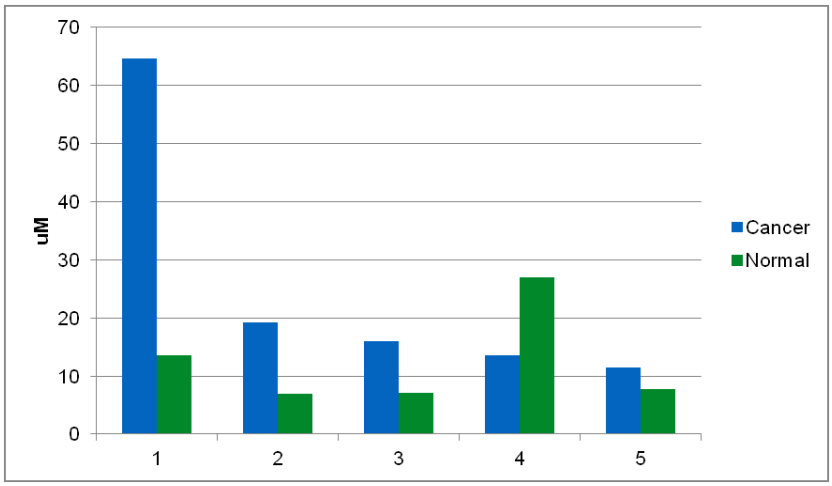

Figure 7-5 Bar plot showing the magnitude of changes in Oxy-hemoglobin during gas challenge between cancer and normal tissues

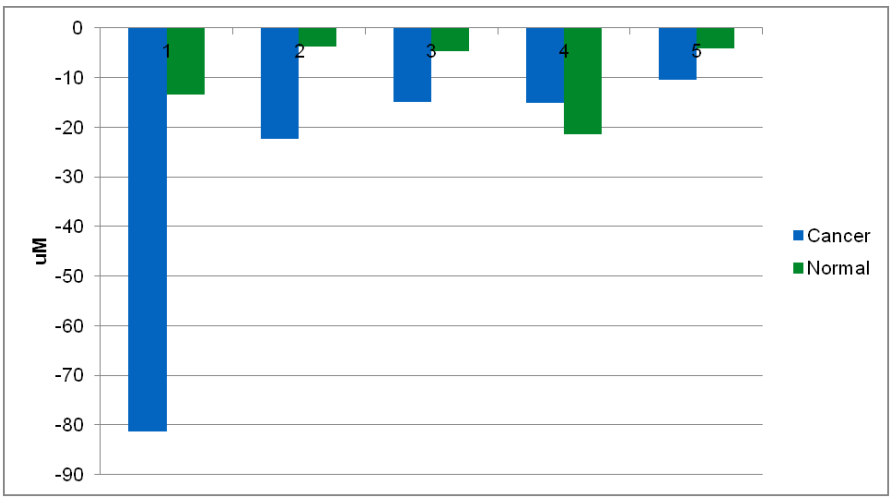

Figure 7-6 Bar plot showing the magnitude of changes in reduced Oxy-hemoglobin during gas challenge between cancer and normal tissues

From Fig. 7-5 and 7-6 it is clear that the cancer has higher changes in both Oxy and deoxy hemoglobin during gas stimulation. However, one rat the changes are in opposite directions. The change across all rats is not uniform.

Image reconstructions:

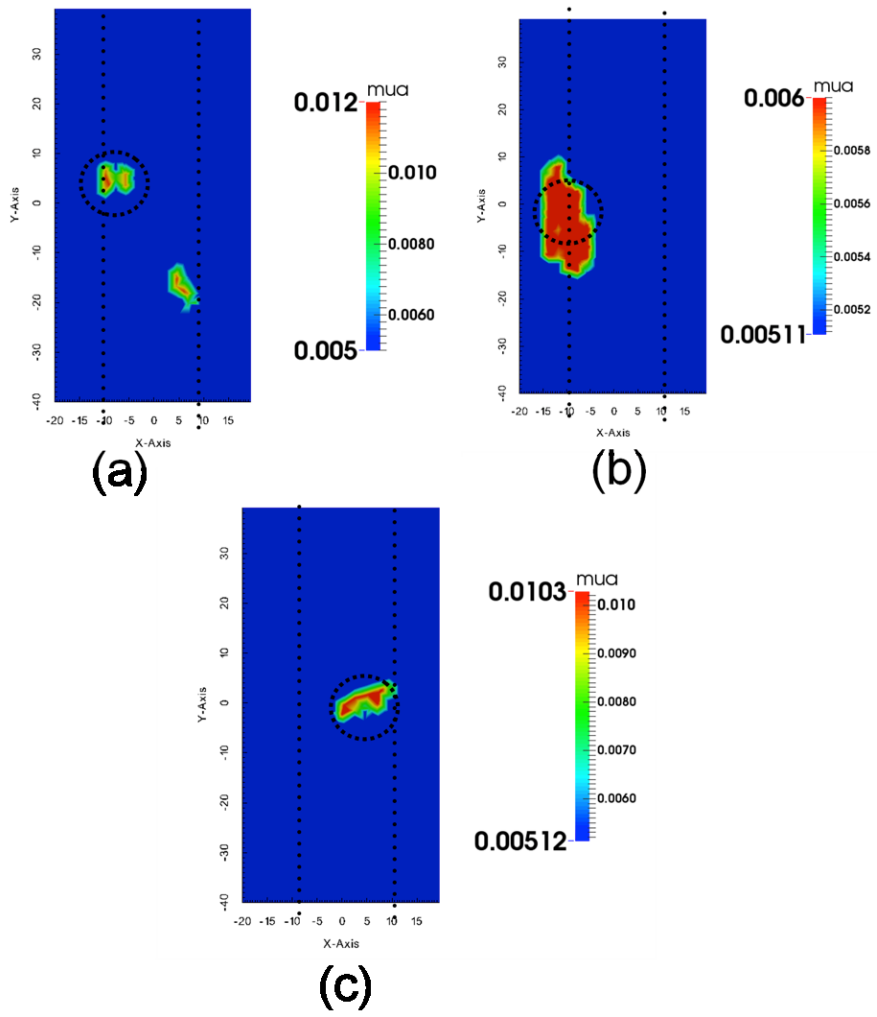

Figure 7-7 (a) (b) and (c) showing the image reconstructions from rats 1,2 and 3 using HCM

Figs 7-7(a),7-7(b) and 7-7(c) shows the image reconstruction using the HCM; The dotted lines depict the approximate location of the probe and the dotted circle indicates the approximate size of the tumor. The tumor locations are not in the center because of the placement of the probe on the phantom bag. Since phantom bag has water and the surface is uneven due to the tumor, the probe usually slips away from the center of the tumor.

7.4 Discussion and Conclusion

This study demonstrated that a gas stimulus consisting of alternating air/oxygen induced the robust hemodynamic response prostate cancer tissue (AT1 tumor) relative to the changes that occurred in muscle tissue. This stimulus caused increases in Oxy-hemoglobin during the oxygen phase of gas inhalation, and decreases during the air phase. For de-Oxy hemoglobin the changes are opposite with respective to Oxy hemoglobin. On the other hand, Clip-on optical probe has been validated using animal models. The clip on probe is able to reconstruct tumors approximately 1cm deep from the surface.

Chapter 8 Concluding Remarks

8.1 Conclusion

In summary, the TRUS coupled trans-rectal NIR imaging probe was designed and fabricated. Specifically, two types of TRUS coupled optical probe designs were explored. In design 1, photodiodes were placed directly on the side of the TRUS probe. In design 2, 3d printing technology has been utilized to create a clip-on optical probe compatible with existing clinical TRUS facility.

For image reconstruction HCM method has been proposed, which improves the image reconstruction in the absence of prior information on cancer location in prostate cancer imaging with diffuse optical tomography. HCM works by (1) Utilizing the available prior information on the locations of prostate, peri-prostate tissue and rectum wall and then (2) dividing the probable location of a prostate tumor or tumors into several clusters. This latter step made the prostate partially heterogeneous. The dimensions of the clusters were iteratively changed to limit the mixing of normal tissue with cancerous tissue and vice versa. Combination of DCA with L1-regularization (DCA-L1) has also been proposed for perturbation based (dynamic) DOT, which can offer significant improvement in depth localization and spatial resolution for DOT images. In DCA-L1, the reconstructed images are obtained by using L1 regularization technique after modifying the Jacobian or sensitivity matrix by DCA.

Bulk optical properties of benign and prostate cancer tissues from human ex vivo specimens. Based on Fig. 3 and further statistical analyses, it is clear that the cancer tissues carry different optical signatures from the benign tissues. It is important to learn that a change in light scattering from benign to cancer tissues is more noticeable or prevailing than that in absorption.

8.2 Contributions of This Work

The most important contribution of this work is to design, develop and test TRUS coupled optical probe. Optical imaging probe works as complimentary technology for existing NIR probe. Utilizing 3d printing technology in optical probe design is an important direction towards future in-vivo clinical studies. Measurement of bulk optical properties of ex-vivo benign and prostate cancer tissues demonstrated that the cancer tissues carry different optical signatures from the benign tissues.

The work in this thesis was focused on both instrumentation and experimental demonstration. The contribution of this work involved multiple areas such as hardware development, system integration, imaging reconstruction and data calibration. The instrumentation part includes the optics related tools designing and assembling, source coupling setup, programming of the system control by Labview and developing the codes for data calibration and imaging reconstruction. The experimental demonstration covers all the tests designed to quantify the system performance and validate the potential on the clinical application.

8.3 Limitations and Future Scope

In DCA-L1 method, the optimized empirical parameters (i.e., NIPCaG and NSNewton) were derived from phantom experiments. For quantitative or rigorous validation of DCA-L1, in future a joint fMRI-DOT study in order to make volumetric DOT possible for human brain imaging. DCA+L1+L2 can also be used to compensate over shrinkage of image by L1 method.

HCM method assumed that variation in light scattering across the prostate and its surrounding tissues is minimal. This assumption was made because CW-based DOT measurements cannot provide enough independent data quantities to uniquely solve both

light scattering and absorption coefficients of the imaged objects. With this assumption, it is possible to focus on DOT reconstruction of absorption coefficients of simulated prostate cancer, using both simulation and experimental data, to implement and validate HCM. I acknowledge that the assumption of constant light scattering across the human prostate tissues may not be accurate, resulting in two negative impacts the conclusion of HCM. One alternative is to take advantage of Simulated annealing (SA) method and reconstruct scattering and absorption before step 1. I recommend using frequency domain system, which can separate both absorption and scattering in future.

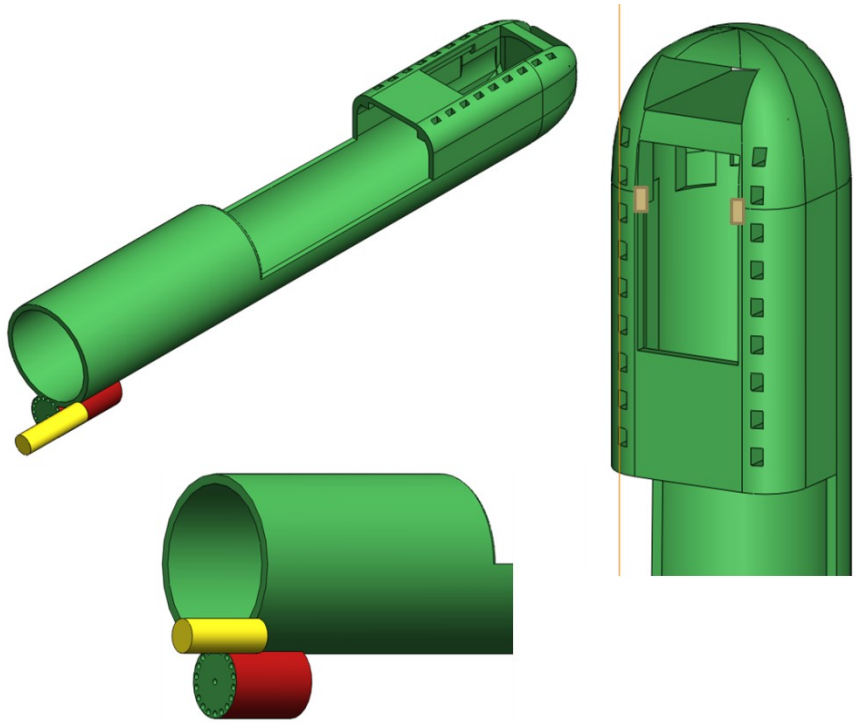

Figure 8-1: Simulated future probe design showing space for rectangular fibers, self calibrating phantom attached to the probe (red) and 3axis gyroscope(yellow)

Although I successfully designed and tested TRUS coupled optical probe real time (clinical imaging) issues were not considered in the design. They are (1) Probe contact: Measurements in DOT are very sensitive to optical contact between the optodes and tissues. It is very critical to ensure sufficient contact or good optical coupling. However, in transrectal measurements, it is impossible to learn such information because of anatomical location. (2) Calibration: Calibration in DOT is also very sensitive to bend losses in the optical fiber. Current challenge is to limit the diameter of the fiber and obtain good SNR. Optical probe needs to be calibrated before each use. During the measurement the probe will be rotated in the rectum so the bending of the optical fibers will change which leads to light loss. (3) Co registration with ultrasound images: 3d anatomical information of prostate will be obtained by stitching 2d ultrasound images taken at different angles. However, alignment of the 2d slices is the key issue to form 3d image from 2d slices. (4) SNR: Achieving good SNR with least possible probe diameter.

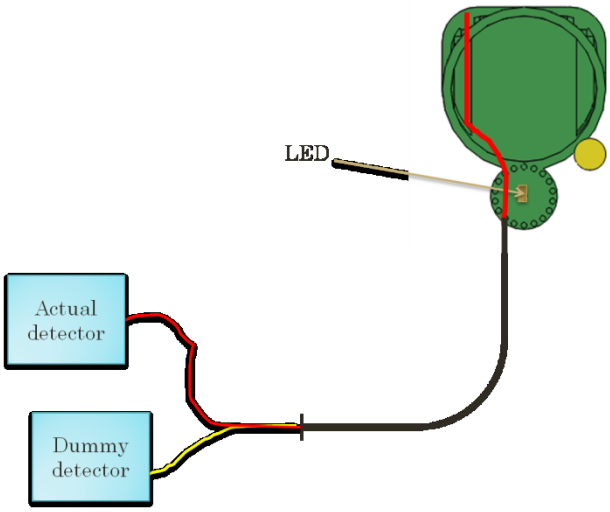

Figure 8-2 Simulated probe design showing the arrangement of dummy detector for self calibrating probe

Touch sensing optode can be used to solve probe contact issue. Capacitive touch sensor should be incorporated into the probe. Gyroscopic sensor will be attached to the probe so that picth, yaw and roll information of each slice will be recorded. Using the information(pitch, yaw and roll) from gyroscopic sensor slices will be realigned.

References

1. R. Siegel, J. Ma, Z. Zou and A. Jemal, "Cancer statistics, 2014," : a cancer journal for clinicians (2014).
2. R. J. Cohen, B. A. Shannon, M. Phillips and R. E. Moorin, "Central zone carcinoma of the prostate gland: a distinct tumor type with poor prognostic features," The Journal of (2008).
3. A. Erbersdobler, H. Augustin, T. Schlomm and R. P. Henke, "Prostate cancers in the transition zone: Part 1; pathological aspects," BJU Int **94**, 1221-5 (2004).
4. H. Augustin, A. Erbersdobler, P. G. Hammerer, M. Graefen and H. Huland, "Prostate cancers in the transition zone: Part 2; clinical aspects," BJU Int **94**, 1226-9 (2004).
5. A. M. De Marzo, E. A. Platz, S. Sutcliffe and J. Xu, "Inflammation in prostate carcinogenesis," Nature Reviews (2007).
6. W. J. Catalona, D. S. Smith and T. L. Ratliff, "Measurement of prostate-specific antigen in serum as a screening test for prostate cancer," England Journal of (1991).
7. H. B. Carter, J. D. Pearson, E. J. Metter, L. J. Brant, D. W. Chan, R. Andres, J. L. Fozard and P. C. Walsh, "Longitudinal evaluation of prostate-specific antigen levels in men with and without prostate disease," JAMA **267**, 2215-20 (1992).
8. F. H. Schröder, A. B. Kruger and J. Rietbergen, "Evaluation of the digital rectal examination as a screening test for prostate cancer," Journal of the (1998).
9. M. K. Brawer, M. P. Chetner and J. Beatie, "Screening for prostatic carcinoma with prostate specific antigen," The Journal of (1992).

10. W. J. Catalona, D. S. Smith, T. L. Ratliff and J. W. Basler, "Detection of organ-confined prostate cancer is increased through prostate-specific antigen-based screening," JAMA 2**70,** 948-54 (1993).

11. E. D. Crawford, E. P. DeAntoni, R. Etzioni, V. C. Schaefer, R. M. Olson and C. A. Ross, "Serum prostate-specific antigen and digital rectal examination for early detection of prostate cancer in a national community-based program. The Prostate Cancer Education Council," Urology 4**7,** 863-9 (1996).

12. A. Wolf, R. C. Wender and R. B. Etzioni, "American Cancer Society guideline for the early detection of prostate cancer: update 2010," CA: a cancer journal (2010).

13. J. B. Meigs, M. J. Barry, J. E. Oesterling and S. J. Jacobsen, "Interpreting results of prostate-specific antigen testing for early detection of prostate cancer," J Gen Intern Med 1**1,** 505-12 (1996).

14. A. Hoogendam, F. Buntinx and H. C. de Vet, "The diagnostic value of digital rectal examination in primary care screening for prostate cancer: a meta-analysis," Fam Pract 1**6,** 621-6 (1999).

15. W. J. Catalona, J. P. Richie, F. R. Ahmann, M. A. Hudson, P. T. Scardino, R. C. Flanigan, J. B. deKernion, T. L. Ratliff, L. R. Kavoussi and B. L. Dalkin, "Comparison of digital rectal examination and serum prostate specific antigen in the early detection of prostate cancer: results of a multicenter clinical trial of 6,630 men," J. Urol 1**51,** 1283-90 (1994).

16. B. Turkbey, P. A. Pinto and P. L. Choyke, "Imaging techniques for prostate cancer: implications for focal therapy," Nature Reviews Urology (2009).

17. M. A. Haider, T. H. van der Kwast, J. Tanguay, A. J. Evans, A. T. Hashmi, G. Lockwood and J. Trachtenberg, "Combined T2-weighted and diffusion-weighted

MRI for localization of prostate cancer," AJR Am J Roentgenol 1**89,** 323-8 (2007).

18. M. Perrotti, R. P. Kaufman, T. A. Jennings, H. T. Thaler, S. M. Soloway, M. D. Rifkin and H. A. Fisher, "Endo-rectal coil magnetic resonance imaging in clinically localized prostate cancer: is it accurate?," J. Urol 1**56,** 106-9 (1996).
19. T. Hara, N. Kosaka, H. Kishi - Journal of nuclear medicine: official and 1998, "PET imaging of prostate cancer using carbon-11-choline," europepmc.org Prostate cancer is difficult to visualize using current techniques. Recently (31).
20. N. Oyama, H. Akino, H. Kanamaru and Y. Suzuki, "11C-acetate PET imaging of prostate cancer," Journal of Nuclear (2002).
21. W. J. Ellis and M. K. Brawer, "The significance of isoechoic prostatic carcinoma," J. Urol 1**52,** 2304-7 (1994).
22. H. Dehghani, M. E. Eames, P. K. Yalavarthy, S. C. Davis, S. Srinivasan, C. M. Carpenter, B. W. Pogue and K. D. Paulsen, "Near infrared optical tomography using NIRFAST: Algorithm for numerical model and image reconstruction," Commun Numer Methods Eng 2**5,** 711-732 (2008).
23. M. Schweiger, A. Gibson and S. R. Arridge, "Computational aspects of diffuse optical tomography," Computing in Science & (2003).
24. Q. Zhang, T. J. Brukilacchio, A. Li, J. J. Stott, T. Chaves, E. Hillman, T. Wu, M. Chorlton, E. Rafferty, R. H. Moore, D. B. Kopans and D. A. Boas, "Coregistered tomographic x-ray and optical breast imaging: initial results," J Biomed Opt 1**0,** 024033 (2005).

25. T. O. McBride, B. W. Pogue, S. Jiang, U. L. Osterberg, K. D. Paulsen and S. P. Poplack, "Initial studies of in vivo absorbing and scattering heterogeneity in near-infrared tomographic breast imaging," Opt Lett 2**6,** 822-4 (2001).

26. B. r. i. a. n. . W. .. . P. o. g. u. e. Ben A. Brooksby, "Near-Infrared (NIR) Tomography Breast Image Reconstruction With A Priori Structural Information From MRI: Algorithm Development for Reconstructing Heterogeneities," IEEE J SEL TOP QUANT V**OL. 9,,** (2003).

27. P. K. Yalavarthy, B. W. Pogue, H. Dehghani, C. M. Carpenter, S. Jiang and K. D. Paulsen, "Structural information within regularization matrices improves near infrared diffuse optical tomography," Opt Express 1**5,** 8043-58 (2007).

28. G. Xu, D. Piao, C. H. Musgrove, C. F. Bunting and H. Dehghani, "Trans-rectal ultrasound-coupled near-infrared optical tomography of the prostate, part I: simulation," Opt Express 1**6,** 17484-504 (2008).

29. P. K. Yalavarthy, B. W. Pogue, H. Dehghani, C. M. Carpenter, S. Jiang and K. D. Paulsen, "Structural information within regularization matrices improves near infrared diffuse optical tomography," Opt Express 1**5,** 8043-58 (2007).

30. H. Dehghani, B. W. Pogue, J. Shudong, B. Brooksby and K. D. Paulsen, "Three-dimensional optical tomography: resolution in small-object imaging," Appl Opt 4**2,** 3117-28 (2003).

31. H. Niu, Z. J. Lin, F. Tian, S. Dhamne and H. Liu, "Comprehensive investigation of three-dimensional diffuse optical tomography with depth compensation algorithm," J Biomed Opt 1**5,** 046005 (2010).

32. F. Tian, H. Niu, S. Khadka, Z. J. Lin and H. Liu, "Algorithmic depth compensation improves quantification and noise suppression in functional diffuse optical tomography," Biomed Opt Express 1**,** 441-452 (2010).

33. S. R. Arridge and W. R. Lionheart, "Nonuniqueness in diffusion-based optical tomography," Opt Lett 2**3,** 882-4 (1998).

34. T. Durduran, R. Choe, W. B. Baker and A. G. Yodh, "Diffuse optics for tissue monitoring and tomography," Reports on Progress in Physics 7**3,** 076701 (2010).

35. M. SÃŒzen, A. Giannoula and T. Durduran, "Compressed sensing in diffuse optical tomography," Optics Express 18, **2**3676-23690 (2010).

36. N. Cao, A. Nehorai and M. Jacobs, "Image reconstruction for diffuse optical tomography using sparsity regularization and expectation-maximization algorithm," Opt Express 15, **1**3695-708 (2007).

37. C. R. Vogel, Com*putational methods for inverse problems (S*ociety for Industrial Mathematics, 2002), Vol. 23.

38. H. W. Engl, M. Hanke and A. Neubauer, Reg*ularization of inverse problems (S*pringer Netherlands, 1996), Vol. 375.

39. S. J. Kim, K. Koh, M. Lustig, S. Boyd and D. Gorinevsky, "An interior-point method for large-scale l1-regularized least squares," Selected Topics in Signal Processing, IEEE Journal of 1, **6**06-617 (2007).

40. http://www.nmr.mgh.harvard.edu/PMI/toolbox/, "PMI toolbox," (2014).

41. http://www.stanford.edu/~boyd/l1_ls/, "L1-LS Toolbox," (2014).

42. F. Tian, G. Alexandrakis and H. Liu, "Optimization of probe geometry for diffuse optical brain imaging based on measurement density and distribution," Appl Opt 48, **2**496-504 (2009).

43. L. Lin, N. Haijing and L. Hanli, ""Volumetric diffuse optical tomography for small animals using a CCD-camera-based imaging system"," (2012).

44. Q. Zhao, L. Ji and T. Jiang, "Improving performance of reflectance diffuse optical imaging using a multicentered mode," J Biomed Opt 11, **0**64019 (2006).

45. "http://www.nirx.net," (0).

46. D. R. Leff, F. Orihuela-Espina, C. E. Elwell, T. Athanasiou, D. T. Delpy, A. W. Darzi and G. Z. Yang, "Assessment of the cerebral cortex during motor task behaviours in adults: a systematic review of functional near infrared spectroscopy (fNIRS) studies," Neuroimage 54, **2**922-36 (2011).

47. F. Tian, M. R. Delgado, S. C. Dhamne, B. Khan, G. Alexandrakis, M. I. Romero, L. Smith, D. Reid, N. J. Clegg and H. Liu, "Quantification of functional near infrared spectroscopy to assess cortical reorganization in children with cerebral palsy," Opt Express 18, **2**5973-86 (2010).

48. M. A. Franceschini, D. K. Joseph, T. J. Huppert, S. G. Diamond and D. A. Boas, "Diffuse optical imaging of the whole head," J Biomed Opt 11, **0**54007 (2006).

49. S. R. Arridge, "Optical tomography in medical imaging," Inverse problems 15, **4**1 (1999).

50. A. Corlu, T. Durduran, R. Choe, M. Schweiger, E. M. Hillman, S. R. Arridge and A. G. Yodh, "Uniqueness and wavelength optimization in continuous-wave multispectral diffuse optical tomography," Opt Lett 28, **2**339-41 (2003).

51. B. W. Zeff, B. R. White, H. Dehghani, B. L. Schlaggar and J. P. Culver, "Retinotopic mapping of adult human visual cortex with high-density diffuse optical tomography," Proc. Natl. Acad. Sci. U.S.A 104**, 1**2169-74 (2007).

52. R. Parlapalli and V. Sharma, "Comparison of hemodynamic response non-linearity using simultaneous near infrared spectroscopy and magnetic resonance imaging modalities," SPIE BiOS: (2009).

53. B. Khan, P. Chand and G. Alexandrakis, "Spatiotemporal relations of primary sensorimotor and secondary motor activation patterns mapped by NIR imaging," Biomed Opt Express 2, **3**367-86 (2011).

54. S. Srinivasan, B. W. Pogue, H. Dehghani, S. Jiang, X. Song and K. D. Paulsen, "Improved quantification of small objects in near-infrared diffuse optical tomography," J Biomed Opt 9, **1**161-71 (2004).

55. Z. Jiang, D. Piao, G. Xu, J. W. Ritchey, G. R. Holyoak, K. E. Bartels, C. F. Bunting, G. Slobodov and J. S. Krasinski, "Trans-rectal ultrasound-coupled near-infrared optical tomography of the prostate, part II: experimental demonstration," Opt Express 16, **1**7505-20 (2008).

56. V. Kolehmainen, S. R. Arridge, M. Vauhkonen and J. P. Kaipio, "Simultaneous reconstruction of internal tissue region boundaries and coefficients in optical diffusion tomography," Phys Med Biol 45, **3**267-83 (2000).

57. A. D. Zacharopoulos, M. Schweiger, V. Kolehmainen and S. Arridge, "3D shape based reconstruction of experimental data in Diffuse Optical Tomography," Opt Express 17, **1**8940-56 (2009).

58. B. J. Tromberg, B. W. Pogue, K. D. Paulsen, A. G. Yodh, D. A. Boas and A. E. Cerussi, "Assessing the future of diffuse optical imaging technologies for breast cancer management," Med Phys 35, **2**443-51 (2008).

59. J. H. Ali, W. B. Wang, M. Zevallos and R. R. Alfano, "Near infrared spectroscopy and imaging to probe differences in water content in normal and cancer human prostate tissues," Technol. Cancer Res. Treat 3, **4**91-7 (2004).

60. T. Svensson, S. Andersson-Engels, M. Einarsdóttír and K. Svanberg, "In vivo optical characterization of human prostate tissue using near-infrared time-resolved spectroscopy," J Biomed Opt 12, 0**14**022 (2007).

61. R. A. Weersink, A. Bogaards, M. Gertner, S. R. Davidson, K. Zhang, G. Netchev, J. Trachtenberg and B. C. Wilson, "Techniques for delivery and monitoring of TOOKAD (WST09)-mediated photodynamic therapy of the prostate: clinical

experience and practicalities," J. Photochem. Photobiol. B, Biol 79, 2**11**-22 (2005).

62. T. C. Zhu, J. C. Finlay and S. M. Hahn, "Determination of the distribution of light, optical properties, drug concentration, and tissue oxygenation in-vivo in human prostate during motexafin lutetium-mediated photodynamic therapy," J. Photochem. Photobiol. B, Biol 79, 2**31**-41 (2005).

63. K. Valluru, B. Chinni, S. Bhatt and V. Dogra, "Probe design for Photoacoustic imaging of prostate," Imaging Systems (2010).

64. R. A. Huch Böni, J. A. Boner, U. M. Lütolf, F. Trinkler, D. M. Pestalozzi and G. P. Krestin, "Contrast-enhanced endorectal coil MRI in local staging of prostate carcinoma," J Comput Assist Tomogr 19, 232**-7** (1995).

65. L. A. G. Ries, D. Melbert and M. Krapcho, "SEER cancer statistics review, 1975-2005," , MD: National Cancer (2008).

66. W. A. Sakr, D. J. Grignon and J. D. Crissman, "High grade prostatic intraepithelial neoplasia (HGPIN) and prostatic adenocarcinoma between the ages of 20-69: an autopsy study of 249 cases," In vivo (Athens, (1993).

67. A. L. Potosky, W. W. Davis, R. M. Hoffman, J. L. Stanford, R. A. Stephenson, D. F. Penson and L. C. Harlan, "Five-year outcomes after prostatectomy or radiotherapy for prostate cancer: the prostate cancer outcomes study," J. Natl. Cancer Inst 96, 135**8-**67 (2004).

68. D. V. Makarov, B. J. Trock, E. B. Humphreys and L. A. Mangold, "Updated nomogram to predict pathologic stage of prostate cancer given prostate-specific antigen level, clinical stage, and biopsy Gleason score (Partin tables) based," Urology (2007).

69. A. W. Partin, L. A. Mangold, D. M. Lamm, P. C. Walsh, J. I. Epstein and J. D. Pearson, "Contemporary update of prostate cancer staging nomograms (Partin Tables) for the new millennium," Urology 58, 843-**8** (2001).

70. Y. Huang, S. Isharwal, A. Haese, F. K. Chun, D. V. Makarov, Z. Feng, M. Han, E. Humphreys, J. I. Epstein, A. W. Partin and R. W. Veltri, "Prediction of patient-specific risk and percentile cohort risk of pathological stage outcome using continuous prostate-specific antigen measurement, clinical stage and biopsy Gleason score," BJU Int 107, 15**62-**9 (2011).

71. O. Smaletz, H. I. Scher, E. J. Small, D. A. Verbel, A. McMillan, K. Regan, W. K. Kelly and M. W. Kattan, "Nomogram for overall survival of patients with progressive metastatic prostate cancer after castration," J. Clin. Oncol 20, 397**2-**82 (2002).

72. M. R. Cooperberg, D. J. Pasta, E. P. Elkin, M. S. Litwin, D. M. Latini, J. Du Chane and P. R. Carroll, "The University of California, San Francisco Cancer of the Prostate Risk Assessment score: a straightforward and reliable preoperative predictor of disease recurrence after radical prostatectomy," J. Urol 173, 19**38-**42 (2005).

73. M. L. Blute, E. J. Bergstralh, A. W. Partin, P. C. Walsh, M. W. Kattan, P. T. Scardino, J. E. Montie, J. D. Pearson, J. M. Slezak and H. Zincke, "Validation of Partin tables for predicting pathological stage of clinically localized prostate cancer," J. Urol 164, 15**91-**5 (2000).

74. J. B. Eifler, Z. Feng, B. M. Lin, M. T. Partin - BJU and 2013, "An updated prostate cancer staging nomogram (Partin tables) based on cases from 2006 to 2011," Wiley Online Library Patients and Methods The study population consisted of 5,629 consecutive men who underwent RP and staging

lymphadenectomy at the Johns Hopkins Hospital between January 1, 2006 and July 30 (2011).

75. F. H. Schröder, J. Hugosson and M. J. Roobol, "Screening and prostate-cancer mortality in a randomized European study," England Journal of (2009).

76. F. H. Schröder, J. Hugosson and M. J. Roobol, "Prostate-cancer mortality at 11 years of follow-up," England Journal of (2012).

77. G. Draisma, R. Etzioni, A. Tsodikov, A. Mariotto, E. Wever, R. Gulati, E. Feuer and H. de Koning, "Lead time and overdiagnosis in prostate-specific antigen screening: importance of methods and context," J. Natl. Cancer Inst 101, 374-**83** (2009).

78. J. Li and T. C. Zhu, "Determination of in vivo light fluence distribution in a heterogeneous prostate during photodynamic therapy," Phys Med Biol 53, 2103-**14** (2008).

79. K. K. Wang and T. C. Zhu, "Reconstruction of in-vivo optical properties for human prostate using interstitial diffuse optical tomography," Opt Express 17, 11665-**7**2 (2009).

80. L. K. Lee, C. Whitehurst, M. L. Pantelides and J. V. Moore, "An interstitial light assembly for photodynamic therapy in prostatic carcinoma," BJU Int 84, 821-6 **(**1999).

81. M. L. Pantelides, C. Whitehurst, J. V. Moore, T. A. King and N. J. Blacklock, "Photodynamic therapy for localised prostatic cancer: light penetration in the human prostate gland," J. Urol 143, 398-**401** (1990).

82. A. Roggan, K. Dörschel, O. Minet and D. Wolff, "The optical properties of biological tissue in the near infrared wavelength range: review and measurements," LITT: laser-induced (1995).

83. V. Sharma, E. O. Olweny, P. Kapur, J. A. Cadeddu, C. G. Roehrborn and H. Liu, "Prostate cancer detection using combined auto-fluorescence and light reflectance spectroscopy: ex vivo study of human prostates," Biomed Opt Express 5, 1512-29 (2014).

84. R. Storn and K. Price, "Differential evolution–a simple and efficient heuristic for global optimization over continuous spaces," Journal of global optimization (1997).

85. M. M. Shen and C. Abate-Shen, "Molecular genetics of prostate cancer: new prospects for old challenges," Genes Dev 24, 1967-200**0** (2010).

86. D. G. Bostwick and L. Cheng, "Precursors of prostate cancer," Histopathology (2012).

87. A. Ziada, M. Rosenblum and E. D. Crawford, "Benign prostatic hyperplasia: an overview," Urology (1999).

88. C. G. Roehrborn, "Benign prostatic hyperplasia: an overview," Reviews in urology (2005).

89. C. M. Carpenter, R. Rakow-Penner, S. Jiang, B. W. Pogue, G. H. Glover and K. D. Paulsen, "Monitoring of hemodynamic changes induced in the healthy breast through inspired gas stimuli with MR-guided diffuse optical imaging," Med Phys 37, 1638-46 **(2**010).

Biographical Information

Venkaiah Chowdary Kavuri (Venki) was born and brought up in Macherla, Andhra Pradesh, India. He earned his undergraduate degree in biomedical engineering from Jawaharlal Nehru Technological University, India in the year 2007. He joined Department of bioengineering University of Texas Arlington in 2008. He was engaged in prostate cancer research project in 2009. His research work has resulted in 2 peer-reviewed 1st-authored journal papers and a couple of manuscripts either under review or to be submitted very soon, as well as leading to a patent application. He has presented and/or published more than six conference proceeding papers at either SPIE conferences or OSA Biomedical Optics topical meetings. His areas of interests include computational modeling and Optical instrumentation.